Neutron-Scattering Studies on Chiral Multiferroics

Inaugural-Dissertation

zur

Erlangung des Doktorgrades

der Mathematisch-Naturwissenschaftlichen Fakultät

der Universität zu Köln

vorgelegt von

Max Michael Baum

aus Köln

Köln, 2013

Abstract

Magnetoelectric multiferroics exhibit a strong correlation of magnetism and ferro-electricity. Among the multiferroics with a strong magnetoelectric effect many have a chiral antiferromagnetic structure. In these materials it is possible to control the electric polarisation by an applied magnetic field and, inversely, to manipulate the antiferromagnetic domains by an applied electric field. The observation of antiferromagnetic domains requires a microscopic method, which neutron scattering with polarised neutrons is particularly suitable for. This thesis reports on neutron and X-ray measurements on several (chiral) antiferromagnetic multiferroics. Special attention is devoted to the switching of (chiral) antiferromagnetic domains.

Neutron-diffraction data on the magnetic structures of the pyroxenes $NaFeSi_2O_6$ and $LiFeSi_2O_6$ are presented. $LiFeSi_2O_6$ undergoes a single magnetic phase transition below $18\,K$ into a canted antiferromagnetic structure with the magnetic space group $P2_1/c'$. $NaFeSi_2O_6$ undergoes two magnetic phase transitions. Both phases are incommensurate with propagation vector $\boldsymbol{k} = (0, 0.77, 0)$. Below $8\,K$ a transverse spin-density wave with moments in the ac plane sets in and below $6\,K$ a helix with moments remaining in the ac plane evolves. By the use of spherical neutron polarisation analysis it is demonstrated that antiferromagnetic domains in $LiFeSi_2O_6$ can be reversed by a combination of electric and magnetic fields. The magnetic structure of $LiFeSi_2O_6$ gives rise to a toroidal moment. Therefore, the results are discussed in the context of manipulating toroidal domains. Furthermore, the magnon dispersion and the spin density of $LiFeSi_2O_6$ are presented.

In many chiral multiferroics it is possible to reverse the chirality of the magnetic structure by an applied electric field providing the opportunity of driving hysteresis loops (chiral ratio vs. electric field). Results of the time dependence of this switching process in $MnWO_4$ studied by stroboscopic techniques for polarised neutron scattering reveal a surprisingly slow relaxation process in the time scale of $2\,ms$ to $30\,ms$ and a strong temperature dependence.

Furthermore, static hysteresis loops recorded on $TbMnO_3$ and $DyMnO_3$ are reported. In $TbMnO_3$, the coercive field increases linearly with decreasing temperature. In $DyMnO_3$, driving of hysteresis loops is possible only close to the ferroelectric phase transition. Further investigations on $TbMnO_3$ show that the quasi-lock-in of the magnetic propagation vector takes place at temperatures slightly above the development of the chiral magnetic structure. In addition, the propagation vector increases linearly with isotropic pressure. X-ray diffraction on single crystals of $TbMnO_3$ and YMn_2O_5 reveals that the deviation of the ions from their centrosymmetric positions in the ferroelectric phase is beyond the resolution limit of the performed diffraction experiments.

Kurzzusammenfassung

Magnetoelektrische Multiferroika sind gekennzeichnet durch eine starke Wechselwirkung magnetischer und ferroelektrischer Ordnung. Viele dieser Multiferroika mit starkem magnetoelektrischem Effekt bilden eine chirale, antiferromagnetische Magnetstruktur. In diesen Materialien ist es möglich, die elektrische Polarisation mit einem äußeren Magnetfeld, und umgekehrt, die antiferromagnetischen Domänen mit einem äußeren elektrischen Feld zu schalten. Die Beobachtung antiferromagnetischer Domänen ist nur mit einer mikroskopischen Methode zugänglich, wofür sich Neutronenstreuung mit polarisierten Neutronen als hervorragend geeignet erweist. Diese Arbeit handelt von Neutronen- und Röngenmessungen an verschiedenen (chiralen) antiferromagnetischen Multiferroika. Das Schalten von (chiralen) antiferromagnetischen Domänen steht im Vordergrund der Untersuchungen.

Neutronendiffraktometrie liefert folgendes Bild von den Magnetstrukturen der Pyroxene $NaFeSi_2O_6$ und $LiFeSi_2O_6$: In $LiFeSi_2O_6$ gibt es einen magnetischen Phasenübergang bei $18\,K$ unterhalb dessen eine verkantete, antiferromagnetische Ordnung mit magnetischer Raumgruppe $P2_1/c'$ vorliegt. In $NaFeSi_2O_6$ gibt es zwei magnetische Phasenübergänge. Beide Phasen sind inkommensurabel mit Propagationsvektor $\boldsymbol{k} = (0, 0.77, 0)$. Unterhalb von $8\,K$ setzt eine transversale Spindichtewelle mit magnetischen Momenten in der ac-Ebene ein, die sich unterhalb von $6\,K$ in eine helikale Struktur verwandelt, wobei die Momente in der ac-Ebene bleiben. Sphärische Neutronenpolarisationsanalyse zeigt, dass antiferromagnetische Domänen in $LiFeSi_2O_6$ mit einer Kombination von elektrischen und magnetischen Feldern ausgerichtet werden können. Die Magnetstruktur in $LiFeSi_2O_6$ ist toroidal. Daher werden die Ergebnisse im Zusammenhang mit der Ausrichtung toroidaler Domänen diskutiert. Zusätzlich werden die Magnonendispersion und die Spindichte von $LiFeSi_2O_6$ besprochen.

In vielen chiralen Multiferroika kann die Chiralität der Magnetstruktur durch das Anlegen eines elektrischen Feldes umgekehrt werden. Dies ermöglicht das Aufnehmen von Hysteresekurven (chirales Verhältnis gegen elektrisches Feld). Die Untersuchung der Zeitskala dieses Schaltprozesses in $MnWO_4$ mit stroboskopischer, polarisierter Neutronenstreuung zeigt ein überraschend langsames Schaltverhalten im Bereich von $2\,ms$ bis $30\,ms$ und eine starke Temperaturabhängigkeit.

Des weiteren werden statische Hysteresekurven an $TbMnO_3$ und $DyMnO_3$ gezeigt. In $TbMnO_3$ nimmt das Koerzitivfeld linear mit fallender Temperatur zu. In $DyMnO_3$ können Hysteresezyklen nur in der Nähe des ferroelektrischen Phasenübergangs durchlaufen werden. Weitere Untersuchungen an $TbMnO_3$ zeigen, dass der quasi-lock-in des magnetischen Propagationsvektors knapp oberhalb des Einsetzens der chiralen magnetischen Ordnung stattfindet. Der Prop-

agationsvektor verändert sich zusätzlich linear mit isotropem Druck. Röntgen-Einkristalldiffraktometrie an $TbMnO_3$ und $DyMnO_3$ zeigt, dass die Auslenkung der Ionen aus ihrer zentrosymmetrischen Lage in der ferroelektrischen Phase sehr gering ist und unterhalb des Auflösungsvermögens der durchgeführten Messungen liegt.

Contents

1 Multiferroics

As the term *multiferroics* already reveals, it refers to materials which combine several ferroic properties. The three ferroic properties are ferroelectricity, ferromagnetism, and ferroelasticity. A material is called *multiferroic* if two or all three of these properties occur simultaneously in the same phase [1].

A ferroic material is characterised by the fact that it forms domains which exhibit a macroscopic property (e.g. magnetisation) which in turn interacts with a related field and by means of this field can be reversed. A ferromagnetic material possesses a spontaneous magnetisation $\boldsymbol{M}^{\mathrm{sp}}$ that can be switched by an applied magnetic field $\boldsymbol{H}$. A ferroelectric material possesses a spontaneous electric polarisation $\boldsymbol{P}^{\mathrm{sp}}$ that can be switched by an applied electric field $\boldsymbol{E}$. A ferroelastic material displays a spontaneous deformation that can be reversed by an applied mechanical stress [2]. Often the definition of multiferroics is expanded to include antiferromagnetic order which is characterised by ordered magnetic moments which cancel out each other on a microscopic scale and thus prevent a macroscopic magnetisation [3].

The topic of multiferroics gets exciting when the different order parameters do not just coexist but also interact with each other. Nowadays most attention is paid to the *magnetoelectric* coupling which describes the influence of a magnetic field on the electric polarisation $\boldsymbol{P}$ and vice versa the influence of an electric field on the magnetisation $\boldsymbol{M}$. Up to the linear order this relation is given by

$$P_i(\boldsymbol{E}, \boldsymbol{H}) = P_i^{\mathrm{sp}} + \epsilon_0 \chi_{ij}^{\mathrm{el}} E_j + \alpha_{ij} H_j + \dots$$
$$\mu_0 M_j(\boldsymbol{E}, \boldsymbol{H}) = \mu_0 M_j^{\mathrm{sp}} + \mu_0 \chi_{ij}^{\mathrm{mag}} H_i + \alpha_{ij} E_i + \dots$$

Whereas the electric and the magnetic susceptibilities χ_{ij} are symmetric the magnetoelectric tensor α_{ij} is not [4, 5].

The term multiferroics is used predominantly for magnetoelectric multiferroics neglecting ferroelasticity. In spite of this the coupling between ferroelectricity and ferroelasticity – i.e. *piezoelectricity* – was already discovered in 1880 by J. and P. Curie [6] and has found indispensable technical application in electric cigarette lighters, in microphones, and as actuators in atomic force and scanning tunneling microscopes, to name just a few [7].

The magnetoelectric effect on the contrary – even though its existence was pointed out by P. Curie in 1894 [8] – was predicted for Cr_2O_3 not before 1959 by I. Dzyaloshinskii [9] and observed by D. Astrov in 1960 [10] and G. Rado

et al. (1961) [11]. Not much progress was reported on that topic from then until 2003 when research on magnetoelectric multiferroics regained substantial interest. This increase in interest has partly to do with the realisation how useful a magnetoelectric material with a strong magnetisation would be for applications [12–14].

Magnetoelectric materials are often discussed in the context of data storage. Presently, most non-volatile data storage devices exploit the magnetisation of small grains for storing information. The magnetisation of these grains gets reversed by a magnetic field. Generation of magnetic fields involves an electric current which consumes energy, produces heat, and is limited in size due to the coils carrying the current. Conversely, the generation of an electric field requires no constant current and solves all three problems at once. A magnetoelectric material with a sizeable magnetisation could then be used to be written by an electric field and read out by its magnetisation [15]. However, a suitable material has not yet been found. Most magnetoelectrics are antiferromagnets and have a low transition temperature. The reasons for that will be illuminated in the following.

Before moving on, it must be distinguished between *single-phase* and *composite* multiferroics. Single-phase (magnetoelectric) multiferroics combine magnetic and ferroelectric properties intrinsically. Composite multiferroics consist of ferromagnetic and ferroelectric phases which both have also a strong ferroelastic interaction. The magnetoelectric effect is mediated by the strain which is generated in one phase by the application of an electric (magnetic) field and in turn causes magnetisation (polarisation) in the other phase. Regarding future applications these composite multiferroics seem more promising. Anyhow, they are not topic of this thesis which entirely deals with single-phase multiferroics. Considering fundamental physical concepts single-phase multiferroics are the more fascinating. These concepts will be recapitulated in the following [7].

Empirically, ferroelectricity and ferromagnetism seem to exclude each other. The reason for that is found in the microscopic origin of both phenomena. In magnetic materials localised electrons of partly filled d or f shells of transition-metal or rare-earth ions form localised magnetic moments. Exchange interaction between these moments leads to their alignment. Ferroelectricity results from the relative shifts of positive and negative ions which breaks inversion symmetry. The microscopic origins for ferroelectricity are various [16, 17].

In classical ferroelectrics with perovskite structure (e.g. $BaTiO_3$) the transition metal ion is located in the centre of an O_6 octahedron. The electric polarisation is caused by an off-centre shift of the transition metal ion with empty d shell in order to form covalent bonds with one or three of the surrounding oxygens. Due to the empty d shell these ferroelectrics lack localised magnetic moments. Introducing ions with partly filled d shells into such systems seems promising in order to combine ferroelectricity and ferromagnetism (e.g. $BiMnO_3$ or $BiFeO_3$).

However, the interaction of both order phenomena is weak [12, 13, 16].

The examples outlined above are so called *proper* ferroelectrics where structural instability towards the polar state, associated with electron pairing, is the cause of the ferroelectric transition. In *improper* ferroelectrics the ferroelectric transition is a consequence of a more complex lattice distortion or a byproduct of another type of ordering. An example for a complex lattice transition is the *geometric* ferroelectricity in hexagonal manganites (e.g. $YMnO_3$) where the MnO_5 blocks tilt into the polar state. An example for another type of ordering is *charge order* in manganites (e.g. $Pr_{1-x}Ca_xMnO_3$) where charges order non-centrosymmetric and induce electric polarisation [12, 16, 17].

Finally, electric polarisation can be induced by magnetic order. Obviously, strong magnetoelectric interaction can be expected for these compounds. Most of the magnetically induced multiferroics exhibit a spiral magnetic structure. The magnetic order in these systems is highly frustrated and competing interactions between the magnetic moments lead to complex magnetic structures. For that reason the order temperature in these compounds is rather low.

The most prominent representative of such systems is $TbMnO_3$ which was found to be multiferroic in 2003 [18]. This discovery marks the strong rise in enthusiasm for multiferroics. As in the case of $TbMnO_3$, in many of these spiral multiferroics frustration leads to a sequence of magnetic phase transitions which start with a sinusoidal spin-density wave followed by the spiral phase. In the sinusoidal spin-density wave phase the moments are not completely ordered. With regard to minimising its entropy, the system has to find a way to order the remaining moments which may result in a spiral phase. In $TbMnO_3$ a sinusoidal spin-density wave sets in below $42\,K$ and spiral order sets in below $28\,K$ [19]. $TbMnO_3$ is further discussed in Chapter 6.

Observations of the magnetic phase transitions in different multiferroics ($TbMnO_3$ [19], $MnWO_4$ [20], $Ni_3V_2O_8$ [21], $CuFeO_2$ [22, 23]) confirm a sequence of two second-order magnetic phase transitions. While the first requires a single irreducible representation and is non-polar the second requires two irreducible representations and is polar. Only the second transition breaks the remaining symmetries and generates the ferroelectric phase [24]. $NaFeSi_2O_6$ seems to be an exception of this rule as discussed in Chapter 4.

Spiral magnetic order is distinguished between *helical* and *cycloidal* arrangement of the magnetic moments. In a helical spiral the moments rotate in a plane perpendicular to the propagation vector while in a cycloidal spiral the propagation vector lies within the rotation plane of the spins. Both spirals break inversion symmetry and may thus induce electric polarisation. A sinusoidal spin-density wave on the contrary does not break inversion symmetry and cannot induce ferroelectricity.

Among the spiral spin arrangements especially the cycloid is known to induce ferroelectricity. The microscopic mechanism for that involves the antisymmetric

Dzyaloshinskii-Moriya interaction and was considered in References [25] and [26]. The Dzyaloshinskii-Moriya interaction between neighbouring moments is given by $\boldsymbol{D}_{ij} \cdot \boldsymbol{S}_i \times \boldsymbol{S}_j$ and favours non-collinear spin arrangement. The exchange interaction between neighbouring moments is usually mediated via super-exchange by oxygen ions forming bonds between pairs of transition metal ions. The bond angle determines the angle between the spins. In order to minimise the energy the Dzyaloshinskii-Moriya interaction can now inversely act on the bond angle and thereby shift the oxygens away from their centrosymmetric position. This mechanism is therefore called *inverse Dzyaloshinskii-Moriya interaction*. The displacement of the oxygen ions leads to electric polarisation which is given by

$$\boldsymbol{P} \propto \sum_{ij} \boldsymbol{e}_{ij} \times (\boldsymbol{S}_i \times \boldsymbol{S}_j) \tag{1.1}$$

where $\boldsymbol{e}_{ij}$ points along the connection lines of the corresponding ions [17]. For the cycloidal spiral the connection line $\boldsymbol{e}_{ij}$ is perpendicular to the cross product $\boldsymbol{S}_i \times \boldsymbol{S}_j$ and a finite electric polarisation is induced. Cycloidal magnetic order can account for ferroelectricity in $R\text{MnO}_3$ ($R =$ Tb, Dy, etc.) [19, 27, 28] (Chapter 6 & 7), MnWO_4 [29–31] (Chapter 5), $\text{Ni}_3\text{V}_2\text{O}_8$ [32] etc.

For the helical spiral $\boldsymbol{e}_{ij}$ is parallel to $\boldsymbol{S}_i \times \boldsymbol{S}_j$ and thus no polarisation is induced by the mechanism of Equation (1.1). Nevertheless there are examples of materials with helical magnetic structure which exhibit ferroelectricity, among them CuFeO_2 [23], $\text{Cu}_3\text{Nb}_2\text{O}_8$ [33], and $\text{NaFeSi}_2\text{O}_6$ (Chapter 4). These compounds have in common that they have a rather low crystal symmetry ($\bar{1}$ or $2/m$). The helical magnetic structure further reduces the symmetry by breaking inversion and mirror operations. The only symmetry operations in accordance with helical magnetic structures are rotation axes. Electric polarisation is in accordance with rotation axes as long as the polarisation is parallel to them (polar axis). Once the symmetry operations which prevent the crystal from being ferroelectric are broken, the ions are prone shift into a polar state and ferroelectricity sets in [23, 33].

Another mechanism, which does not require spiral magnetic order and thus can account for ferroelectricity even in collinear spin arrangements, is the *exchange striction*. The energy between neighbouring spins is given by $\boldsymbol{S}_i \cdot \boldsymbol{S}_j$. In a frustrated magnetic structure the exchange striction shifts ions in a way to optimise their exchange energy. For example in a chain with nearest-neighbour ferromagnetic and next-nearest-neighbour antiferromagnetic interaction the moments with parallel spin will move closer together which may break inversion symmetry and generate electric polarisation [16, 17, 34]. Exchange striction is argued to be the predominant mechanism for ferroelectricity in YMn_2O_5 [34, 35]. YMn_2O_5 is discussed in Chapter 8.

Considering the three well established ferroic properties under their behaviour of the inversion of space and time gives the following picture. Ferroelasticity is invariant against space and time inversion. Ferromagnetism is invariant against

space inversion but changes sign upon time inversion. Ferroelectricity changes sign upon space inversion but is invariant against time inversion. It is then a natural expansion to consider also a ferroic order parameter which breaks both space and time inversion. Ferrotoroidicity is claimed to be the fourth ferroic order parameter which fulfils the desired symmetry behaviour. The toroidal moment $\boldsymbol{t}$ of a bulk material with localised magnetic moments is given by the sum over all the magnetic moments $\boldsymbol{m}_\alpha$ and the cross product with their position vectors $\boldsymbol{r}_\alpha$ with respect to some origin

$$\boldsymbol{t} = \frac{1}{2} \sum_\alpha \boldsymbol{r}_\alpha \times \boldsymbol{m}_\alpha$$

Naturally this quantity fulfils the desired symmetry behaviour. The ferrotoroidal state can be visualised as an array of spin vortices [36, 37].

Ferrotoroidal domains in a crystal are not necessarily identical to the antiferromagnetic domains in the same crystal. A reversal of all magnetic moments in an antiferromagnetic domain however results in inversion of the toroidal moment. Therefore it is questionable whether the toroidal moment can be considered as an independent ferroic state. In order to exhibit a toroidal moment a crystal must have an antiferromagnetic structure which additionally breaks inversion symmetry. Crystals with an antiferromagnetic structure known to give rise to a toroidal moment are $LiCoPO_4$ [38] and $LiFeSi_2O_6$ (Chapter 3).

In magnetoelectric materials it is possible to manipulate the antiferromagnetic structure by means of an electric field. Especially in materials with spiral magnetic structure it is possible to reverse the sense of rotation of the spiral [39]. A microscopic method is required for observing antiferromagnetic domains. So far two methods are available: optical second harmonic generation (SHG) [40] and spherical neutron-polarisation analysis. The fundamentals of polarised neutron scattering are reviewed in detail in Chapter 2.

2 Polarised Neutron Scattering

This chapter covers essential neutron-scattering formulas. Rather than giving a general introduction on the entire theory of neutron scattering, it is restricted to the formulas essentially used in this thesis. The main attention is thus directed to elastic polarised neutron scattering. General knowledge of scattering theory (i.e. elementary X-ray scattering) is assumed.

The neutron-scattering experiments presented in this thesis have been performed at the *Institut Laue-Langevin* (*ILL*) in Grenoble, at the *Laboratoire Léon Brillouin* (*LLB*) in Saclay (Paris), and at the *Forschungsreaktor München II* (*FRM II*) in Garching.

2.1 The Structure Factor

For elastic neutron scattering the length of the wave vector is retained during the scattering event $k_{\mathrm{i}} = k_{\mathrm{f}} = \frac{2\pi}{\lambda}$, i.e. the neutrons do not gain or yield energy to the crystal. The scattering vector is defined as the momentum transfer on the crystal due to the scattering process

$$\boldsymbol{Q} = \boldsymbol{k}_{\mathrm{i}} - \boldsymbol{k}_{\mathrm{f}} \tag{2.1}$$

$Q = 4\pi \frac{\sin\theta}{\lambda}$. Constructive interference is achieved only when the scattering vector is equal to a reciprocal lattice vector $\boldsymbol{G}$

$$\boldsymbol{Q} = \boldsymbol{G} \tag{2.2}$$

Equations (2.1) and (2.2) yield the Bragg equation

$$2\boldsymbol{k} \cdot \boldsymbol{G} = \boldsymbol{G}^2$$

which is commonly written as

$$2d\sin\theta = n\lambda$$

The intensity of the scattered neutrons I is proportional to the absolute square of the structure factor N. The nuclear structure factor N is the Fourier transform of the nuclei distribution, it is given by

$$N(\boldsymbol{Q}) = \sum_j b_j \, \mathrm{e}^{\mathrm{i}\boldsymbol{Q}\cdot\boldsymbol{r}_j} \, \mathrm{e}^{-W_j(\boldsymbol{Q})}$$

The sum runs over all nuclei j in the unit cell of the crystal. b is the coherent scattering length of the corresponding nucleus which is in the range of 1 to 10 fm. All values are listed in [41, 42]. The scattering length of an element depends on the isotope and on the orientation of the nuclear spin with respect to the neutron's spin. It is a reasonable assumption that isotopes and nuclear spin are distributed randomly. They can therefore not contribute to the interference effect which assumes perfect periodicity of the scattering centres. The coherent scattering length b_c is the mean value of the scattering lengths of the element averaged over the various possible isotopes and spin orientations. The uncorrelated distribution of the isotopes and the spins contributes to the so called incoherent scattering which is isotropic (i.e. it is independent of Q). Thus it adds to the background uniformly and can be neglected for most neutron-scattering experiments.

The Debye-Waller factor $\mathrm{e}^{-W(\boldsymbol{Q})} = \exp(-\frac{Q^2 U}{2}) = \exp(-B\frac{\sin^2\theta}{\lambda^2}) = \exp(-\frac{B}{4d^2})$ describes the effect of thermal motion on the intensity of the coherent scattering. There are two common expressions for the temperature factor which are related by $B_{\mathrm{iso}} = 8\pi^2 U_{\mathrm{iso}}$. Thermal fluctuations of the nuclei about their equilibrium position diminish the intensity of the scattered neutrons. But where do these neutrons go? They must still exist because the amount of incident neutrons must equal the amount of final neurons except for absorption due to neutron capture. Due to the statistical nature of the thermal fluctuations the crystal structure deviates from its periodic alignment. As in the case of incoherent scattering by the different isotopes and spins the thermal motion contributes to the background uniformly.

2.1.1 Magnetic Scattering

In analogy to the nuclear structure factor the magnetic structure factor for non-modulated structures (i.e. propagation vector $\boldsymbol{k} = \boldsymbol{0}$) is given by

$$\boldsymbol{M}(\boldsymbol{Q}) = p \sum_j f_j^{\mathrm{mag}}(\boldsymbol{Q})\, \boldsymbol{m}_j\, \mathrm{e}^{\mathrm{i}\boldsymbol{Q}\cdot\boldsymbol{r}_j}\, \mathrm{e}^{-W_j(\boldsymbol{Q})}$$

The magnetic form factor $f^{\mathrm{mag}}(\boldsymbol{Q})$ represents the magnetisation distribution within a single magnetic ion. Its values are listed in [41, 42]. $\boldsymbol{m}$ is the magnetic moment in units of μ_{B}. The constant $p = 2.695\,\mathrm{fm}/\mu_{\mathrm{B}}$ relates the scattering length for a single magnetic moment of $1\,\mu_{\mathrm{B}}$ at $Q = 0$ to the nuclear scattering length b which is in the range of 1 to 10 fm. Therefore magnetic scattering is of the same magnitude as nuclear scattering or may eventually exceed it for large magnetic moments ($\sim 10\,\mu_{\mathrm{B}}$) as in rare earths. The magnetic interaction vector $\boldsymbol{M}_\perp$ is the part of the magnetic structure factor $\boldsymbol{M}$ perpendicular to $\boldsymbol{Q}$

$$\boldsymbol{M}_\perp = \hat{\boldsymbol{Q}} \times (\boldsymbol{M} \times \hat{\boldsymbol{Q}}) \tag{2.3}$$

Only that perpendicular part contributes to the scattered intensity. The intensity is proportional to the absolute square of the magnetic interaction vector. When

magnetic and nuclear scattering peaks occur in the same position (as they do for $\boldsymbol{k} = \boldsymbol{0}$) the coherence between the magnetic and nuclear scattering amplitudes must be considered. In the case of unpolarised neutrons there is no coherence and the magnetic and nuclear intensities are additive.

$$I = |N|^2 + |\boldsymbol{M}_\perp|^2 \tag{2.4}$$

Modulated Magnetic Structures

For modulated structures (i.e. propagation vector $\boldsymbol{k} \neq \boldsymbol{0}$) the formulas get slightly more complicated. The magnetic moment distribution $\boldsymbol{m}_{lj}$ can be Fourier expanded

$$\boldsymbol{m}_{lj} = \sum_{\boldsymbol{k}} \mathbf{m}_{\boldsymbol{k}j} \, \mathrm{e}^{-\mathrm{i}(\boldsymbol{k}\cdot\boldsymbol{R}_l + \phi_{\boldsymbol{k}j})} \tag{2.5}$$

The Fourier components $\mathbf{m}_{\boldsymbol{k}j}$ are in general complex vectors. The sum runs over all propagation vectors, usually $\boldsymbol{k}_1 = \boldsymbol{k}$ and $\boldsymbol{k}_2 = -\boldsymbol{k}$. A necessary condition for the magnetic moments $\boldsymbol{m}_{lj}$ to be real is $\mathbf{m}_{-\boldsymbol{k}} = \mathbf{m}_{\boldsymbol{k}}^*$, where * denotes complex conjugation. $\boldsymbol{R}_l$ is the vector which translates the origin of the direct space to the individual unit cell of actual interest. The phase $\phi_{\boldsymbol{k}j} = -\phi_{-\boldsymbol{k}j}$ is not absolutely necessary. In principle any phase between two Fourier components can be determined by the value of the components themselves. However, the equations become more intuitive when regarding two moments which are connected by symmetry. In a centred cell for example the phase $\phi_{\boldsymbol{k}} = \boldsymbol{k} \cdot \boldsymbol{t}$ relates the Fourier component of an ion to the one translated by the centering vector $\boldsymbol{t}$.

Lastly, the magnetic structure factor for magnetic structures with propagation vector reads as

$$\boldsymbol{M}(\boldsymbol{Q} = \boldsymbol{G} + \boldsymbol{k}) = p \sum_{j} f_j^{\mathrm{mag}}(\boldsymbol{Q}) \, \mathbf{m}_{\boldsymbol{k}j} \, \mathrm{e}^{\mathrm{i}(\boldsymbol{Q}\cdot\boldsymbol{r}_j - \phi_{\boldsymbol{k}j})} \, \mathrm{e}^{-W_j(\boldsymbol{Q})}$$

This summary is based on text books [41–47].

2.2 Polarised Neutron Scattering

As mentioned earlier for unpolarised neutrons no coherence between magnetic and nuclear scattering has to be considered. In other words useful information can be gained by the use of polarised neutrons. Even when magnetic and nuclear scattering peaks do not occur in the same position ($\boldsymbol{k} \neq \boldsymbol{0}$) useful information about the magnetic structure can be acquired by the use of polarised neutrons.

For a given axis of quantisation the neutron's spin can be aligned either parallel ($+$) or antiparallel ($-$). The polarisation of the neutron beam with respect to an

arbitrarily chosen axis ($i = x, y, z$) is then defined as

$$P_i = \frac{N_i - N_{\bar{i}}}{N_i + N_{\bar{i}}} \tag{2.6}$$

where N_i is the number of neutrons with spin parallel to the axis i. In a completely unpolarised neutron beam there are equal amounts of both spin configurations, hence $P = 0$. A completely polarised beam has polarisation $P = \pm 1$.

It is useful to define a right handed, orthogonal coordinate system with respect to the scattering vector $\boldsymbol{x} \, \| (-\boldsymbol{Q})$. $\boldsymbol{z}$ is chosen to be vertical on the scattering plane and $\boldsymbol{y} = \boldsymbol{z} \times \boldsymbol{x}$ completes the right handed system. The usefulness of this definition becomes immediately obvious when regarding the magnetic interaction vector which now writes as $\boldsymbol{M}_\perp = (0, M_y, M_z)^\mathsf{T}$.

The polarisation of the incident neutron beam along some arbitrary axis is given by $\boldsymbol{P} = (P_x, P_y, P_z)^\mathsf{T}$. The scattered intensity under the condition that the incoming neutron beam is polarised is

$$I = NN^* + \boldsymbol{M}_\perp \cdot \boldsymbol{M}_\perp^* + \boldsymbol{P} \cdot \boldsymbol{M}_\perp N^* + \boldsymbol{P} \cdot \boldsymbol{M}_\perp^* N - \mathrm{i}\boldsymbol{P} \cdot (\boldsymbol{M}_\perp \times \boldsymbol{M}_\perp^*) \tag{2.7}$$

For unpolarised neutrons ($\boldsymbol{P} = \boldsymbol{0}$) Equation (2.7) results in Equation (2.4).

In the most general case one is interested in the polarisation P'_{ij} of the scattered intensity I_{ij} along some axis j under the condition that the incident neutron beam was polarised along i. Likewise to Equation (2.6) the scattered polarisation is defined as

$$P'_{ij} = \frac{I_{ij} - I_{i\bar{j}}}{I_{ij} + I_{i\bar{j}}} \tag{2.8}$$

and $\boldsymbol{P}'_i = (P'_{ix}, P'_{iy}, P'_{iz})^\mathsf{T}$. The sum ($I_i$ the scattered intensity when incident polarisation is parallel i)

$$I_i = I_{ij} + I_{i\bar{j}} \tag{2.9}$$

must hold as the neutron spin must be either up or down. Equation (2.8) and Equation (2.9) yield

$$I_{ij} = \frac{1}{2}(I_i + P'_{ij}I_i) \tag{2.10}$$

which is a useful expression once $P'_{ij}I_i$ is available. This quantity is in fact given by

$$\begin{aligned} \boldsymbol{P}'I = {}& \boldsymbol{P}(NN^* - \boldsymbol{M}_\perp \cdot \boldsymbol{M}_\perp^*) \\ & + \boldsymbol{M}_\perp(\boldsymbol{P} \cdot \boldsymbol{M}_\perp^*) + \boldsymbol{M}_\perp^*(\boldsymbol{P} \cdot \boldsymbol{M}_\perp) + \boldsymbol{M}_\perp N^* + \boldsymbol{M}_\perp^* N \\ & - \mathrm{i}\boldsymbol{P} \times (\boldsymbol{M}_\perp N^* - \boldsymbol{M}_\perp^* N) + \mathrm{i}(\boldsymbol{M}_\perp \times \boldsymbol{M}_\perp^*) \end{aligned} \tag{2.11}$$

Equations (2.7) and (2.11) are called the Blume-Maleev equations. They were derived simultaneously and independently by the physicists M. Blume and

S. Maleev et al. in the early 1960's [48, 49]. However, for better understanding an article of P. J. Brown [50] is recommended. Table 2.1 summarises all of the 36 possible channels of neutron-polarisation analysis. The different contributions are classified depending on their origin as nuclear, magnetic, chiral magnetic and nuclear magnetic interference term.

Two simple rules which in many cases are sufficient and provide greater insight can be deduced from the complete set of equations: *(I.) Components of the magnetic moment which are parallel to the neutron polarisation produce non-spin-flip scattering, while those perpendicular to the neutron polarisation produce spin-flip scattering. (II.) Hence, if the neutron polarisation is along the scattering vector, all magnetic scattering is spin-flip scattering* [51].

It is useful to summarise the polarisations in a matrix-like notation

$$\boldsymbol{\mathcal{P}}' = (\boldsymbol{P}'_x, \boldsymbol{P}'_y, \boldsymbol{P}'_z) = \begin{pmatrix} P'_{xx} & P'_{yx} & P'_{zx} \\ P'_{xy} & P'_{yy} & P'_{zy} \\ P'_{xz} & P'_{yz} & P'_{zz} \end{pmatrix} \qquad (2.12)$$

with P'_i as columns. Note that just 18 of the intensity channels contribute to this kind of matrix.

I_{ij}		nuclear		magnetic	chiral magnetic	nuc. magn. interference
xx	$=$	NN^*				
$x\bar{x}$	$=$			$\boldsymbol{M}_\perp \cdot \boldsymbol{M}_\perp^*$	$- \, \mathrm{i}(\boldsymbol{M}_\perp \times \boldsymbol{M}_\perp^*)_x$	
$\bar{x}x$	$=$			$\boldsymbol{M}_\perp \cdot \boldsymbol{M}_\perp^*$	$+ \, \mathrm{i}(\boldsymbol{M}_\perp \times \boldsymbol{M}_\perp^*)_x$	
$\bar{x}\bar{x}$	$=$	NN^*				
yy	$=$	NN^*	$+$	$M_y M_y^*$		$+ \quad 2\Re(M_y^* N)$
$y\bar{y}$	$=$			$M_z M_z^*$		
$\bar{y}y$	$=$			$M_z M_z^*$		
$\bar{y}\bar{y}$	$=$	NN^*	$+$	$M_y M_y^*$		$- \quad 2\Re(M_y^* N)$
zz	$=$	NN^*	$+$	$M_z M_z^*$		$+ \quad 2\Re(M_z^* N)$
$z\bar{z}$	$=$			$M_y M_y^*$		
$\bar{z}z$	$=$			$M_y M_y^*$		
$\bar{z}\bar{z}$	$=$	NN^*	$+$	$M_z M_z^*$		$- \quad 2\Re(M_z^* N)$
$xy = y\bar{x} =$		$^1/_2(NN^*$	$+$	$\boldsymbol{M}_\perp \cdot \boldsymbol{M}_\perp^*$	$- \, \mathrm{i}(\boldsymbol{M}_\perp \times \boldsymbol{M}_\perp^*)_x$	$+ \, 2\Re(M_y^* N) + 2\Im(M_z^* N))$
$x\bar{y} = \bar{y}\bar{x} =$		$^1/_2(NN^*$	$+$	$\boldsymbol{M}_\perp \cdot \boldsymbol{M}_\perp^*$	$- \, \mathrm{i}(\boldsymbol{M}_\perp \times \boldsymbol{M}_\perp^*)_x$	$- \, 2\Re(M_y^* N) - 2\Im(M_z^* N))$
$\bar{x}y = yx =$		$^1/_2(NN^*$	$+$	$\boldsymbol{M}_\perp \cdot \boldsymbol{M}_\perp^*$	$+ \, \mathrm{i}(\boldsymbol{M}_\perp \times \boldsymbol{M}_\perp^*)_x$	$+ \, 2\Re(M_y^* N) - 2\Im(M_z^* N))$
$\bar{x}\bar{y} = \bar{y}x =$		$^1/_2(NN^*$	$+$	$\boldsymbol{M}_\perp \cdot \boldsymbol{M}_\perp^*$	$+ \, \mathrm{i}(\boldsymbol{M}_\perp \times \boldsymbol{M}_\perp^*)_x$	$- \, 2\Re(M_y^* N) + 2\Im(M_z^* N))$
$xz = z\bar{x} =$		$^1/_2(NN^*$	$+$	$\boldsymbol{M}_\perp \cdot \boldsymbol{M}_\perp^*$	$- \, \mathrm{i}(\boldsymbol{M}_\perp \times \boldsymbol{M}_\perp^*)_x$	$+ \, 2\Re(M_z^* N) - 2\Im(M_y^* N))$
$x\bar{z} = \bar{z}\bar{x} =$		$^1/_2(NN^*$	$+$	$\boldsymbol{M}_\perp \cdot \boldsymbol{M}_\perp^*$	$- \, \mathrm{i}(\boldsymbol{M}_\perp \times \boldsymbol{M}_\perp^*)_x$	$- \, 2\Re(M_z^* N) + 2\Im(M_y^* N))$
$\bar{x}z = zx =$		$^1/_2(NN^*$	$+$	$\boldsymbol{M}_\perp \cdot \boldsymbol{M}_\perp^*$	$+ \, \mathrm{i}(\boldsymbol{M}_\perp \times \boldsymbol{M}_\perp^*)_x$	$+ \, 2\Re(M_z^* N) + 2\Im(M_y^* N))$
$\bar{x}\bar{z} = \bar{z}x =$		$^1/_2(NN^*$	$+$	$\boldsymbol{M}_\perp \cdot \boldsymbol{M}_\perp^*$	$+ \, \mathrm{i}(\boldsymbol{M}_\perp \times \boldsymbol{M}_\perp^*)_x$	$- \, 2\Re(M_z^* N) - 2\Im(M_y^* N))$
$yz = zy =$		$^1/_2(NN^*$	$+ \, \boldsymbol{M}_\perp \cdot \boldsymbol{M}_\perp^* + 2\Re(M_y M_z^*)$			$+ \, 2\Re(M_y^* N) + 2\Re(M_z^* N))$
$y\bar{z} = \bar{z}y =$		$^1/_2(NN^*$	$+ \, \boldsymbol{M}_\perp \cdot \boldsymbol{M}_\perp^* - 2\Re(M_y M_z^*)$			$+ \, 2\Re(M_y^* N) - 2\Re(M_z^* N))$
$\bar{y}z = z\bar{y} =$		$^1/_2(NN^*$	$+ \, \boldsymbol{M}_\perp \cdot \boldsymbol{M}_\perp^* - 2\Re(M_y M_z^*)$			$- \, 2\Re(M_y^* N) + 2\Re(M_z^* N))$
$\bar{y}\bar{z} = \bar{z}\bar{y} =$		$^1/_2(NN^*$	$+ \, \boldsymbol{M}_\perp \cdot \boldsymbol{M}_\perp^* + 2\Re(M_y M_z^*)$			$- \, 2\Re(M_y^* N) - 2\Re(M_z^* N))$

Table 2.1: Intensity of all 36 possible channels of neutron-polarisation analysis. [52]

2.2.1 Chiral Magnetic Structures

The concept of chirality is most intuitively introduced by considering human hands (Greek: χειρ, hand). The mirror image (enantiomorph) of the right hand is the left hand and it is not possible to bring both hands to coincident by the use of pure rotation or translation operations. Lord Kelvin introduced the term *chirality* in 1904. Generally an object can be defined to be chiral, if it is not superposable by pure rotation or translation on its mirror image [53].[1] Chirality is an important property in nature. Enantiomers (enantiomorphs of molecules) often smell and taste differently.

An object is chiral, if its point group contains no symmetry elements like inversions ($\bar{1}$), mirrors (m), and rotoinversions ($\bar{n}$). The point group must contain only pure rotations (n). Chirality depends on the dimension of the space. A chiral object in two dimensions, such as the palm of the hand, becomes achiral in three dimensions, since the plane containing the two-dimensional object becomes then a mirror symmetry.[2]

Before we move on to chirality of magnetic structures we must consider the action of symmetry operations on magnetic moments. We can imagine a magnetic moment as an infinitesimal current loop. Time inversion ($1'$) will therefore reverse the direction of the current and thus the direction of the magnetic moment. In an analogous manner we can investigate how the current loop reacts on spatial symmetry operations. This is a tedious exercise. The results can best be summarised by introducing the concept of polar and axial vectors. For this purpose we write the symmetry operation as an orthogonal 3×3 matrix. The symmetry operations can then be classified as *proper*, $\det(\boldsymbol{\alpha}) = 1$ (real rotation), and *improper*, $\det(\boldsymbol{\alpha}) = -1$ (inversion, refection). When the vector is polar (e.g. the electric dipole moment) it transforms as $g(\boldsymbol{p}) = \boldsymbol{\alpha} \cdot \boldsymbol{p}$. When the vector is axial (e.g. the magnetic dipole moment) it transforms as $g(\boldsymbol{a}) = \det(\boldsymbol{\alpha})\,\boldsymbol{\alpha} \cdot \boldsymbol{a}$.

The complexity of the term chirality comes along when considering dynamical aspects (here current loops i.e. magnetic moments) as in the following example. A parallel arrangement of a magnetic and an electric dipole moment $\uparrow_m \uparrow_e$ seems to be a chiral object as both moments become antiparallel $\downarrow_e \uparrow_m$ under space inversion and are not superposable onto each other. However, the same configuration can be obtained, by time inversion combined with a two-fold rotation. The former given definition of chirality gives no clear answer how to deal with time inversion. L. Barron introduces the term *true chirality*: *True chirality is possessed by sys-*

---

[1]In crystallography (restricted to three dimensions) it is customary to define an object as chiral, if it is not superposable by pure rotation or translation on its image gained by inversion. (The equivalence of both definitions becomes obvious when remembering that a mirror is a combination of a spatial inversion and a two-fold rotation, $m = \bar{2}$.)

[2]If we do not distinguish any more between the palm of the hand and its back we can superimpose the right and the left hand if we flip on hand.

tems that exist in two distinct enantiomeric states that are interconverted by space inversion but not by time reversal combined with any proper spatial rotation [54].

When dealing with magnetic structures we have an intuitive understanding of the sense of spin rotation. It is customary to associate this sense of spin rotation to some value. A suitable value is the *vector chirality*

$$\boldsymbol{\chi} = \boldsymbol{S}_i \times \boldsymbol{S}_j$$

determined by two consecutive spins $\boldsymbol{S}_i$ and $\boldsymbol{S}_j$ on an oriented path. The behaviour of the vector chirality will now be discussed in regard of two most prominent magnetic structures with a sense of rotation: the helical and the cycloidal magnetic structure.

Helical magnetic structure means the propagation vector is perpendicular to the plane of rotation of the magnetic moments so that the connection line of the magnetic moments forms a helix (also referred to as screw type magnetic structures). Space inversion produces two enantiomorphs with spins rotating in the opposite sense around the axis of the helix. Neither time inversion nor rotation about any axis does change the sense of spin rotation. Thus a helix shows true chirality according to Barron. The vector chirality for both enantiomorphs has opposite sign and is in accordance of our intuitive understanding.

Cycloidal magnetic structure means the propagation vector lies in the plane of rotation of the magnetic moments so that the connection line of the magnetic moments forms a cycloid. Again, space inversion produces two configurations with spins rotating in the opposite sense in the plane. However a two-fold rotation about an axis either perpendicular to the rotation plane of the spins or parallel to the propagation vector produces the same configuration (modulo a translation). Obviously, such an object is not chiral. This behaviour is a consequence of the cycloid being a two-dimensional object in three-dimensional space. Nevertheless it is possible to unambiguously assign distinct vector chiralities to both configurations.

An excellent review on chirality is given by V. Simonet, M. Loire, and R. Ballou [55].

In many multiferroic materials with spiral magnetic structure[3] the microscopic origin of the ferroelectricity is the inverse Dzyaloshinskii-Moriya interaction. The direction of the electric polarisation $\boldsymbol{P}$ is given by $\boldsymbol{P} \propto \sum_{ij} \boldsymbol{e}_{ij} \times (\boldsymbol{S}_i \times \boldsymbol{S}_j)$ where $\boldsymbol{S}_i$ and $\boldsymbol{S}_j$ are the magnetic moments of neighbouring magnetic ions and $\boldsymbol{e}_{ij}$ points along the connection line of the corresponding ions.

---

[3]**Spiral magnetic structure** is used as a collective term for helical, cycloidal and mixed types of spin arrangements.

We recognise the term $\boldsymbol{S}_i \times \boldsymbol{S}_j$ as the vector chirality. It is non-zero only for non-collinear spin arrangements. In particular sinusoidal spin-density waves yield a vanishing cross product of neighbouring magnetic moments.

Neutron scattering with polarised neutrons suggests itself for studying magnetic structures with a non-vanishing term $\boldsymbol{S}_i \times \boldsymbol{S}_j$ as it gives access to the so called *chiral term*: $-\mathrm{i}(\boldsymbol{M}_\perp \times \boldsymbol{M}_\perp^*)_x$. The *chiral ratio* is defined as

$$r_\chi = \frac{-\mathrm{i}(\boldsymbol{M}_\perp \times \boldsymbol{M}_\perp^*)_x}{|\boldsymbol{M}_\perp|^2}$$

As we learn from Table 2.1 the chiral ratio can be measured likewise in several channels of the neutron polarisation. The strongest intensity can be detected in the channel $I_{x\bar{x}} = |\boldsymbol{M}_\perp|^2 - \mathrm{i}(\boldsymbol{M}_\perp \times \boldsymbol{M}_\perp^*)_x$ and $I_{\bar{x}x} = |\boldsymbol{M}_\perp|^2 + \mathrm{i}(\boldsymbol{M}_\perp \times \boldsymbol{M}_\perp^*)_x$:

$$r_\chi = \frac{I_{x\bar{x}} - I_{\bar{x}x}}{I_{x\bar{x}} + I_{\bar{x}x}} \tag{2.13}$$

In order to observe the chiral term and the chiral ratio the scattering vector must have a component perpendicular to the rotation plane of the magnetic moments. Only if the scattering vector is exactly perpendicular to this rotation plane chiral ratios of ± 1 are possible[4]

2.2.2 The Flipping Ratio

When undertaking a neutron-scattering experiment with polarised neutrons the quality of the polarisation of the incoming beam is an important factor as all scattering results will depend on it. The polarisation was given by Equation (2.6): $P_i = \frac{N_i - N_{\bar{i}}}{N_i + N_{\bar{i}}}$. A polarisation of 1 is desired yet experimentally not obtainable, of course. So N_i represents the number of the 'good' neutrons whose spin is aligned properly while $N_{\bar{i}}$ represents the number of the 'bad' neutrons whose spin is misaligned. Another frequently used quantity is the flipping ratio which is defined as

$$\mathrm{FR} = \frac{N_i}{N_{\bar{i}}}$$

The flipping ratio and the polarisation are connected by the following relations:

$$\mathrm{FR} = \frac{1 + P}{1 - P} \qquad P = \frac{\mathrm{FR} - 1}{\mathrm{FR} + 1}$$

Under good experimental conditions a flipping ratio of 40 is readily achieved, but at 20 reasonable results still can be obtained (polarisation of ~ 0.95 and ~ 0.90, respectively).

---

[4]Proof: In our notation $\boldsymbol{Q} \,\|\, (-\boldsymbol{x})$. Imagine an arbitrary spiral magnetic structure with the scattering vector in the plane of rotation of the magnetic moments. Without loss of generality we choose $\boldsymbol{M} = M_x \boldsymbol{x} + M_y \boldsymbol{y}$. Obviously $\boldsymbol{M}_\perp = M_y \boldsymbol{y}$. It follows $\boldsymbol{M}_\perp \times \boldsymbol{M}_\perp^* = \boldsymbol{0}$. Now let the scattering vector be perpendicular to the plane of rotation: $\boldsymbol{M} = M_y \boldsymbol{y} + M_z \boldsymbol{z}$. It follows $\boldsymbol{M}_\perp = M_y \boldsymbol{y} + M_z \boldsymbol{z}$, but now $\boldsymbol{M}_\perp \times \boldsymbol{M}_\perp^* = (M_y M_z^* - M_y^* M_z)\boldsymbol{x}$.

2.2.3 History of Polarised Neutrons

The existence of the neutron was predicted by E. Rutherford in 1920 in order to explain the nuclear constitution of atoms [56]. The neutron was proposed as a neutral particle consisting of close combination of a proton and an electron. A concept which was elaborated in the theory of β decay of the neutron by E. Fermi in 1934 [57]. It was J. Chadwick who experimentally verified its existence in 1932 [58, 59]. Although since its discovery it was generally accepted that the neutron is a spin-$1/2$ particle [60, 61] it lasted till 1947 until an unambiguous experimental proof was delivered [62]. The magnetic moment of the neutron was postulated already in 1934 [63]. In 1936, short after their discovery, it was shown that neutrons could be diffracted by crystals [64]. It was the same year when F. Bloch pointed out that neutrons will scatter from an atom not only on account of the interaction of the neutron with the atomic nucleus but also on account of the interaction of the neutron's magnetic moment with the magnetic moment of the atom [65]. In 1937 J. Schwinger gave a more detailed theory on an unpolarised beam of neutrons which will be partially polarised after being transmitted through a ferromagnet [66]. Experimentally this was accomplished 1938 [67, 68]. O. Halpern and M. Johnson advanced the theory of magnetic neutron scattering and placed special emphasis upon questions of polarisation (1937-1939) [69–71]. Again, Bloch together with L. Alvarez determined the magnetic moment of the neutron by polarisation analysis in 1940 [72]. The first determination of a magnetic structure was carried out in a pioneering experiment by C. Shull and J. Smart in 1949 on antiferromagnetic MnO [73]. In 1951 complete polarisation of the neutron beam by reflection of neutrons from magnetised mirrors was reported [74]. In the same year complete polarisation by Bragg scattering on antiferromagnetic magnetite (Fe_3O_4) was achieved by Shull et al. [75]. In 1959 the first measurement with polarised neutrons was carried out and the magnetic form factors of nickel and iron were determined [76, 77]. In this experiment the incident neutron beam was polarised either parallel or antiparallel to the magnetisation of the scattering crystal and the corresponding intensities were compared. A general theory of polarised neutron scattering was published simultaneously and independently by the physicists M. Blume and S. Maleev et al. in 1963 [48, 49]. In contrast to the former theory by Halpern and Johnson, which was restricted to ferromagnetic and simple antiferromagnetic structures, no restrictions were made. As a consequence interesting polarisation effects in the case of scattering by spiral spin structures were henceforth computable.

In 1969 the development of the first triple-axis spectrometer with *uniaxial (longitudinal)* polarisation analysis was reported by R. Moon, T. Riste and W. Koehler [51]. They installed a polariser before and polarisation analysis behind the sample. The direction of polarisation could be chosen to be perpendicular or parallel to the scattering vector. Due to the need of a continuous magnetic guide field from

the polariser to the analyser the polarisation and analysis were always parallel or antiparallel, hence the term *uniaxial*. The instrument allowed to choose the spin state of the incident beam to be $(+)$ or $(-)$ and equally the spin state of the scattered beam to be $(+)$ or $(-)$. This way for either polarisation axis ($\boldsymbol{P} \perp \boldsymbol{Q}$ or $\boldsymbol{P} \parallel \boldsymbol{Q}$) four scattering amplitudes were available.

The guide field is necessary to preserve the neutron polarisation. Without guide field small fields as the earth's magnetic field will disturb the original polarisation of the beam as the neutron spin will precess about the field direction leaving only the component along the field observable. As Moon et al. [51] already point out, observing the scattered polarisation not in the direction of the incident polarisation, would require a magnetic field which changes direction precisely at the location of the scattering centre. This is of course unfeasible. Another solution to overcome this challenge is to install a zero-field chamber at the position of the scattering centre. The first sophisticated experimental realisation was presented by F. Tasset in 1989 [78]. The *CRYOPAD* (cryogenic polarisation-analysis device) makes use of superconducting Meissner screens to expel any magnetic field from the scattering centre. The guide fields before and after the scattering centre can thus be selected independently. This way any arbitrary spin state for the incident and the scattered beam can be achieved. In comparison to the former methods this technique represents a great improvement. For the first time all polarisation channels summarised in Table 2.1 were available. That is why this method is referred to as *spherical* (*vectorial*, *three-dimensional*) polarisation analysis. The setup of *CRYOPAD* is described in detail in Section 2.3.4.

This historical overview follows a lecture of R. Stewart [79] and an article of J. Schweizer [80].

2.3 Polarised Neutron-Scattering Technique

2.3.1 Polarising the Neutron Beam

There are three different methods of polarising the neutron beam which will be described in the following.

Polarising Crystals

Ferromagnetic single crystals can be used to simultaneously polarise and monochromatise the neutron beam. A magnetic field is applied along the crystal perpendicular to the scattering vector to saturate the magnetic moments along the field direction. For an unpolarised beam $\boldsymbol{P} = \boldsymbol{0}$ the Blume-Maleev equations

(2.7) and (2.11) yield

$$\boldsymbol{P}' = \frac{2\boldsymbol{M}_\perp N}{|N|^2 + |\boldsymbol{M}_\perp|^2} = \frac{2M_z N}{|N|^2 + |M_z|^2}\,\boldsymbol{z}$$

The chiral term $-\mathrm{i}(\boldsymbol{M}_\perp \times \boldsymbol{M}_\perp^*)_x$ is zero for collinear structures. For centrosymmetric and for simple collinear magnetic structures N and $\boldsymbol{M}_\perp$ are real quantities. If the magnetic field aligns all moments along the z direction then $\boldsymbol{M}_\perp = M_z\boldsymbol{z}$. Under the special condition that the nuclear and the magnetic scattering amplitude are of the same magnitude the neutron beam is completely polarised and by reversing the magnetic field it is possible to reverse the neutron polarisation. Suitable crystals are iron single crystals with a special amount of ^{57}Fe and the following alloys $Co_{0.92}Fe_{0.08}$, Cu_2MnAl (Heusler) and Fe_3Si. [79, 81]

Polarising Mirrors

For small scattering angles neutrons experience refraction. The refractive index n of a material is usually slightly smaller than 1 (e.g. $1 - n = 1.5 \cdot 10^{-6}$ for Ni at $\lambda = 1\,$Å). From this it follows that neutrons can experience total reflection at the boundary between the material and the vacuum for very small incident angles, typically $0°10'$. This effect facilitates the construction of neutron guides which allow to transport the neutrons from the reactor to the spectrometer without loss of intensity. By slightly bending the guide it is even possible to eliminate neutrons of higher energy and gamma rays.

For a ferromagnetic material the critical angle differs for both spin states. By choosing a suitable angle it is indeed possible to suppress one spin state and produce a completely polarised beam. Due to the small angle of total reflection a mirror must be a few meters long to produce a beam of a reasonable width.

More practical polarisers can be constructed by alternating several layers of magnetic and non-magnetic material. This way it is possible to tune the critical angle.

A polariser for broader wavelength range can be constructed if these bilayers exhibit a gradient in their thickness. These devices are called supermirrors. Typically they are made from layers of Fe/Si or Co/Ti. To ensure that the neutrons are reflected at least once, the mirror can be gently bent. This device is then called a bender. Polarising multilayers produce a beam of high polarisation. The wavelength is restricted to exceed $2\,$Å however. [44, 79, 81]

Polarising Filters

Polarising filters have different transmissibility for the two spin states. This is on account of either preferential absorption or preferential scattering. The intensity is a trade-off between attenuation and polarisation. Although in principle there

are different isotopes which exhibit this feature the only one of contemporary interest is ^{3}He because it exhibits the strongest difference in the absorption cross-section for the two spin states. One spin state goes through the gas with strong absorption while the other one is less absorbed. The ^{3}He nuclei can be polarised by optical pumping using high power lasers, followed by compression of the gas. Due to collisions with the walls of the container and stray magnetic fields the polarisation of the gas decreases over time. For transport and at the instrument magnetic shielding is employed. Nevertheless the cells have to be replaced about once a day. Usual polarisation for recharged cells is about 0.8. [81]

2.3.2 Guiding the Polarised Neutron Beam

For any experimental implementation utilising polarised neutrons, the action of a magnetic field on the magnetic moment of the neutron has to be taken into account. The magnetic moment of the neutron is given by $\boldsymbol{\mu}_\mathrm{n} = \gamma_\mathrm{n}\boldsymbol{s}$ where the gyromagnetic ratio of the neutron is $\gamma_\mathrm{n} = -2 \cdot 1.91\,\mu_\mathrm{N}/\hbar = -1.83 \cdot 10^8\,\text{/sT}$. $\mu_\mathrm{N} = e\hbar/2m_\mathrm{p} = 5.05 \cdot 10^{-27}\,\text{J/T}$ is the nuclear Bohr magneton. The relation of the nuclear Bohr magneton to the (electron) Bohr magneton is $\mu_\mathrm{N} = \mu_\mathrm{B}/1836$. The z component of the neutron magnetic moment amounts $\mu_{\mathrm{n},z} = \gamma_\mathrm{n}\hbar/2 = -1.91\mu_\mathrm{N} = -9.66 \cdot 10^{-27}\,\text{J/T}$. The relation of the neutron magnetic moment to the electron magnetic moment is $\mu_{\mathrm{n},z} = \mu_{\mathrm{e},z}/961$. [82, 83]

A magnetic field $\boldsymbol{B}$ exerts a torque $\boldsymbol{T}$ on the magnetic moment, $\boldsymbol{T} = \boldsymbol{\mu}_\mathrm{n} \times \boldsymbol{B}$. The time evolution of the spin is thus governed by the following equation

$$\frac{\mathrm{d}\boldsymbol{s}}{\mathrm{d}t} = \gamma_\mathrm{n}\boldsymbol{s} \times \boldsymbol{B}$$

When the spin and the field are parallel in the beginning, the cross product is zero and the spin is preserved. Therefore such a field is called guide field. In the other case the spin precesses about field what can be seen from the general solution of the equation of motion

$$\boldsymbol{s}(t) = \begin{pmatrix} s_{x0}\cos(\omega_\mathrm{L}t) + s_{y0}\sin(\omega_\mathrm{L}t) \\ s_{x0}\sin(\omega_\mathrm{L}t) + s_{y0}\cos(\omega_\mathrm{L}t) \\ s_{z0} \end{pmatrix}$$

with $\boldsymbol{B} = B\boldsymbol{e}_z$ and the Larmor frequency $\omega_\mathrm{L} = \gamma_\mathrm{n}B$.

A guide field is needed to preserve the spin of the neutron. If the guide field rotates slowly in space (mathematical this means $\omega_\mathrm{L}/\omega_B \gg 1$ where ω_B is the rotation of the magnetic field, experimentally this can be accomplished by $\omega_\mathrm{L}/\omega_B > 10$) the spin of the neutron will follow the guide field. This is called *adiabatic* rotation. On the other hand if the guide field changes *non-adiabatically* (i.e. $\omega_\mathrm{L}/\omega_B \ll 1$) the spin begins to precess about the new field direction[5] [50, 80].

---

[5]The calculation for the adiabatic and non-adiabatic rotation is not provided here.

So far the mathematical treatment was for a *classical* spin. For a quantum mechanical spin just one component of the spin is preserved, whilst the other components remain fluctuating. The classical analysis keeps valid however if the former spin is associated with the one component of the spin which is preserved.

The quantum mechanical spin comes along with some counterintuitive features. One easy task is to imagine a neutron whose spin is aligned along the z direction and now will be measured along the y direction. As mentioned before a quantum mechanical spin can have only one fixed component. Subsequently when measuring this spin along the y direction its probability of the being parallel or antiparallel y is $1/2$ each.

Mathematically the probability $P_z(y)$ of finding a spin being prepared in $|z\rangle$ along the y direction is given by the projection $P_z(y) = |\langle y|z\rangle|^2$. In order to calculate this probability we must represent the states $|y\rangle$ and $|z\rangle$ in the eigenvectors of their operators given by the Pauli matrices $s_i = \frac{\hbar}{2}\sigma_i$

$$\sigma_x = \begin{pmatrix} 0 & 1 \\ 1 & 0 \end{pmatrix} \qquad \sigma_y = \begin{pmatrix} 0 & -\mathrm{i} \\ \mathrm{i} & 0 \end{pmatrix} \qquad \sigma_z = \begin{pmatrix} 1 & 0 \\ 0 & -1 \end{pmatrix}$$

With $|y\rangle = \frac{1}{\sqrt{2}} \begin{pmatrix} -\mathrm{i} \\ 1 \end{pmatrix}$ and $|z\rangle = \begin{pmatrix} 1 \\ 0 \end{pmatrix}$ it follows $P_z(y) = |\langle y|z\rangle|^2 = \frac{1}{2}$.

2.3.3 Spin Flippers

Scattering experiments with polarised neutrons usually require turning the neutron spin in the desired direction. Different devices are available. Two of them shall be described here.

Mezei Flipper

The principle of operation of a Mezei Flipper depends on the neutron spin undergoing a well-defined number of Larmor precessions in a fixed magnetic field over a well-defined distance. On entering the magnetic coil of the Mezei flipper the neutron is exposed to a field perpendicular to the guide field. Because the transition to the new field is non-adiabatic the spin starts to precess about the perpendicular field. When it exits the flipping field after performing exactly one rotation of π the spin is flipped. It is then preserved by the guide field which it now opposes. Neutrons of different velocities spend different precession time inside the coil, hence Mezei flippers can be employed for monochromatic beams only. [79, 84, 85]

Current Sheet (Dabs Foil) Flipper

Originally a foil, more advanced a grid of closely aligned copper wires, is introduced into the neutron beam in a way that the neutrons pass through the sheet. A strong

current in the direction of the guide field through the sheet produces a magnetic field perpendicular to the guide field. Right on the two sides of the sheet the magnetic field lines are of opposite direction. Because the foil is thin the neutrons experience a non-adiabatic field change when transmitting the foil. Precession does not occur at that point as the fields are exactly opposing. The superposition of the guide field and the field of the foil generates an ample transition region. It is that region which adiabatically reverses the neutron polarisation. This kind of flipper is independent of the neutron velocity. [79, 84]

2.3.4 CRYOPAD

This section describes the setup of the *CRYOPAD III* (cryogenic polarisation-analysis device) for spherical polarisation analysis. Spherical polarisation analysis allows choosing the direction of the incident and the final polarisation independently and thereby gives access to the full polarisation matrix (2.12). The off-diagonal terms of the polarisation matrix yield valuable information on the nuclear magnetic interference. For the experimental implementation it is necessary to separate the guide fields of the incident and the final neutrons by a zero-field chamber at the position of the scattering centre. The guide fields define the direction of polarisation analysis and may be chosen independently. In the zero-field chamber at the scattering centre the orientation of the spin is maintained. For a precise measurement of the spin direction an abrupt (non-adiabatic) transition into the zero-field region is required. This is accomplished by superconducting Nd-Meissner screens at the beam level, Figure 2.1. In addition, the environmental
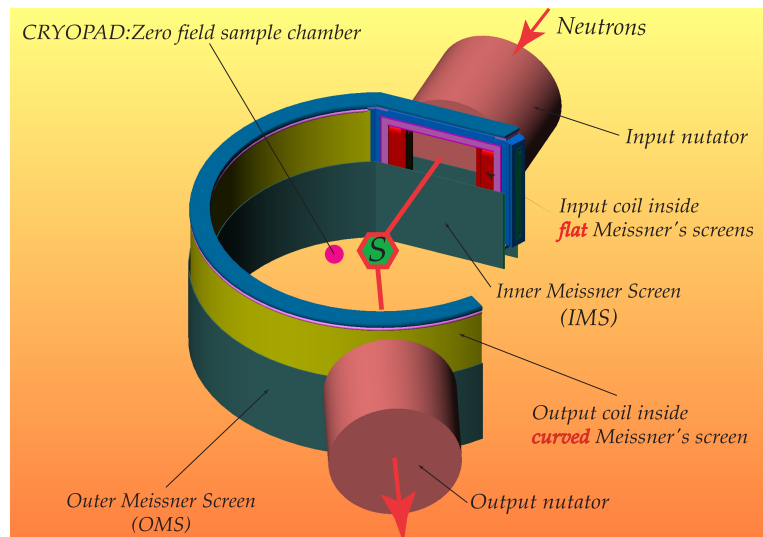

Figure 2.1: *CRYOPAD III* (cryogenic polarisation-analysis device) [86]

magnetic field is expelled from the zero-field chamber by µ-metal screens.

The neutron beam is polarised vertically (z direction) by a polariser (a Heusler monochromator at *IN22* for example). The spin then gets rotated adiabatically along the direction of the incident neuron (x direction) by a guide field parallel $\boldsymbol{k}_i$. Then a *nutator* adiabatically rotates the spin into a plane transverse to the incident neutron (yz plane). The angle between the spin and the vertical z axis can be chosen by rotating the nutator in the yz plane. Behind the nutator the neutron enters the region between the two Meissner screens. Upon passing the outer Meissner screen the magnetic field changes abruptly (non-adiabatically) to a horizontal field perpendicular to the incident neutron (y direction) produced by a superconducting entrance coil. The neutron's spin starts to precess about the magnetic field. Upon passing the inner Meissner screen the Larmor precession stops and the spin maintains its direction in the zero-field. By choosing the nutator angle and the current in the entrace precession coil the spin of the incident neutron can be aligned in any direction desired. After the scattering process the neutron enters the magnetic field of the exit coil between the Meissner screens which is decoupled from the entrance coil. The exit nutator and the guide field adiabatically transport the neutron to the analyser. Because the direction of the spin is unknown after scattering at the sample, only the component parallel to the guide field is preserved while the transverse components precess about the guide field and average to zero. [86–88]

2.4 Time-Resolved Neutron Scattering

Within the scope of this thesis for the first time the kinetics of electric field induced switching of chiral magnetic structures was investigated. On the one hand this is of fundamental research interest, on the other hand multiferroics are often regarded in the context of data storage devices such as non-volatile magnetic random access memory (RAM). For this application the writing speed is a crucial issue. The idea of the applied technique utilising neutron scattering was to instantaneously reverse an electric field up to $\pm 1.5\,\mathrm{kV/mm}$ and detect the response of the magnetic structure as a function of time. When one intends to employ neutron scattering for resolving a process which takes place on the timescale of milliseconds, one faces the problem that counting times for neutrons typically range in the timescale of several minutes. To overcome this challenge stroboscopic neutron-scattering techniques were developed in the group of G. Eckold [89]. With this method it is possible to synchronise a periodically switching electric field at the sample with the count rate of the neutron detector. The signal from the detector is recorded into time slots by a multichannel scaler (MCS). In order to gain sufficient count rates for each time slot the measurement is repeated periodically while the count rates of the individual time slots are accumulated. Obviously this method is limited to reversible processes.

Time resolution is not a standard feature of most neutron spectrometers. With little effort it is however possible to equip a standard neutron spectrometer with time resolution. This task is especially simple when the spectrometer has two monitors available. Monitor 1 is normally used to account for varying neutron flux either due to fluctuations of the reactor power and – more importantly for inelastic measurements only – where the flux may depend on the wavelength of the incoming neutron beam. Monitor 2 is used for inelastic measurements only and is not required for elastic measurements. The external electronics for the time resolution is connected to the spectrometer in the following way: the signal from the neutron detector is fed to the multichannel scaler where it is recorded into time slots synchronised with the electric field at the sample. The input of Monitor 1 is fed with the signal which counts the cycles of the switching process. This way the spectrometer software can handle the number of switching cycles with no need of modification in the spectrometer software. The signal of Monitor 1 is fed to the input of Monitor 2 and is recorded by the spectrometer software for subsequent correction of the neutron flux.

For the measurements in this thesis time resolution was installed on the cold triple-axis spectrometer *IN12* and *IN14* (*ILL*) and at *4F1* (*LLB*). The chiral ratio was obtained by measuring both spin-flip channels in x direction, compare Equation (2.13). Both channels were measured subsequently. All time-resolved measurements were performed in collaboration with J. Leist and G. Eckold.

2.5 Linear Spin-Wave Theory

This section describes how a magnon dispersion can be treated in terms of linear spin-wave theory. In the Heisenberg model [90] the interaction between localised electron spins is mediated by exchange constants J_{ij} between neighbouring electron spins at sites i and j. Obviously $J_{i,j} = J_{j,i}$ and $J_{i,i} = 0$. $J_{\mathrm{F}} > 0$ for ferromagnetic coupling and $J_{\mathrm{AF}} < 0$ for antiferromagnetic coupling. The Heisenberg-Hamilton operator is given by

$$\hat{H} = -\sum_{i,j} J_{i,j} \hat{\boldsymbol{S_i}} \cdot \hat{\boldsymbol{S_j}}$$

Each pair of neighbouring spins is counted twice in this formalism.

In the following the solution of the Heisenberg Hamiltonian will be discussed for a simple ferromagnetic model with nearest-neighbour interaction. The Hamiltonian for next nearest neighbours is rewritten by the use of the ladder operators $\hat{S}^{\pm} = \hat{S}_x \pm \mathrm{i}\hat{S}_y$.

$$\hat{H} = -J \sum_i \sum_{\substack{\delta \\ \mathrm{n.n.}}} \hat{\boldsymbol{S_i}} \cdot \hat{\boldsymbol{S_{i+\delta}}} = -J \sum_i \sum_{\substack{\delta \\ \mathrm{n.n.}}} \left[\frac{1}{2} \left(\hat{S}_i^+ \hat{S}_{i+\delta}^- + \hat{S}_i^- \hat{S}_{i+\delta}^+ \right) + \hat{S}_i^z \hat{S}_{i+\delta}^z \right]$$

The eigenvalues of $\hat{S}^z$ are $\hbar m$ where $m = -S, -S+1, \ldots, S$ and refers to the projection of the spin on the z direction. In the ground state all spins are parallel, i.e. $|\Psi_0\rangle = |S, \ldots, S\rangle$. The energy of the ground state is $E_0 = -NZJS^2$, where N is the number of atoms and Z is the number or nearest neighbours. The effect of the ladder operators is to raise or lower the projection on the z direction. $\hat{S}^\pm |S, m\rangle = \hbar\sqrt{S(S+1) - m(m \pm 1)}|S, m \pm 1\rangle$

Although it is possible to exactly diagonalise this Hamiltonian for such easy systems as the ferromagnet with nearest neighbour interaction it is useful to introduce the Bose operators $\hat{a}$ (annihilation) and $\hat{a}^\dagger$ (creation). This approach was first introduced by T. Holstein and H. Primakoff [91] and is therefore called Holstein-Primakoff transformation. The spin quantum state is now expressed by an occupation number $n = 0, \ldots, 2S$ rather than the spin-quantum number m. $n = 0$ means there is no excitation and the spin is in the ground state with $m = S$, $|\Psi_0\rangle = |0, \ldots, 0\rangle$, generally $n = S - m$. A deviation from the ground state is called a *magnon*. The action of the Bose operators is given by

$$\hat{a}|n\rangle = \sqrt{n}|n-1\rangle, \quad \hat{a}^\dagger|n\rangle = \sqrt{n+1}|n+1\rangle, \quad \hat{a}^\dagger\hat{a}|n\rangle = n|n\rangle,$$
$$[\hat{a}_i, \hat{a}_j^\dagger] = \delta_{ij}, \quad [\hat{a}_i, \hat{a}_j] = [\hat{a}_i^\dagger, \hat{a}_j^\dagger] = 0,$$

$\hat{n} = \hat{a}^\dagger\hat{a}$ is called the number operator. In these equations the restriction $n \leq 2S$ is not incorporated any more, instead n is unlimited. However, for excitations with a few magnons this discrepancy is irrelevant. The ladder operators can be expressed by the Bose operators as follows

$$\hat{S}^+ = \sqrt{2S}\sqrt{1 - \frac{\hat{a}^\dagger\hat{a}}{2S}}\hat{a} \approx \sqrt{2S}\hat{a}, \quad \hat{S}^- = \sqrt{2S}\hat{a}^\dagger\sqrt{1 - \frac{\hat{a}^\dagger\hat{a}}{2S}} \approx \sqrt{2S}\hat{a}^\dagger$$
$$\hat{S}^z = S - \hat{a}^\dagger\hat{a}$$

Again, the approximations relies on the assumption $\langle\hat{n}\rangle \ll 2S$. Especially for a spin-1/2 system this is a crude assumption, which describes the physical properties satisfactorily, however. Substituting the Bose operators and neglecting the quadratic term $n^2 \ll S$ yields the linearised Hamiltonian

$$\hat{H} \approx -JS \sum_i \sum_\delta \left(\hat{a}_{i+\delta}^\dagger\hat{a}_i + \hat{a}_i^\dagger\hat{a}_{i+\delta} - \hat{a}_i^\dagger\hat{a}_i - \hat{a}_{i+\delta}^\dagger\hat{a}_{i+\delta}\right) - NZJS^2$$

The effect of the Hamiltonian on a spin state is to increase the spin state at one site (create a magnon) and to lower it at the neighbouring state (annihilate a magnon). By this means a spin excitation is not located at one atom but propagates through the crystal as *spin wave*. The wave-like behaviour motivates diagonalising the Hamiltonian by Fourier transformation. Substituting

$$\hat{a}_i = \frac{1}{\sqrt{N}}\sum_{\boldsymbol{q}} e^{i\boldsymbol{q}\cdot\boldsymbol{R}_i}\hat{a}_{\boldsymbol{q}}, \quad \hat{a}_i^\dagger = \frac{1}{\sqrt{N}}\sum_{\boldsymbol{q}} e^{-i\boldsymbol{q}\cdot\boldsymbol{R}_i}\hat{a}_{\boldsymbol{q}}^\dagger$$

into the Hamiltonian yields

$$\hat{H} - E_0 = -JS \sum_i \sum_{\boldsymbol{\delta}} \frac{1}{N} \sum_{\boldsymbol{q},\boldsymbol{q}'} \left(\mathrm{e}^{-\mathrm{i}\boldsymbol{q}\cdot(\boldsymbol{R}_i+\boldsymbol{\delta})} \mathrm{e}^{\mathrm{i}\boldsymbol{q}'\cdot\boldsymbol{R}_i} + \mathrm{e}^{-\mathrm{i}\boldsymbol{q}\cdot\boldsymbol{R}_i} \mathrm{e}^{\mathrm{i}\boldsymbol{q}'\cdot(\boldsymbol{R}_i+\boldsymbol{\delta})} \right.$$
$$\left. - \mathrm{e}^{\mathrm{i}(\boldsymbol{q}'-\boldsymbol{q})\cdot\boldsymbol{R}_i} - \mathrm{e}^{\mathrm{i}(\boldsymbol{q}'-\boldsymbol{q})\cdot(\boldsymbol{R}_i+\boldsymbol{\delta})} \right) \hat{a}_{\boldsymbol{q}}^{\dagger}\hat{a}_{\boldsymbol{q}'}$$
$$= -JS \sum_{\boldsymbol{q}} \sum_{\boldsymbol{\delta}} \left(\mathrm{e}^{\mathrm{i}\boldsymbol{q}\cdot\boldsymbol{\delta}} + \mathrm{e}^{-\mathrm{i}\boldsymbol{q}\cdot\boldsymbol{\delta}} - 2 \right) \hat{a}_{\boldsymbol{q}}^{\dagger}\hat{a}_{\boldsymbol{q}}$$
$$= \sum_{\boldsymbol{q}} E_{\boldsymbol{q}} \hat{a}_{\boldsymbol{q}}^{\dagger}\hat{a}_{\boldsymbol{q}}$$

with the energy eigenvalues

$$E_{\boldsymbol{q}} = 2JS \left(Z - \sum_{\boldsymbol{\delta}} \cos(\boldsymbol{q}\cdot\boldsymbol{\delta}) \right)$$

For the second step the identity $\frac{1}{N}\sum_j \mathrm{e}^{\mathrm{i}(\boldsymbol{q}-\boldsymbol{q}')\cdot\boldsymbol{R}_j} = \delta_{\boldsymbol{qq}'}$ was used. For a spin chain with $Z = 2$ and $\delta = -a, +a$ we get $E_q = 4JS(1 - \cos(qa))$. A good introduction to linear spin-wave theory is given in the textbook of G. Czycholl [92].

The generalised Heisenberg-Hamilton operator for n magnetic moments per primitive magnetic unit cell, which are mutually parallel or antiparallel, is given by:

$$\hat{H} = - \sum_{i,j,\alpha,\beta} J_{i\alpha,j\beta} \hat{\boldsymbol{S}}_{i\alpha} \cdot \hat{\boldsymbol{S}}_{j\beta} - \sum_{i,\alpha} \sigma_\alpha A_\alpha \hat{S}_{i\alpha}^z \tag{2.14}$$

The indices $i, j = 0, 1, \ldots, N - 1$ run over all primitive unit cells in the crystal while the indices $\alpha, \beta, \gamma = 0, 1, \ldots, n - 1$ run over all magnetic moments within one of these cells. S_α is the spin quantum number and $\hat{\boldsymbol{S}}_{i\alpha}$ and $\hat{S}_{i\alpha}^z$ are the spin operators of the magnetic ion located at $\boldsymbol{R}_{i\alpha} = \boldsymbol{R}_i + \boldsymbol{r}_\alpha$ where $\boldsymbol{R}_i$ is a lattice translation vector. A_α is a possible anisotropy field collinear to the z direction and $\sigma_\alpha = 1(-1)$ for moments parallel (antiparallel) to the z direction. $\boldsymbol{\sigma} = [\sigma_\alpha \delta_{\alpha\beta}]$ is a diagonal matrix. Obviously $J_{i\alpha,j\beta} = J_{j\beta,i\alpha}$ and $J_{i\alpha,i\alpha} = 0$. The solution of 2.14 is given in the work of A. Sáenz [93]. Introducing the Hermitian matrix

$$\begin{aligned} L_{\boldsymbol{q},\alpha\beta} &= 2 \left(\sigma_\alpha \sum_{i\gamma} J_{i\gamma,0\alpha} \sigma_\gamma S_\gamma + A_\alpha/2 \right) \delta_{\alpha\beta} \\ &\quad - 2\sigma_\alpha \sigma_\beta \sqrt{S_\alpha S_\beta} \sum_i J_{i\beta,0\alpha} \exp\left(\mathrm{i}\boldsymbol{q}\cdot(\boldsymbol{R}_{i\beta} - \boldsymbol{R}_{0\alpha})\right) \end{aligned} \tag{2.15}$$

the energy eigenvalues E_α of (2.14) are given by the eigenvalues of $\boldsymbol{\sigma}\cdot\boldsymbol{L_q}$ denoted μ_α:

$$E_{\boldsymbol{q},\alpha} = |\mu_{\boldsymbol{q},\alpha}| \tag{2.16}$$

3 LiFeSi$_2$O$_6$

LiFeSi$_2$O$_6$ is a member of the pyroxene family with general composition AMSi$_2$O$_6$ (A = mono- or divalent metal, M = di- or trivalent metal) recently shown to exhibit interesting magnetoelectric properties [94]. It crystallises in the monoclinic space group $C2/c$ at room temperature and undergoes a structural phase transition to $P2_1/c$ at 229 K [95, 96]. LiFeSi$_2$O$_6$ is a synthetic analogue to NaFeSi$_2$O$_6$ which exists as natural grown crystal. The crystals of LiFeSi$_2$O$_6$ used for measurements in this thesis were provided by the group of P. Becker of the Insitut für Kristallographie at Universität zu Köln. Large single crystals were grown from melt solvent of the system Li$_2$MoO$_4$−LiVO$_3$.

LiFeSi$_2$O$_6$ shows a single magnetic transition into a commensurate magnetic phase at 18 K [97]. There is no spontaneous ferroelectric polarisation at zero magnetic field but sizeable electric polarisation up to $P_c \approx 20\,\mu$C/m^2 is induced by magnetic fields in the ac plane. Thus LiFeSi$_2$O$_6$ is a material with a strong magnetoelectric effect. The magnetoelectric tensor shows asymmetric off-diagonal components [98].

There have been contradictory reports on the magnetic structure of LiFeSi$_2$O$_6$ basing on powder neutron diffraction [95, 99]. A single-crystal diffraction experiment at *HEIDI* single-crystal diffractometer already reported in the diploma thesis [97] identifies $P2_1/c'$ as the most probable magnetic space group in LiFeSi$_2$O$_6$ con-
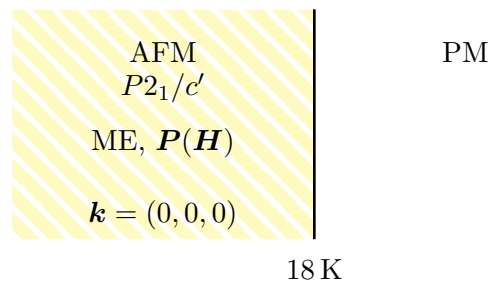
AFM
$P2_1/c'$

ME, $\boldsymbol{P}(\boldsymbol{H})$

$\boldsymbol{k} = (0, 0, 0)$

PM

18 K

Figure 3.1: Magnetic phase diagram of LiFeSi$_2$O$_6$. The moments are collinearly aligned in the ac plane coupled with a b component leading to a canted antiferromagnetic structure. The main part of the moment is along the c direction. Only by applying a magnetic field electric polarisation can be observed. Therefore LiFeSi$_2$O$_6$ is not multiferroic but just magnetoelectric.

sistent with the more recent powder study [99]. Only this magnetic group is in accordance with the finite off-diagonal magnetoelectric coefficients α_{13} and α_{31} [4, 98].[1] The moments are collinearly aligned in the *ac* plane coupled with a *b* component leading to a canted antiferromagnetic structure. The main part of the moment is along the *c* direction.

The largest section of this chapter deals with the poling of antiferromagnetic domains by a combination of electric and magnetic fields. A microscopic method is needed for studying antiferromagnetic domains which spherical neutron-polarisation analysis was utilised for. The result is that it is possible to manipulate antiferromagnetic domains employing different components of the magnetoelectric tensor. The non-centrosymmetric magnetic space group of LiFeSi$_2$O$_6$ gives rise to a toroidal moment. The behaviour of the antiferromagnetic domains is discussed in the context of the toroidal moment.

In addition the magnon dispersion and the spin density were determined.

3.1 Magnetic structure

The magnetic structure of LiFeSi$_2$O$_6$ preliminarily treated in the diploma thesis [97] was revisited in the context of this thesis. An anomaly for reflections with $2\theta > 90°$ was recorded. It seems that for higher angles some part of the Eulerian cradle itself got into the path of the scattered neutrons attenuating the corresponding intensities [101]. For the revisited refinement only reflections with $2\theta < 90°$ were considered. Due to the magnetic form factor reflections at high scattering angle have a low magnetic scattering intensity and are of minor importance for the determination of the magnetic structure anyway.

The space group of LiFeSi$_2$O$_6$ is $P2_1/c$ ($a = 9.6195$ Å, $b = 8.6625$ Å, $a = 5.2630$ Å, $\beta = 109.93°$) [95]. The magnetic structure of LiFeSi$_2$O$_6$ was investigated at *HEIDI* single-crystal diffractometer at the *Forschungsreaktor München II* (*FRM II*) using a point detector and a wavelength of $\lambda = 1.16$ Å. Structural and magnetic peaks were recorded at two temperatures (10 K and 20 K). The lower temperature lies in the antiferromagnetic phase, the higher temperature lies in the paraelectric phase. LiFeSi$_2$O$_6$ shows no magnetic propagation vector. The data were corrected numerically for absorption with *datap*. The structural refinement was done with *FullProf* [102].

At 20 K 925 reflections with $2\theta < 90°$ were collected. 188 of those were equivalent reflections. 54 reflections were rejected. 777 valid independent reflections were used for the refinement. The (weighted) internal R value was 3.29 % (3.64%). The refinement was done with isotropic temperature factors and anisotropic extinction

---

[1]More recent results indicate that the magnetoelectric tensor may have finite entries in all components which would suggest magnetic point groups $P1$ or $P\bar{1}'$. So far it is not clarified whether this applies also in zero magnetic field. [4, 100]
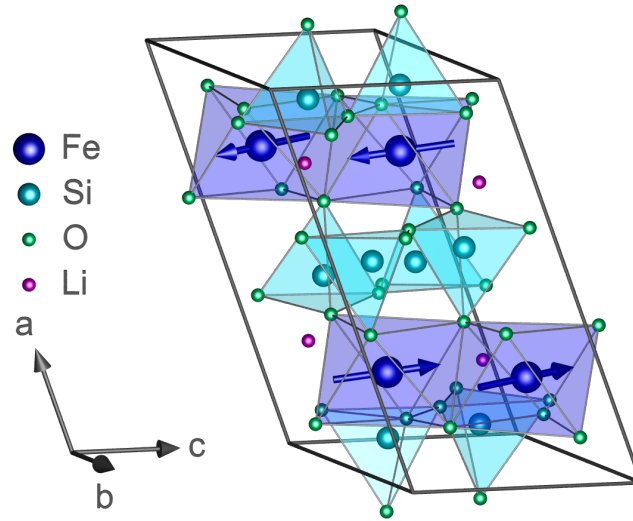
Figure 3.2: Magnetic structure of LiFeSi$_2$O$_6$ as determined at *HEIDI*. Moments are coupled ferromagnetically in the zigzag chains along the c direction and antiferromagnetically between neighbouring chains. The moments are collinearly aligned in the ac plane plus an additional b component leading to a canted antiferromagnetic structure. The main part of the moment is along the c-direction.

correction (model 4 in *FullProf*). The structural parameters and the R values are listed in Table 3.1.

For the magnetic structure a symmetry analysis was employed. There are four irreducible representations in $P2_1/c$. The character table is shown in Table 3.3. The representations belong to the following magnetic space groups: $\Gamma_1 = P2_1/c$, $\Gamma_2 = P2_1/c'$, $\Gamma_3 = P2_1'/c'$, $\Gamma_4 = P2_1'/c$. The symmetry conditions of the four irreducible representations are listed in Table 3.4. The symmetry analysis was done with *BasIreps* [102].

At 10 K 936 reflections with $2\theta < 90°$ were collected. 212 of those were equivalent reflections. 830 valid independent reflections were used for the refinement. The (weighted) internal R value was 1.23 % (1.29%). The refinement was done with isotropic temperature factors and anisotropic extinction correction. The R values are listed in Table 3.2. Undoubtedly $P2_1/c'$ yields the lowest R values. The structural parameters for $P2_1/c'$ are listed in Table 3.1. The structural parameters are consistent for both temperatures within the errors. The magnetic moment is given by $\boldsymbol{M} = (0.58(8),\ 0.69(3),\ 3.91(3))\,\mu_\mathrm{B}$, $M = 3.81(3)\mu_\mathrm{B}$ in a coordinate system with unit vectors parallel to the crystallographic axes. The main part is parallel to the c axis and the moment is canted slightly towards the a and b direction. The structure is a canted antiferromagnet. The results confirm the former results, but are more reliable because the R values are considerably lower. A picture of the crystal and magnetic structure is shown in Figure 3.2.

3 LiFeSi$_2$O$_6$

atom	x	y	z	U_{iso} [Å^2]			
Li	0.2486(5)	0.0066(5)	0.2376(8)	0.0104(9)			
Fe	0.25014(10)	0.64815(10)	0.23462(17)	0.0080(2)	T	$=$	20 K
SiA	0.0478(2)	0.3395(2)	0.2783(4)	0.0072(4)			
SiB	0.5485(2)	0.8392(2)	0.2509(4)	0.0079(4)	R_{F^2}	$=$	5.0 %
O1A	0.86710(16)	0.33254(17)	0.1634(3)	0.0083(3)	R_{wF^2}	$=$	7.8 %
O1B	0.36712(16)	0.83405(17)	0.1338(3)	0.0086(3)	R_F	$=$	4.7 %
O2A	0.11589(15)	0.50899(17)	0.3098(3)	0.0092(3)	$\chi^2(I)$	$=$	17.6
O2B	0.62236(15)	0.00355(17)	0.3543(3)	0.0094(3)			
O3A	0.10887(16)	0.26758(16)	0.5840(3)	0.0087(3)			
O3B	0.60519(16)	0.72238(18)	0.5108(3)	0.0086(3)			
Li	0.2490(5)	0.0071(5)	0.2380(9)	0.0091(9)			
Fe	0.25023(11)	0.64834(10)	0.23441(19)	0.0070(2)	T	$=$	10 K
SiA	0.0478(2)	0.3395(2)	0.2782(4)	0.0065(4)			
SiB	0.5484(2)	0.8393(2)	0.2511(4)	0.0070(4)	R_{F^2}	$=$	5.1 %
O1A	0.86714(17)	0.33274(17)	0.1636(3)	0.0075(3)	R_{wF^2}	$=$	7.7 %
O1B	0.36715(17)	0.83418(17)	0.1338(3)	0.0077(3)	R_F	$=$	4.7 %
O2A	0.11592(16)	0.50906(17)	0.3097(3)	0.0083(3)	$\chi^2(I)$	$=$	16.6
O2B	0.62234(16)	0.00352(18)	0.3545(3)	0.0087(3)			
O3A	0.10873(16)	0.26765(17)	0.5839(3)	0.0078(3)			
O3B	0.60514(16)	0.72229(19)	0.5106(3)	0.0078(3)			

Table 3.1: Structural parameters of LiFeSi$_2$O$_6$ as determined at *HEIDI*.

	$P2_1/c$	$P2_1/c'$	$P2_1'/c'$	$P2_1'/c$
R_{F^2}	7.5%	5.1%	7.7%	7.2%
R_{wF^2}	17.9%	7.7%	18.6%	17.2%
R_F	8.4%	4.7%	8.8%	7.8%
$\chi^2(I)$	89.5	16.6	96.3	82.6

Table 3.2: R values of different magnetic models of LiFeSi$_2$O$_6$ fitted to the data determined at *HEIDI* at 10 K.

	1	2_1	$\bar{1}$	c
Γ_1	1	1	1	1
Γ_2	1	1	-1	-1
Γ_3	1	-1	1	-1
Γ_4	1	-1	-1	1

Table 3.3: Character table of $P2_1/c$.

		x, y, z	$\bar{x}, y+\frac{1}{2}, \bar{z}+\frac{1}{2}$	$\bar{x}, \bar{y}, \bar{z}$	$x, \bar{y}+\frac{1}{2}, z+\frac{1}{2}$
Γ_1	$P2_1/c$	u, v, w	$\bar{u}, v, \bar{w}$	u, v, w	$\bar{u}, v, \bar{w}$
Γ_2	$P2_1/c'$	u, v, w	$\bar{u}, v, \bar{w}$	$\bar{u}, \bar{v}, \bar{w}$	$u, \bar{v}, w$
Γ_3	$P2_1'/c'$	u, v, w	$u, \bar{v}, w$	u, v, w	$u, \bar{v}, w$
Γ_4	$P2_1'/c$	u, v, w	$u, \bar{v}, w$	$\bar{u}, \bar{v}, \bar{w}$	$\bar{u}, v, \bar{w}$

Table 3.4: Symmetry conditions of the four irreducible representations of $P2_1/c$.

3.2 Poling of Antiferromagnetic Domains

Antiferromagnetic magnetic structures form domains. Their most prominent representatives are 180° domains, which are characterised by regions of the crystal in which the direction of the magnetic moments are reversed with respect to the corresponding opposite domain. From symmetry considerations there is no evidence that a magnetic field should prefer either of the two domains. However, if the magnetic structure gives rise to the magnetoelectric effect, a combination of an electric and a magnetic field may break the symmetry and thereby prefer one particular domain.

The magnetoelectric tensor of LiFeSi$_2$O$_6$ was determined by S. Jodlauk [98].

$$\boldsymbol{\alpha} = \begin{pmatrix} 0.60 & \sim 0 & 3.16 \\ \sim 0 & \sim 0 & \sim 0 \\ 0.64 & \sim 0 & 4.86 \end{pmatrix} \frac{\text{ps}}{\text{m}} \qquad (T = 14\,\text{K}) \qquad (3.1)$$

It is derived from the treated data shown in Figure 3.4 which are again derived from the measured data shown in Figure 3.3. As can be learned from the magnetoelectric tensor a magnetic field in the ac plane induces electric polarisation also lying in the ac plane. The biggest effect can be achieved by a magnetic field along c. By an additional electric field it is further possible to choose the direction of the electric polarisation. Due to the magnetoelectric effect the magnetic structure and the electric polarisation are coupled in LiFeSi$_2$O$_6$. Therefore by the application of

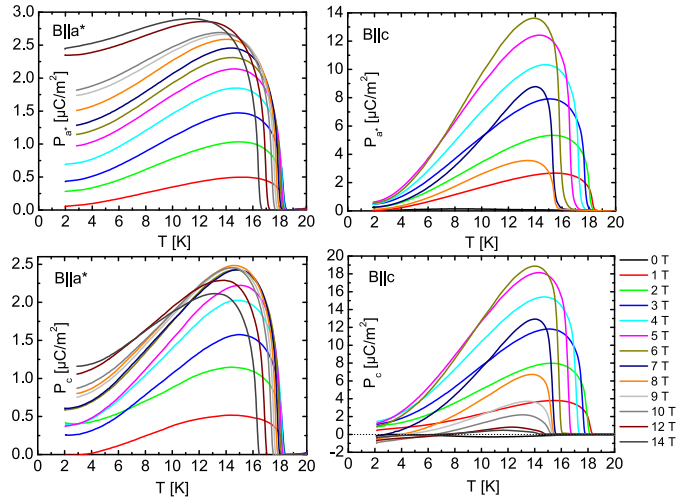**Figure 3.3:** Electric polarisation induced by magnetic field for the four non-zero components of the magnetoelectric tensor of LiFeSi$_2$O$_6$ [98].

a magnetic field and an electric field, both in the *ac* plane, it should be possible to manipulate antiferromagnetic domains.

More recent results indicate that the magnetoelectric tensor may have finite entries in all components. So far it is not clarified whether this applies also in zero magnetic field [100].

A microscopic method is required for observing antiferromagnetic domains. So far two methods are available: optical second harmonic generation (SHG) [40] and spherical neutron-polarisation analysis. Poling of antiferromagnetic domains by cooling below the magnetic phase transition in parallel magnetic and electric fields has been studied with polarised neutrons in Cr$_2$O$_3$ [103] and in crossed electric and magnetic fields in LiCoPO$_4$, MnGeO$_3$ [104], and MnPS$_3$ [105].

By the use of spherical polarisation analysis the different antiferromagnetic domains can be distinguished via the nuclear-magnetic interference terms (Table 2.1). The reversion of the magnetic moments results in a different sign of the magnetic structure factor. For structures with non-zero propagation vector structural and magnetic intensities do not superimpose. As a consequence only squares of the magnetic structure factor contribute to the magnetic intensity and thus different domains cannot be distinguished. However, if the propagation vector is zero, nuclear and magnetic intensities superimpose giving rise to nuclear-magnetic interference terms. These terms consist of the product of the nuclear and the magnetic structure factor (not their squares), hence opposite domains are distinguishable by measuring the neuron polarisation in the corresponding channels. Only monodomain crystals yield the full neutron polarisation. The intensity and polarisation in a multidomain crystal will be the average of the contributions of the two domains weighted by their populations. [50]
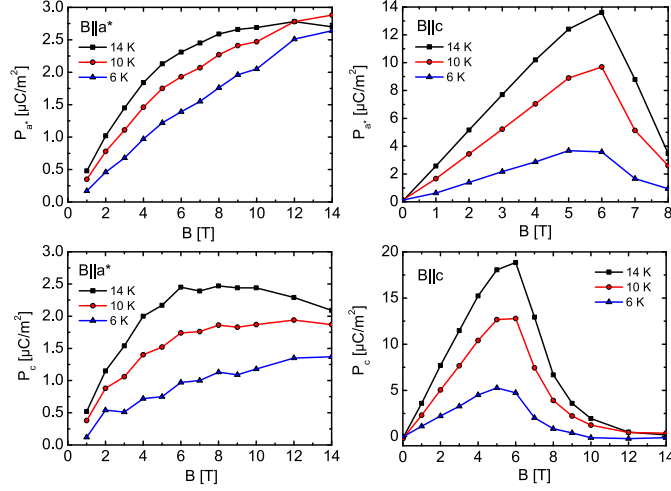
Figure 3.4: Electric polarisation as function of the magnetic field for the four non-zero components of the magnetoelectric tensor of LiFeSi$_2$O$_6$ as derived from the data in Figure 3.3 [98].

The full neutron polarisation is given by the Blume-Maleev equations (2.7) and (2.11). By implementing the equations and the structure factors into a *Python* code and a systematic search in the two scattering planes $(1\,0\,0)/(0\,1\,0)$ and $(0\,1\,0)/(0\,0\,1)$ the reflections $(3\,0\,0)$ and $(0\,3\,1)$ were found to be suitable candidates for investigating the poling of antiferromagnetic domains. Because of the nuclear structure having an inversion centre and the magnetic structure having an inversion centre composed with time reversal, N is real and $\boldsymbol{M}_\perp$ is purely imaginary. Both reflections are extinct in the high-temperature nuclear phase due to the C centring. At the $(3\,0\,0)$ reflection the b component of the magnetic moment does not contribute, thus $\boldsymbol{M}_\perp$ only has a finite z component $M_z = im_z$ with m_z being real. Hence $\Im(M_z^*N) = -m_zN$ and $\Re(M_z^*N) = 0$. At the $(0\,3\,1)$ reflection the b component of the magnetic moment yields only a minor contribution[2]. Both components $M_y = im_y$ and $M_z = im_z$ are purely imaginary. Hence $\Im(M_y^*N) = -m_yN$, $\Im(M_z^*N) = -m_zN$, $\Re(M_yM_z^*) = m_ym_z$, and $\Re(M_y^*N) = \Re(M_z^*N) = 0$. Also there is no chiral contribution $-i(\boldsymbol{M}_\perp \times \boldsymbol{M}_\perp^*)_x = 0$ for any reflection. Following these preliminary considerations the complete polarisation matrices can be derived:

$$\boldsymbol{\mathcal{P}}'_{(3\,0\,0)} = \frac{1}{N^2 + m_z^2} \begin{pmatrix} N^2 - m_z^2 & 2Nm_z & 0 \\ -2Nm_z & N^2 - m_z^2 & 0 \\ 0 & 0 & N^2 + m_z^2 \end{pmatrix}$$

---

[2]Note the b component is not to be confused with the y component. While b refers to the coordinate system of the crystallographic unit cell, y refers to the coordinate system attached to the scattering vector $\boldsymbol{Q}$.

$$\boldsymbol{\mathcal{P}}'_{(0\,3\,1)} = \frac{1}{N^2 + m_y^2 + m_z^2} \begin{pmatrix} N^2 - m_y^2 - m_z^2 & 2Nm_z & -2Nm_y \\ -2Nm_z & N^2 + m_y^2 - m_z^2 & 2Nm_ym_z \\ 2Nm_y & 2Nm_ym_z & N^2 - m_y^2 + m_z^2 \end{pmatrix}$$

The magnetic structure factors of both antiferromagnetic domains have opposing signs. Therefore those components of the polarisation matrix, which are a linear function of the magnetic structure factor, have opposing signs for the different domains. With the nuclear and magnetic structure given in Section 3.1 the polarisation matrices for the two reflections and both antiferromagnetic domains are

$$\boldsymbol{\mathcal{P}}'_{(3\,0\,0)} = \begin{pmatrix} -0.997 & \mp 0.077 & 0 \\ \pm 0.077 & -0.997 & 0 \\ 0 & 0 & 1 \end{pmatrix}$$

$$\boldsymbol{\mathcal{P}}'_{(0\,3\,1)} = \begin{pmatrix} 0.134 & \pm 0.230 & \pm 0.964 \\ \mp 0.230 & 0.953 & -0.195 \\ \mp 0.964 & -0.195 & 0.180 \end{pmatrix}$$

3.2.1 Experimental
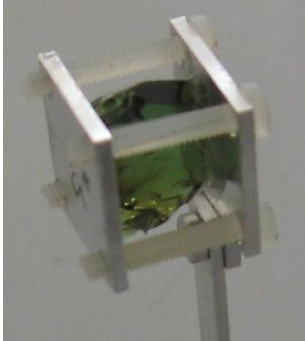
Figure 3.5: Sample holder of LiFeSi$_2$O$_6$.

Two samples were prepared: one in the $(1\,0\,0)/(0\,1\,0)$ scattering plane and one in the $(0\,1\,0)/(0\,0\,1)$ scattering plane. For the first sample an electric field was applied parallel to the crystallographic a^* axis by inserting the plate-shaped single crystalline sample of synthetic LiFeSi$_2$O$_6$ between two thin aluminium plates so that the crystal-plate normal b was parallel to the aluminium plates and the c axis vertical. The sample was glued in between these plates, which were further stabilized by nylon screws, see Figure 3.5. The second sample was fixed with plate normal b parallel to the aluminium plates again but this time the a axis was vertical. The distance of the aluminium plates measured 8 mm for both samples. Unfortunately spherical polarisation analysis cannot be performed with a magnetic field at the sample position, as the neutron spin would precess about the field direction and thereby only the component parallel to the magnetic field would be preserved. The measurement was carried out with the CRYOPAD in which the magnetic field is expelled from the sample position. The poling of the antiferromagnetic domains thus could not be studied in situ, but the sample needed to be cooled in the electric and magnetic field below the magnetic transition outside of the CRYOPAD. The cold sample then was inserted into the CRYOPAD and the neutron polarisation was determined. The sample with the capacitor was mounted in a cryostat with a sufficiently thin tail to enter both the CRYOPAD and an external magnet.

The experiment was realised during two beam times at the *Institut Laue-Langevin*. In the first experiment the reflection $(3\,0\,0)$ was investigated at the cold triple-axis spectrometer *IN14*. In the second experiment the reflection $(0\,3\,1)$ was investigated at the thermal triple-axis spectrometer *IN22*. The following table shows which configurations of electric and magnetic fields were realised.

IN14	$(3\,0\,0)$	$E \parallel a^*$				$B \parallel c$
IN22	$(0\,3\,1)$	$E \parallel c^*$	$B \parallel a$	$B \parallel b$	$B \parallel c^*$

$(\boldsymbol{E} \parallel \boldsymbol{a}^*) \perp (\boldsymbol{B} \parallel \boldsymbol{c})$

The first experiment was performed at *IN14*. The neutron wave vector was set to $k = 1.5\,\text{Å}^{-1}$. The sample was cooled outside the spectrometer in crossed electric and magnetic fields. An electric field of $E = +0.25\,\text{kV/mm}$ was applied along the a^* axis while a magnetic field of $B = +1\,\text{T}$ was applied along the c axis. At a temperature of $10\,\text{K}$ both fields were removed and the cold sample was transferred to the spectrometer and the CRYOPAD.

The first measurement of the polarisation matrix at the $(3\,0\,0)$ reflection after the above-described cooling in crossed fields yields

$$\boldsymbol{\mathcal{P}}'_{(3\,0\,0),+E+B} = \begin{pmatrix} -0.924 & -0.067 & 0.005 \\ 0.057 & -0.919 & 0.005 \\ 0.005 & 0.020 & 0.925 \end{pmatrix}$$

Inspecting the data one notices that the zz-channel is not 1 as it should be according to theory. This is not due to a lack in statistics but reflects the precision of polarisation control. A polarisation of 0.925 corresponds to a flipping ratio of 26. It is not easy, if not impossible, to correct for this. A poor attempt is made by multiplying all polarisations by a factor of $1/0.925$. The result is

$$\boldsymbol{\mathcal{P}}'_{(3\,0\,0),+E+B} = \begin{pmatrix} -0.998 & -0.072 & 0.005 \\ 0.061 & -0.993 & 0.005 \\ 0.006 & 0.022 & 1.000 \end{pmatrix}$$

The four channels which should be zero give us a chance to estimate the error. Their mean is 0.01. So an error of ± 0.01 can be estimated.

Repeating the measurement by reversing the magnetic field only, $+E$, $-B$ yields (correction already applied)

$$\boldsymbol{\mathcal{P}}'_{(3\,0\,0),+E-B} = \begin{pmatrix} -0.999 & 0.041 & -0.003 \\ -0.043 & -0.998 & 0.007 \\ 0.011 & 0.026 & 1.000 \end{pmatrix}$$

These two polarisation matrices clearly show the expected inversion of the two polarisation channels xy and yx although the poling appears to be slightly less

E	B	P'_{xy}	P'_{yx}
$+$	$+$	0.061	-0.072
$+$	$-$	-0.043	0.041
$-$	$-$	0.045	-0.058
$+$	0	-0.005	0.002
$-$	0	-0.006	-0.004
0	$-$	-0.016	0.007

Table 3.5: Neutron polarisation at $(3\,0\,0)$ as function of different cooling fields. The sample was cooled from $33\,\mathrm{K}$ to $10\,\mathrm{K}$ in $(E \parallel a^*) = \pm 0.25\,\mathrm{kV/mm}$ and $(B \parallel c) = \pm 1\,\mathrm{T}$.

perfect for the second run. The good agreement between the calculated and experimental polarisation matrix unambiguously shows, that it is possible to control the antiferromagnetic domains in LiFeSi$_2$O$_6$ by crossed electric and magnetic fields similar to the usual control of ferroic order.

The next measurement was done with both fields being reversed, $-E$, $-B$, yielding $\mathcal{P}'_{xy} = 0.045$ and $\mathcal{P}'_{yx} = -0.058$, which as expected correspond to the same domain structure as for the $+E$, $+B$ run. Furthermore, it was verified that it is not possible to pole the domains in LiFeSi$_2$O$_6$ by applying just one field, either magnetic or electric. The experimental data are summarised in Table 3.5.

Figure 3.6 shows the temperature dependence of the magnetic Bragg peak intensity $xy = \frac{1}{2}(N^2 + m_z^2 - 2Nm_z)$ and $x\bar{y} = \frac{1}{2}(N^2 + m_z^2 + 2Nm_z)$ and the polarisation $P'_{xy} = (xy - x\bar{y})/(xy + x\bar{y}) = -2Nm_z/(N^2 + m_z^2)$ computed from
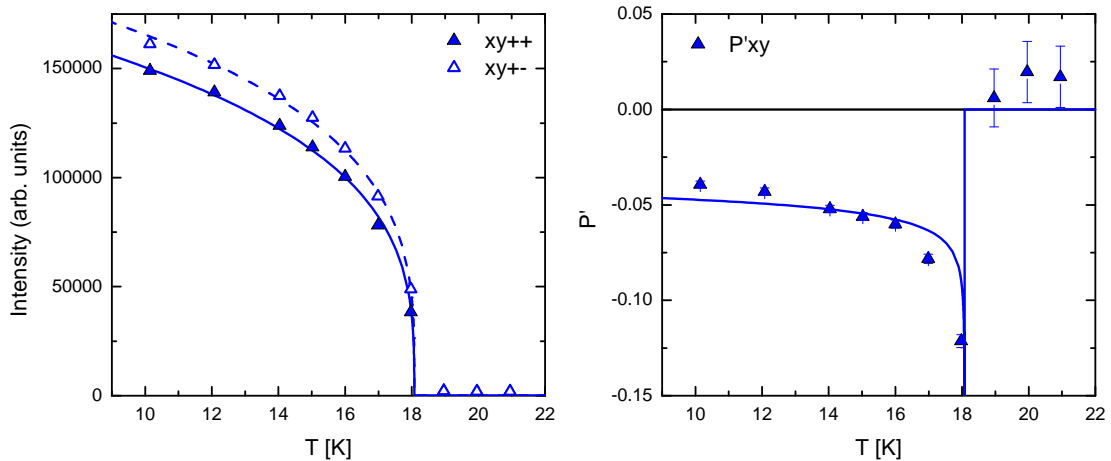

Figure 3.6: Temperature dependence of the intensities in the xy and the $x\bar{y}$ channel of the $(3\,0\,0)$ reflection and that of the neutron polarisation P'_{xy} computed from these intensities recorded after cooling in crossed fields $(+E \parallel a^*)$ and $(-B \parallel c)$. The temperature was increased during this measurement.

these intensities. It was recorded after the second cooling cycle in $+E$, $-B$. The temperature was heated from $10\,\mathrm{K}$ to $22\,\mathrm{K}$ during this measurement. The intensities xy and $x\bar{y}$ can be fitted simultaneously by assuming a temperature independent nuclear contribution N and describing the temperature dependence of the magnetic contribution by $m_z = m_{z0}(1 - \frac{T}{T_\mathrm{N}})^\beta$ [106]: $m_{z0} = 632(4)$, $N = 13(1)$, $T_\mathrm{N} = 18.07(2)\,\mathrm{K}$, $\beta = 0.146(5)$. The same parameters satisfactorily describe the temperature dependence of the neutron polarisation, too.

$(\boldsymbol{E} \parallel \boldsymbol{c}^*) \perp (\boldsymbol{B} \parallel \boldsymbol{a})$

The second experiment was performed at *IN22*. The neutron wave vector was set to $k = 2.66\,\text{Å}^{-1}$. An electric field of $E = \pm 0.25\,\mathrm{kV/mm}$ was applied along the c^* axis while a magnetic field of $B = \pm 1\,\mathrm{T}$ was applied along the a, b, and c^* axes. For each configuration of the fields the sample was cooled from $30\,\mathrm{K}$ to $14\,\mathrm{K}$ or $12\,\mathrm{K}$. For most configurations the complete neutron polarisation matrix at the reflection $(0\,3\,1)$ was recorded. A complete polarisation matrix was recorded in the paramagnetic phase at $30\,\mathrm{K}$ and can be used to determine the accuracy of the measurement. The values on the diagonal give the polarisation of the neutron beam $(\mathrm{FR} = 9)$ while the off-diagonal values should be zero.

$$\boldsymbol{\mathcal{P}}'_{(0\,3\,1),\ 30\,\mathrm{K}} = \begin{pmatrix} 0.805 & -0.003 & 0.016 \\ 0.040 & 0.804 & -0.025 \\ -0.009 & 0.020 & 0.808 \end{pmatrix}$$

For the magnetic field along a all four combinations of the field directions were examined. The complete polarisation matrices are given in Table 3.6. For $+E$

	$+B$			$-B$		
$+E$	0.311	−0.130	−0.505	0.310	0.152	0.581
	0.142	0.766	−0.159	−0.127	0.807	−0.107
	0.519	−0.107	0.330	−0.579	−0.115	0.338
$-E$	0.224	0.026	0.160	0.310	−0.047	−0.137
	−0.024	0.777	−0.134	0.054	0.786	−0.138
	−0.147	−0.120	0.254	0.147	−0.109	0.336
$E = 0$	0.234	−0.077	−0.267			
	0.073	0.784	−0.153			
	0.277	−0.130	0.263			

Table 3.6: Neutron polarisation matrices at $(0\,3\,1)$ after field cooling in $(E \parallel c^*) = \pm 0.25\,\mathrm{kV/mm}$ and $(B \parallel a) = \pm 1\,\mathrm{T}$ from $30\,\mathrm{K}$ to $14\,\mathrm{K}$.

(0 3 1)			(0 3 $\bar{1}$)			(0 $\bar{3}$ $\bar{1}$)		
0.310	0.152	0.581	0.324	−0.166	−0.598	0.310	−0.112	0.594
−0.127	0.807	−0.107	0.185	0.802	−0.152	0.143	0.783	0.110
−0.579	−0.115	0.338	0.600	−0.135	0.373	−0.586	0.122	0.329

Table 3.7: Neutron polarisation matrices of equivalent reflections to (0 3 1) after field cooling in $(E \parallel c^*) = +0.25\,$kV/mm and $(B \parallel a) = -1\,$T from 30 K to 14 K.

with both directions of the magnetic field polarisation higher than 0.5 can be achieved for the xz and zx channel. The sign of the channel xy resembles the sign of the channel xz according to the predicted values. The same holds for yx and zx. The symmetry of the polarisation matrix is fulfilled to a high degree and the values are conform to the theoretical predictions. No corrections had to be applied to the data in order to see this. For $-E$ the polarisation is less perfect for both directions of the magnetic field. Nevertheless the signs of the relevant polarisation channels follow the electric and magnetic fields. Clearly the sample has a preferred direction for one direction of the electric field. Thus it is not surprising that even by applying solely a magnetic field a polarisation approximately half as strong as with $+E$ and even exceeding the polarisation for $-E$ can be achieved. This is a direct consequence of the preferred direction of this sample. Poling with solely a magnetic field was not possible for the other sample previously examined at *IN14*.

Two equivalent reflections of (0 3 1) were examined during one cooling cycle, see Table 3.7. The arrangement of the signs and the values is in perfect accordance with the theory.

The temperature dependence of the neutron polarisation was investigated. The sample was cooled from 30 K to 14 K in $E = +0.25\,$kV/mm and $B = -1\,$T. Then the temperature was increased to 23 K while the neutron polarisation was measured. Again the intensities were fitted ($m_{y0} = -106(4)$, $m_{z0} = 22(2)$, $T_{\mathrm{N}} = 18.13(8)\,$K, $\beta = 0.29(2)$). The same parameters describe the polarisation well. The polarisation data are shown in the left panel of Figure 3.7.

Another temperature dependence was recorded after cooling in $E = -0.25\,$kV/mm and $B = +1\,$T. The polarisation is less perfect as usual for negative electric field. The polarisation was recorded while the sample was heated from 12 K to 30 K. Thereafter the sample was cooled again to 14 K while an opposite electric field $E = +0.25\,$kV/mm was applied . The magnetic field was zero. During heating the polarisation shows the familiar power-law dependence. No neutron polarisation develops during cooling. This demonstrates that an electric field solely is not sufficient to pole the antiferromagnetic domains. After heating the poled sample into the paramagnetic regime the sample develops approximately an equal population of the two antiferromagnetic domains upon re-entering the magnetic phase.
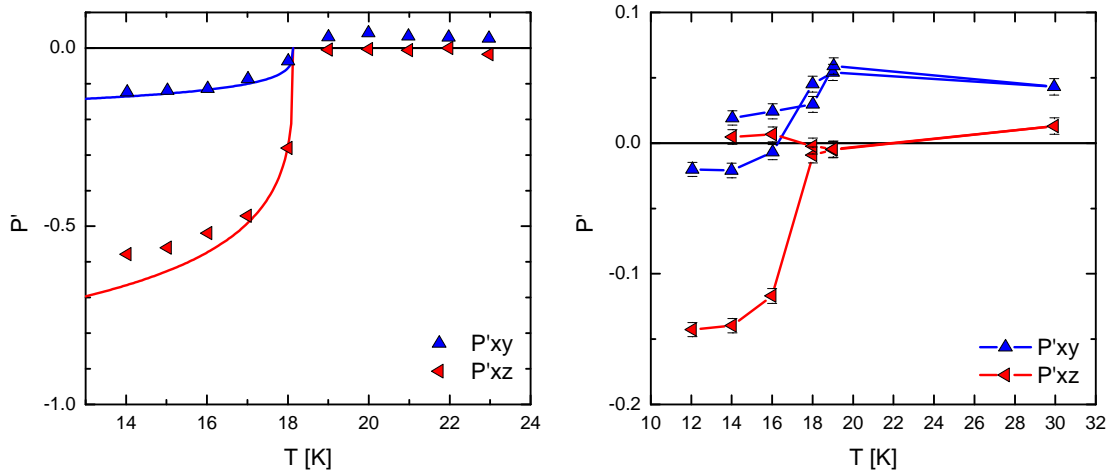
Figure 3.7: Temperature dependence at $(0\,3\,1)$. Left: The sample was field cooled in $(E \parallel c^*) = +0.25\,\text{kV/mm}$ and $(B \parallel a) = -1\,\text{T}$. Then during heating the neutron polarisation was recorded. Right: The sample was field cooled in $(E \parallel c^*) = -0.25\,\text{kV/mm}$ and $(B \parallel a) = +1\,\text{T}$. Then the polarisation was measured during heating from $12\,\text{K}$ to $30\,\text{K}$ and re-cooling to $14\,\text{K}$ with opposite electric field $E = +0.25\,\text{kV/mm}$ and zero magnetic field. The re-cooled sample does not give rise to neutron polarisation which means that both antiferromagnetic domains are equally populated.

$(E \parallel c^*) \parallel (B \parallel c^*)$

The largest component of the magnetoelectric tensor in LiFeSi$_2$O$_6$ is the component α_{33}. Therefore it is a natural consequence that poling of antiferromagnetic domains is possible with magnetic and electric fields both parallel the c^* axis. Polarisation matrices for different temperatures after cooling from 30 K to 12 K in $(E \parallel c^*) = +0.25$ kV/mm and $(B \parallel c^*) = +1$ T are shown in Table 3.8. The matrices were recorded successively while increasing the temperature by 2 K. The achieved polarisation at 12 K is of the same magnitude as for cooling in crossed electric and magnetic fields. All polarisations and their fits are plotted against the temperature in Figure 3.8. The data shown in the figure have been corrected for the background with the data from the matrix at 30 K. The fit values are $m_{y0} = -268(6)$, $m_{z0} = 56(3)$, $N = 240(1)$, $T_{\mathrm{N}} = 18.3(1)$ K, $\beta = 0.42(2)$.

With parallel electric and magnetic field it is also possible to pole opposite antiferromagnetic domains by reversing the magnetic field, see Table 3.9. Reversing the electric field was not tested due to lack of beam time. Again it was possible to pole the antiferromagnetic domains with solely a magnetic field, see Table 3.9. The polarisation is less perfect in this case.
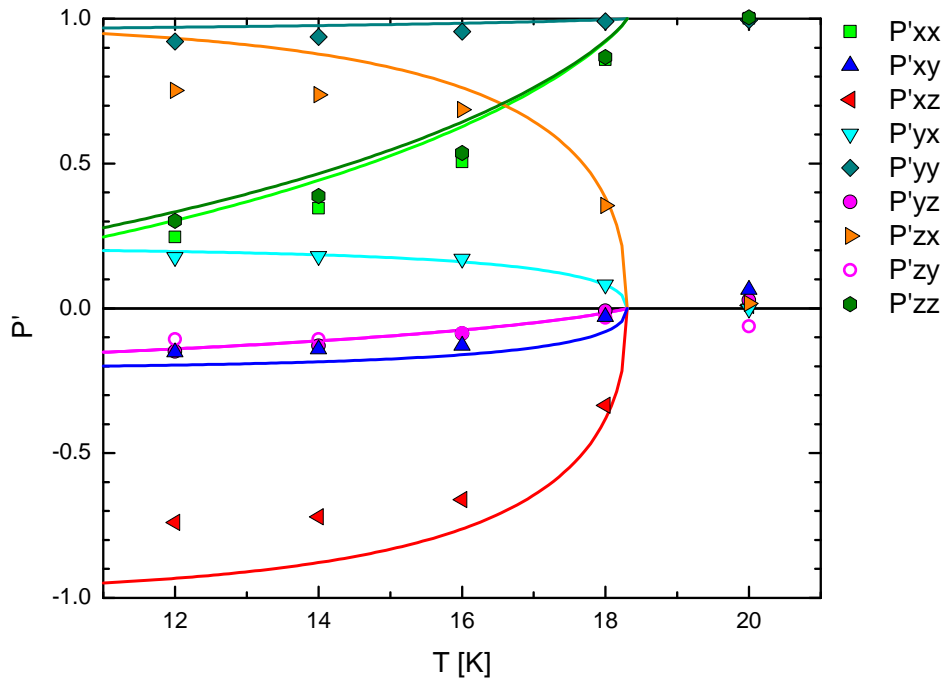

Figure 3.8: Polarisation matrices for different temperatures after field cooling in $(E \parallel c^*) = +0.25$ kV/mm and $(B \parallel c^*) = +1$ T. The temperature was increased during the measurement. The data are from Table 3.8 additionally corrected for background.

$T = 12\,\mathrm{K}$			$T = 14\,\mathrm{K}$			$T = 16\,\mathrm{K}$		
0.203	0.145	0.616	0.276	0.144	0.586	0.396	0.133	0.536
−0.124	0.757	−0.087	−0.112	0.749	−0.085	−0.100	0.747	−0.068
−0.608	−0.123	0.245	−0.576	−0.103	0.309	−0.517	−0.069	0.419
$T = 18\,\mathrm{K}$			$T = 20\,\mathrm{K}$			$T = 30\,\mathrm{K}$		
0.645	0.061	0.266	0.741	−0.001	0.012	0.805	−0.003	0.016
−0.022	0.743	−0.025	0.047	0.736	−0.046	0.040	0.804	−0.025
−0.252	−0.007	0.652	0.007	0.020	0.744	−0.009	0.020	0.808

Table 3.8: Polarisation matrices for different temperatures after field cooling in $(E \parallel c^*) = +0.25\,\mathrm{kV/mm}$ and $(B \parallel c^*) = +1\,\mathrm{T}$.

	$+B$			$-B$		
	0.203	0.145	0.616	0.233	−0.159	−0.617
$+E$	−0.124	0.757	−0.087	0.154	0.748	−0.172
	−0.608	−0.123	0.245	0.630	−0.126	0.252
	0.222	0.031	0.200	0.222	−0.058	−0.201
$E = 0$	−0.031	0.784	−0.131	0.060	0.785	−0.159
	−0.182	−0.125	0.252	0.215	−0.132	0.255

Table 3.9: Neutron polarisation matrices at $(0\,3\,1)$ after field cooling in $(E \parallel c^*) = +0.25\,\mathrm{kV/mm}$ and $(B \parallel c^*) = \pm 1\,\mathrm{T}$ from 30 K to 12 K.

($E \parallel c^*$) $\perp$ ($B \parallel b$)

According to S. Jodlauk [98] the magnetoelectric tensor, Equation (3.1), has only zero-entries for the magnetic field parallel b. Therefore poling of antiferromagnetic domains should not be possible with magnetic fields along b. According to more recent experiments by M. Ackermann [100] there are small components for magnetic field parallel b.

Now it is an interesting result that it is indeed possible to pole antiferromagnetic domains with magnetic field along b. The electric field was along c^* as before. It is even possible to pole the domains with zero electric field. Again this leads to lower values of the neutron polarisation. The data are shown in Table 3.10.

	$+B$			$-B$		
	0.237	−0.116	−0.431	0.218	0.129	0.549
$+E$	0.108	0.787	−0.165	−0.124	0.782	−0.116
	0.440	−0.127	0.268	−0.544	−0.132	0.258
				0.227	0.032	0.187
$E=0$				−0.038	0.788	−0.133
				−0.181	−0.130	0.265

Table 3.10: Neutron polarisation matrices at $(0\,3\,1)$ after field cooling in $(E \parallel c^*) = +0.25\,\text{kV/mm}$ and $(B \parallel b) = \pm 1\,\text{T}$ from $30\,\text{K}$ to $12\,\text{K}$.

($E \parallel c^*$) & ($B = 0$)

Solely electric field without magnetic field is not sufficient to pole antiferromagnetic domains. This was seen before in the right panel of Figure 3.7. After heating into the paramagnetic phase the sample develops no preferred antiferromagnetic domain upon re-entering the magnetic phase. One matrix was recorded with $E = +0.25\,\text{kV/mm}$ and zero magnetic field, Table 3.11. It shows only marginal

	$+E$			$E = 0$		
	0.223	−0.013	−0.006	0.223	−0.009	−0.002
$B=0$	0.013	0.781	−0.146	0.010	0.779	−0.140
	0.013	−0.132	0.252	0.012	−0.131	0.259

Table 3.11: Neutron polarisation matrices at $(0\,3\,1)$ after field cooling in $(E \parallel c^*) = +0.25\,\text{kV/mm}$ and zero magnetic field from $30\,\text{K}$ to $12\,\text{K}$.

polarisation which is of the same size as the polarisation for a sample cooled without any field. Therefore it is not possible to pole antiferromagnetic domains solely with electric fields of $E = +0.25\,\text{kV/mm}$.

3.2.2 Discussion

The experiments at *IN14* and *IN22* demonstrate that it is possible to pole antiferromagnetic domains with electric and magnetic fields applied in different directions both parallel and perpendicularly. One observation is, when reversing one field, the opposite domain is obtained. By reversing both fields the initial domain is re-obtained. This holds for all combinations of field directions. This is in accordance with basic symmetry considerations. Different components of the magnetoelectric tensor were employed for poling the domains. It is most remarkable that the component for $B \parallel b$ brings high polarisation values. This allows two conclusions: either the magnetoelectric tensor is not zero in this component as mentioned by M. Ackermann [100] or the magnetic field had components along c^* . This is quite likely since correct alignment of the magnetic field could not be checked because the crystal was mounted inside the cryostat.

The asymmetry of the direction of the electric field can only be explained by a preferred direction of the sample. This asymmetry is noticeable only for electric fields and not for magnetic fields. The reasons for that might be the following: (I.) The electric polarisation arises from displaced charges. Therefore the electric polarisation is directly coupled to the lattice and may develop a preferred direction. The magnetic moments on the contrary are not directly coupled to the lattice. (II.) The magnetic order is the primary order. Thus a magnetic field has a big influence on the magnetic order and easily overcomes the preferred direction. The ferroelectric order is the secondary order. Therefore an electric field has much less impact on the magnetic order.

It is also not possible to pole antiferromagnetic domains by solely an electric field. Poling with solely a magnetic field was much more obvious for the second sample. In fact for the first sample this effect was not significant. From symmetry considerations neither antiferromagnetic domain is preferred by solely a magnetic field. The fact that poling of antiferromagnetic domains is allowed by solely a magnetic field after all, is a direct consequence of the preferred direction of that sample.

3.3 Toroidal Moment

Poling of antiferromagnetic domains can also be considered in the picture of poling toroidal domains. This section introduces the concept of the toroidal moment and discusses the results of the previous section in the picture of the toroidal moment.

A multiferroic compound is defined by the coexistence of at least two ferroic order parameters [1], in first view one may consider ferroelasticity, ferromagnetism and ferroelectricity. A ferroic order parameter is characterised by the fact that it forms domains which may be switched by applying an external field (stress, magnetic or electric field). These three well-established cases transform differently under the inversion of space and time, $(++, +-, -+)$[3] for ferroelasticity, ferromagnetism, and ferroelectricity, respectively. It is then a natural extension to consider also a ferroic order parameter which breaks both space and time inversion symmetry and transforms as $(--)$. The (ferro-)toroidal moment, which can be defined as the sum over the magnetic moments $\boldsymbol{m}$ multiplied by their position $\boldsymbol{r}$, exhibits the desired transformation behaviour. A toroidal moment can arise either by head-to-tail arrangement of local moments or by orbital currents. Ferrotoroidal order results from spontaneous parallel alignments of the toroidal moments. In order to establish the toroidal moment as an independent fourth ferroic order parameter one needs to further prove the possibility of switching toroidal domains. A combination of crossed (perpendicular) electric and magnetic fields $(\boldsymbol{E} \times \boldsymbol{B})$ fulfils the symmetry requirements and thus should switch the toroidal domains. However, the switching of the toroidal domains has not been reported so far, just the change of the domain structure [38].

Following the definition of C. Ederer and N. Spaldin [36] the toroidal moment $\boldsymbol{t}$ of a bulk material with localised magnetic moments can be computed as sum over all the moments $\boldsymbol{m}_\alpha$ and the cross product with their position vectors $\boldsymbol{r}_\alpha$ with respect to some origin:

$$\boldsymbol{t} = \frac{1}{2} \sum_\alpha \boldsymbol{r}_\alpha \times \boldsymbol{m}_\alpha$$

The choice of that origin it not negligible for the value of the toroidal moment which can be shown easily:

$$\boldsymbol{t}' = \frac{1}{2} \sum_\alpha \boldsymbol{r}'_\alpha \times \boldsymbol{m}_\alpha = \frac{1}{2} \sum_\alpha (\boldsymbol{r}_\alpha + \boldsymbol{R}) \times \boldsymbol{m}_\alpha = \boldsymbol{t} + \frac{1}{2} \boldsymbol{R} \times \boldsymbol{m}$$

where $\boldsymbol{m} = \sum_\alpha \boldsymbol{m}_\alpha$ is the magnetisation. Luckily, in the case of an antiferromagnetic structure the magnetisation $\boldsymbol{m} = 0$ vanishes and the choice of the origin becomes irrelevant. Another crucial detail about the toroidal moment is that it

---

[3]This reads as follows: Ferromagnetism for example stays invariant under the inversion of space but changes sign under the inversion of time.

vanishes for structures with spatial and time inversion symmetry. Spatial inversion affects the position ($\bar{1}: \boldsymbol{r} \to -\boldsymbol{r}, \; \boldsymbol{m} \to \boldsymbol{m}$) and time inversion the magnetic moment ($1': \boldsymbol{r} \to \boldsymbol{r}, \; \boldsymbol{m} \to -\boldsymbol{m}$). Structures with time inversion symmetry obviously do not allow any magnetic order at all so we restrict our treatment to the case of spatial inversion:

$$\boldsymbol{t} = \frac{1}{2} \sum_{\alpha} \boldsymbol{r}_{\alpha} \times \boldsymbol{m}_{\alpha} = \frac{1}{2} \sum_{\alpha} -\boldsymbol{r}_{\alpha} \times \boldsymbol{m}_{\alpha} = -\boldsymbol{t}$$
$$\Rightarrow \boldsymbol{t} = -\boldsymbol{t} = 0$$

For periodic bulk material one likes to restrict the sum to one unit cell. This brings us to the definition of the toroidisation $\boldsymbol{T} = \boldsymbol{t}/V_{\mathrm{S}}$ as the toroidal moment per volume V_{S} of the system. It can be shown (see Reference [36]) that

$$\boldsymbol{T} = \frac{1}{2V} \sum_{j} \boldsymbol{r}_{j} \times \boldsymbol{m}_{j} \tag{3.2}$$

where the sum runs over all moments in the unit cell of volume V. In a periodic system the choice of the basis is ambiguous. Each moment may be translated by a lattice vector $\boldsymbol{R}_{n}$ without changing the overall periodic arrangement. However, such a translation results in a change of the toroidisation.

$$\Delta \boldsymbol{T}_{nj} = \frac{1}{2V} \boldsymbol{R}_{n} \times \boldsymbol{m}_{j}$$

In order to get a well-defined quantity Ederer and Spaldin [36] suggest that only the difference of the toroidisation calculated by equation 3.2 for two states – one being the actual state of interest and the other being a centrosymmetric and thus non-toroidal reference state – is a physical measurable quantity. This difference is independent of the choice of the basis and thus well-defined. In doing so it is not relevant if this structural transition actually takes place in reality or if it is just a mathematical trick.

$$\Delta \boldsymbol{T} = \boldsymbol{T} - \boldsymbol{T}_{\bar{1}} = \frac{1}{2V} \sum_{j} \Delta \boldsymbol{r}_{j} \times \boldsymbol{m}_{j} \tag{3.3}$$

$\Delta \boldsymbol{r}_{j}$ is the structural displacement between the two states.

The magnetic space group of $LiFeSi_2O_6$ is $P2_1/c'$. The magnetic structure is described in detail in Table 3.12 and it is depicted in Figure 3.9. As can be learned from Table 3.12 in the magnetic space group $P2_1/c'$ the inversion centre is in combination with time inversion $\bar{1}'$. This means there is no pure spatial inversion. Thus $P2_1/c'$ allows the toroidal state. While searching for a non-toroidal reference state one comes across the structural phase transition in $LiFeSi_2O_6$ which takes place at $T_{\mathrm{S}} = 229\,\mathrm{K}$ and is characterised by the loss of

3 LiFeSi_2O_6

	Fe site	element	symm. op.	magn. symm.
	1	1	x, y, z	u, v, w
	2	$2_1 \, (0, \tfrac{1}{2}, 0) \; 0, y, \tfrac{1}{4}$	$\bar{x}, y + \tfrac{1}{2}, \bar{z} + \tfrac{1}{2}$	$\bar{u}, v, \bar{w}$
	3	$\bar{1}' \; 0, 0, 0$	$\bar{x}, \bar{y}, \bar{z}$	$\bar{u}, \bar{v}, \bar{w}$
	4	$c' \; x, \tfrac{1}{4}, z$	$x, \bar{y} + \tfrac{1}{2}, z + \tfrac{1}{2}$	$u, \bar{v}, w$
	2	$t' \; (\tfrac{1}{2}, \tfrac{1}{2}, 0)$	$x + \tfrac{1}{2}, y + \tfrac{1}{2}, z$	$\bar{u}, \bar{v}, \bar{w}$
	1	$2' \; \tfrac{1}{4}, y, \tfrac{1}{4}$	$\bar{x} + \tfrac{1}{2}, y, \bar{z} + \tfrac{1}{2}$	$u, \bar{v}, w$
	4	$\bar{1} \; \tfrac{1}{4}, \tfrac{1}{4}, 0$	$\bar{x} + \tfrac{1}{2}, \bar{y} + \tfrac{1}{2}, \bar{z}$	u, v, w
	3	$n \; (\tfrac{1}{2}, 0, \tfrac{1}{2}) \; x, 0, z$	$x + \tfrac{1}{2}, \bar{y}, z + \tfrac{1}{2}$	$\bar{u}, v, \bar{w}$

(Left margin labels: $C'2'/c'$ spanning all rows; $P2_1/c'$ spanning the top four rows.)

Table 3.12: Symmetry elements in the magnetic space groups $P2_1/c'$ and $C'2'/c'$. The magnetic space group is $P2_1/c'$. In the space group $C'2'/c'$ the Fe-site sits at special Wyckoff position $(1/4, y, 1/4)$. The site symmetry is a twofold rotation axis composed with time inversion $2'$ and consequently the magnetic component parallel the b axis (which is labelled with v) must be zero.

the centring: $C2/c \to P2_1/c$. In $C2/c$ the position of the Fe ion is fixed to the special Wyckoff position $(1/4, y, 1/4)$. The site symmetry is a twofold rotation axis 2. When the magnetic structure is assumed to stay invariant under this transition this twofold axis must be composed with time inversion $2'$ and consequently the magnetic component parallel to the b axis (which is labelled with v) must be zero. The complete magnetic space group is $C'2'/c'$. Here C' means the centring operation $\boldsymbol{t}' = (1/2, 1/2, 0)$ is composed with time inversion. More conventionally this would be described by a magnetic propagation vector of either $\boldsymbol{k} = (1, 0, 0)$ or $\boldsymbol{k} = (0, 1, 0)$ but the formalism with the time inversion operator $'$ seems to be more plausible here. There is an additional inversion centre $\bar{1}$ in $C'2'/c'$ which is not composed with time inversion. Thus the toroidal moment must vanish and a suitable reference state is found.

The situation is illustrated in Figure 3.9. In the left part the structure has the symmetry $C'2'/c'$ and an inversion centre $\bar{1}$ (black circle) relates the four iron sites. We choose this inversion centre as origin and the four iron sites as basis. Since two of the moments have parallel magnetic moments and opposite position vectors (green arrows) each, their toroidal contributions cancel out. In the right part of the picture the magnetic symmetry is $P2_1/c'$. Only inversion centres composed with time inversion $\bar{1}'$ (red circle) are left. Due to the reduction of the symmetry structural displacement (green arrows) is allowed. For all iron sites the displacement and the magnetic moments have the same relative phase. Therefore the toroidal moments arising from the shift of the four ions add up.
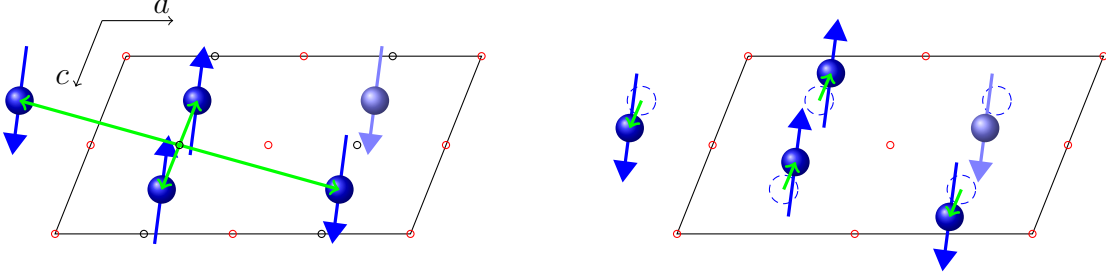
Figure 3.9: The magnetic structure of LiFeSi$_2$O$_6$. (Left) The non-toroidal reference state. The structure has symmetry $C'2'/c'$ and an inversion centre $\bar{1}$ (black circle) relates the four iron sites. We choose this inversion centre as origin and the four iron sites as basis. Since two of the moments have parallel magnetic moments and opposite position vectors (green arrows) each of their toroidal contributions cancel out. Generally, in a centrosymmetric structure $\boldsymbol{t} = 0$. (Right) In reality the magnetic symmetry is $P2_1/c'$. Only inversion centres composed with time inversion $\bar{1}'$ (red circle) are left. Due to the reduction of the symmetry structural displacements (green arrows, enlarged by factor 10) are allowed. For all iron sites the displacement and the magnetic moments have the same relative phase therefore the toroidal moments arising from the shift of the four ions add, $\boldsymbol{t} \neq 0$.

The displacement vector for site 1 is

$$\Delta \boldsymbol{r} = (0.25023, y, 0.23441) - (^1/_4, y, ^1/_4) = (0.00023, 0, -0.01559)$$
$$= (\sigma_x, 0, \sigma_z) = \sigma_x \boldsymbol{a} + \sigma_z \boldsymbol{c}$$

The magnetic moment of site 1 is $\boldsymbol{m} = u\boldsymbol{a}/a + w\boldsymbol{c}/c$ (the component parallel $\boldsymbol{b}$ is ignored on account of the symmetry considerations discussed above). With equation 3.3 we receive for the toroidisation

$$\Delta \boldsymbol{T} = \frac{2}{V}\Delta \boldsymbol{r} \times \boldsymbol{m} = \frac{1}{\pi}\left(\frac{\sigma_z u}{a} - \frac{\sigma_x w}{c}\right)\frac{2\pi \boldsymbol{c} \times \boldsymbol{a}}{V} = \frac{1}{\pi}\left(\frac{\sigma_z u}{a} - \frac{\sigma_x w}{c}\right)\boldsymbol{b}^*$$
$$= -0.00025(3)\frac{\mu_B}{\text{Å}^2}\hat{\boldsymbol{b}}$$

Where $\hat{\boldsymbol{b}}$ is the unit vector in b direction which is parallel to the b^* direction.

By reversing the antiferromagnetic domains the toroidal moment is reversed, too. As demonstrated in the previous section reversing of antiferromagnetic domains is possible by a combination of electric and magnetic fields. The toroidal moment points along the b direction. Therefore the cross product $(\boldsymbol{E} \times \boldsymbol{B})$ should point along b in order to reverse the toroidal moment which implies that $\boldsymbol{E}$ and $\boldsymbol{B}$ should lie in the ac plane. But switching of antiferromagnetic domains is also possible for both fields parallel c. In this case the cross product $(\boldsymbol{E} \times \boldsymbol{B}) = \boldsymbol{0}$ and switching of antiferromagnetic domains cannot be explained by the toroidal moment. Poling of antiferromagnetic domains however can be explained as a natural

consequence of the magnetoelectric effect. In fact the component $\alpha_{33} = 4.86\,\text{ps/m}$ is the largest component of the magnetoelectric tensor. In conclusion, toroidal moments in LiFeSi$_2$O$_6$ can be switched, but this is just a natural consequence of the linear magnetoelectric effect and the toroidal domains are coupled to the antiferromagnetic domains. The two toroidal domains with toroidisation parallel and antiparallel to the b axis result from nearly parallel or nearly antiparallel alignment of magnetic moment and structural displacement, see Figure 3.9. Note that the structural transition only results in 180° domains associated with the sign of the structural order parameter. The same holds for the magnetic transition. Therefore one can identify four different domains with magnetic and structural phases of $(0°, 0°)$, $(0°, 180°)$, $(180°, 0°)$, and $(180°, 180°)$, respectively. From these the first and the last together form the up-toroidisation domain, while the second and the third form the down-toroidisation domain. Toroidal and antiferromagnetic domains are therefore not identical.

3.4 Spin Waves

The magnon dispersion in LiFeSi$_2$O$_6$ was already presented in the diploma thesis [97]. The dispersion relation was revisited in the context of this thesis and a more sophisticated data analysis was performed to describe both branches of the dispersion relation satisfactorily. The magnon dispersion was measured at the triple-axis spectrometer *PANDA* (*FRM II*) at a temperature of 3.5 K in constant-k_f mode with $k_f = 1.55\,\text{Å}^{-1}$. The dispersion relation is shown in Figure 3.10. The dispersion relation is treated in the context of linear spin-wave theory. The Heisenberg Hamiltonian is

$$\hat{H} = -\sum_{i,j,\alpha,\beta} J_{i\alpha,j\beta} \hat{\boldsymbol{S}}_{i\alpha} \cdot \hat{\boldsymbol{S}}_{j\beta} - \sum_{i,\alpha} \sigma_\alpha A_\alpha \hat{S}_{i\alpha}^z$$

See Section 2.5 for further explanation. The following exchange constants are introduced: J_F connecting two Fe sites within the zigzag chains, green lines in
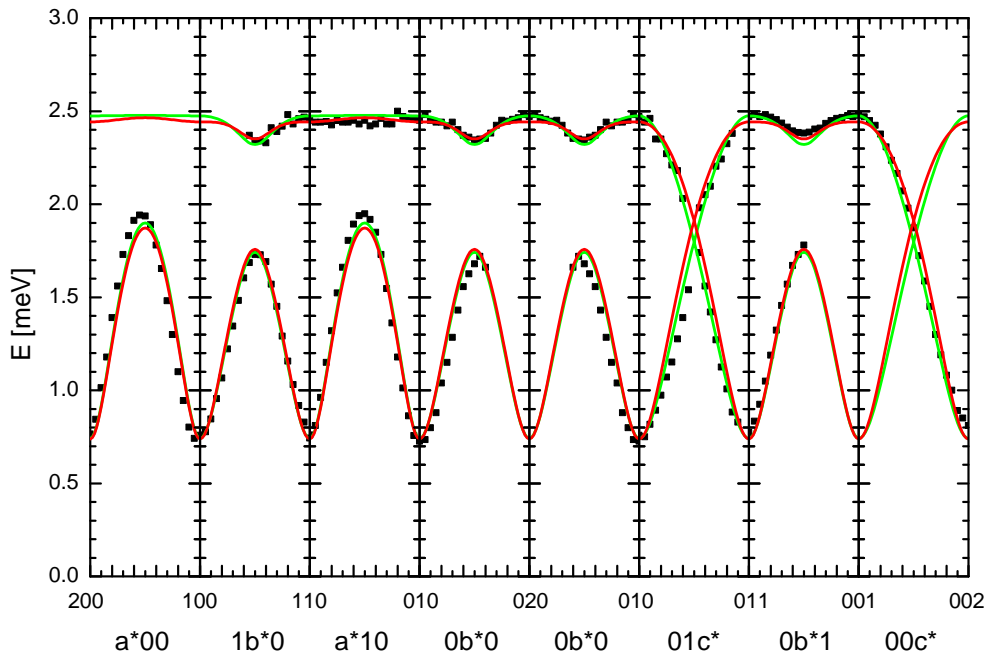
Figure 3.10: Magnon dispersion in LiFeSi$_2$O$_6$ as determined at *PANDA*, $T = 3.5$ K. A Heisenberg model with one ferromagnetic and two antiferromagnetic and an additional anisotropy term describes both branches of the magnon dispersion well (red line). An additional antiferromagnetic next-nearest neighbour interaction along c yields only minor improvement (green line).
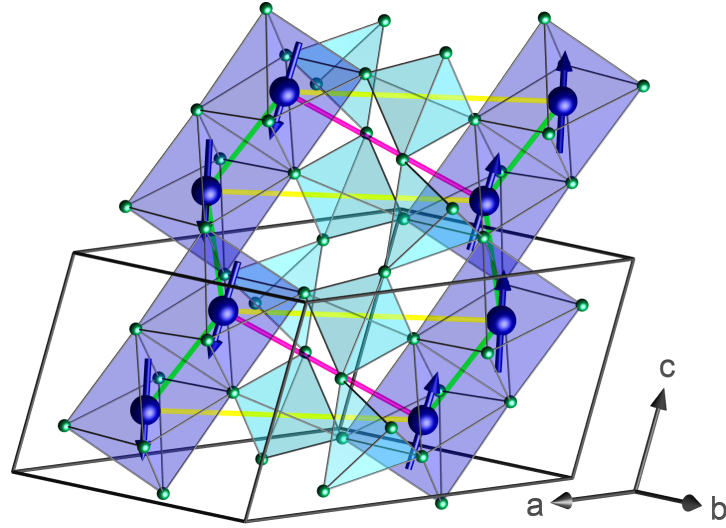
Figure 3.11: Magnetic structure of LiFeSi$_2$O$_6$. Moments are coupled ferromagnetically in the zigzag chains along the c direction and antiferromagnetically between neighbouring chains. The magnon dispersion is described with the following exchange constants: J_F connecting two Fe sites within the zigzag chains, green lines. The super-exchange interactions rise from two equivalent Fe-O-Fe paths. Super-super exchange J_{AF} (yellow) and J_{AF2} (magenta) via one respectively two SiO$_4$ tetrahedra. Each Fe ion has two neighbours with J_F, four neighbours with J_{AF} and two neighbours with J_{AF2}. The anisotropy term A takes into account that the moments are aligned mainly along the c direction.

Figure 3.11. The super-exchange interactions rise from two equivalent Fe-O-Fe paths. Super-super exchange J_{AF} (yellow) and J_{AF2} (magenta) via one respectively two SiO$_4$ tetrahedra [94]. Each Fe ion has two neighbours with J_F, four neighbours with J_{AF} and two neighbours with J_{AF2}. With four Fe sites in the unit cell the matrix $J_{i,\alpha,j,\beta}$ has 32 non-zero entries. The anisotropy term A takes into account that the main part of the magnetic moments is aligned along the c axis.

The solution of the Hamiltonian is given by the eigenvalues of the matrix $\boldsymbol{\sigma} \cdot \boldsymbol{L_q}$, see equations (2.15) and (2.16). The matrix $\boldsymbol{\sigma} \cdot \boldsymbol{L_q}$ and its eigenvalues were computed numerically with a *Python* code. A least square fit was used to fit the four parameters J_F, J_{AF}, J_{AF2} and A to the measured data. As start values the parameters from the analysis of the diploma thesis were used, slightly modified by hand to account for the new parameter J_{AF2}. $S = 5/2$ is fix. The fit yields the following results.

$$
\begin{aligned}
J_{\mathrm{F}} &= 0.0297(8) \quad \mathrm{meV} \\
J_{\mathrm{AF}} &= -0.0513(10) \quad \mathrm{meV} \\
J_{\mathrm{AF2}} &= -0.069(2) \quad\;\; \mathrm{meV} \\
A &= 0.152(6) \quad\;\; \mathrm{meV}
\end{aligned}
$$

The model with theses four parameters describes the magnon dispersion well as can be seen by the red line in Figure 3.10.

The experimental parameters are at odds with theoretical parameters determined by ab initio band structure calculations: $J_{\mathrm{F}} = -0.60\,\mathrm{meV}$, $J_{\mathrm{AF}} = -0.16\,\mathrm{meV}$, $J_{\mathrm{AF2}} = -0.29\,\mathrm{meV}$ [94]. The negative sign indicates that all three exchange interactions are all antiferromagnetic. The labelling was adjusted to be consistent with the labelling introduced in Figure 3.11. The theoretical parameters favour a spiral magnetic structure which is not observed experimentally. Thus the theoretical parameters are not very reliable.

It was tested whether a next-nearest neighbour interaction along c would yield even better results. The improvement of the refinement is marginal. The refinement finds a small antiferromagnetic component J_{AF3}. The other parameters do not change much.

$$
\begin{aligned}
J_{\mathrm{F}} &= 0.0289(6) \quad \mathrm{meV} \\
J_{\mathrm{AF}} &= -0.0467(12) \quad \mathrm{meV} \\
J_{\mathrm{AF2}} &= -0.081(3) \quad\;\; \mathrm{meV} \\
J_{\mathrm{AF3}} &= -0.0082(9) \quad \mathrm{meV} \\
A &= 0.151(4) \quad\;\; \mathrm{meV}
\end{aligned}
$$

The model is displayed as green line in Figure 3.10.

3.5 Spin Density

The spin density was measured at *5C1* the *Laboratoire Léon Brillouin*. The temperature was set to 20 K and a magnetic field of 7 T was applied along the c axis. The flipping ratio of 407 reflections were measured. 160 of these reflections are independent. 380 reflections are equivalent reflections. The (weighted) internal R value is 2.66% (3.37%). The spin density was refined with *FullProf* [102] in the spherical mode [107]. In the spherical mode the magnetic form factor f^{mag} is given by

$$f^{\mathrm{mag}}(s) = \sum_{l=0,2,4,6} W_l \langle j_l(s) \rangle$$

with $s = \sin(\theta)/\lambda$. The radial wave functions of the unpaired electrons are approximated by $\langle j_l(s) \rangle$ whose values are tabulated in [41, 42]. The coefficients W_l are refined. The unit of these coefficients is μ_{B}. W_0 gives the value of the magnetic moment. For Fe^{3+} three coefficients are refineable $l = 0, 2, 4$ and for O^- there is one coefficient $l = 0$. The (weighted) R factor of the refinement is 4.2% (2.3%) and $\chi^2 = 3.6$. The coefficients are listed in Table 3.13. The total magnetic moment is $-1.03(6)\,\mu_{\mathrm{B}}$ which is in perfect agreement with the value at 7 T of the magnetisation curve, Figure 3.13.

The different positions of the O ions are indicated in Figure 3.12. Maps of the spin density are shown in Figures 3.14–3.16.

atom	W_0	W_2	W_4
Fe	$-0.84(2)$	$0.08(17)$	$-0.5(6)$
O1A	$-0.096(15)$		
O1B	$-0.125(15)$		
O2A	$0.069(15)$		
O2B	$0.074(15)$		
O3A	$-0.08(4)$		
O3B	$-0.03(3)$		

Table 3.13: Value of the refinable coefficients W_l. The unit of these coefficients is μ_{B}. W_0 gives the value of the magnetic moment.
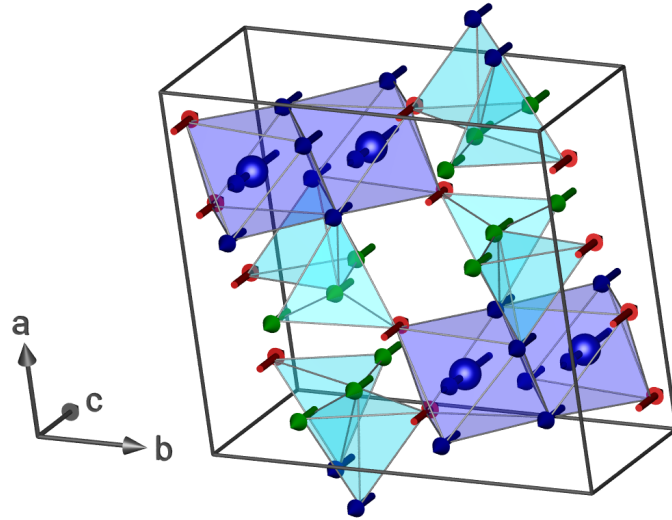
Figure 3.12: This figure indicates the different positions of the magnetic moments. The O1 ions (blue) are located at the corners of the edge-sharing FeO_6 octahedra that belong to two octahedra. The O2 ions (red) are located at the corners of the octahedra which have no contact to other octahedra. The O3 ions (green) are not in contact to the octahedra. They are located in the corners of the corner-sharing SiO_4 tetrahedra. The Fe ions (blue) and their moments (blue) are located in the centres of the octahedra. Moments are not true to scale.
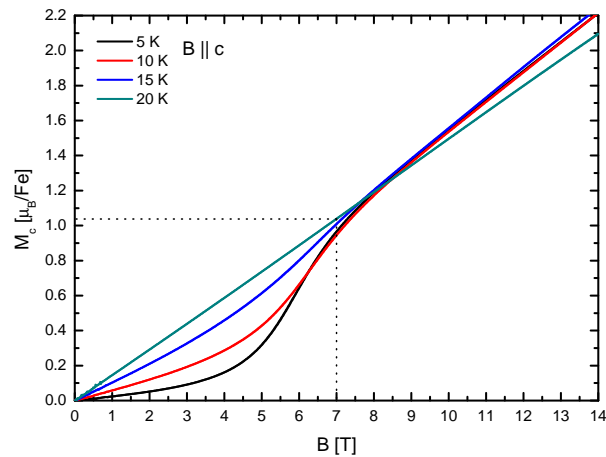
Figure 3.13: Magnetisation curve of $LiFeSi_2O_6$ [98].
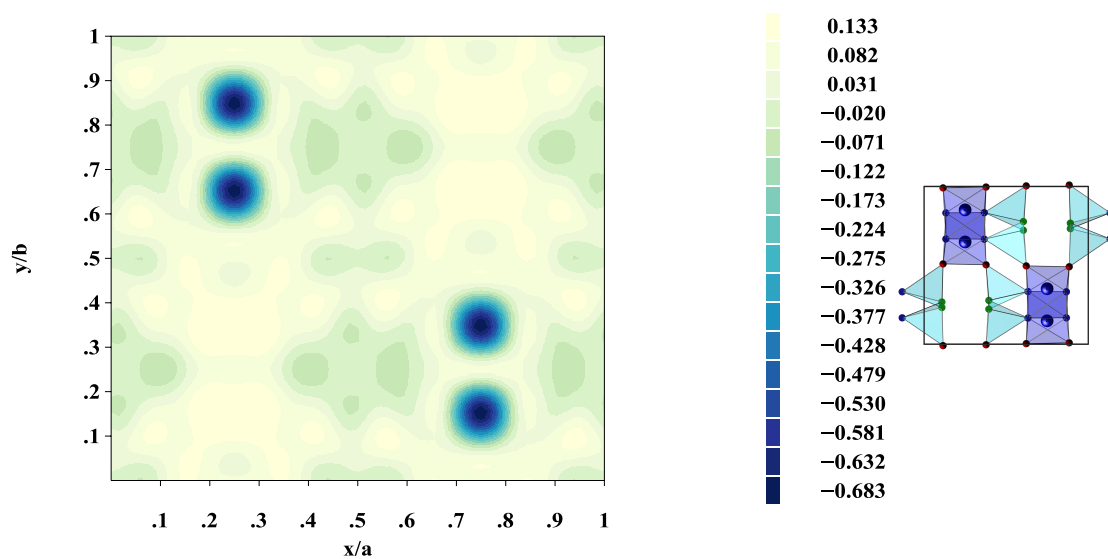
Figure 3.14: Spin density of LiFeSi$_2$O$_6$ in the *ab* plane integrated over the whole unit cell.
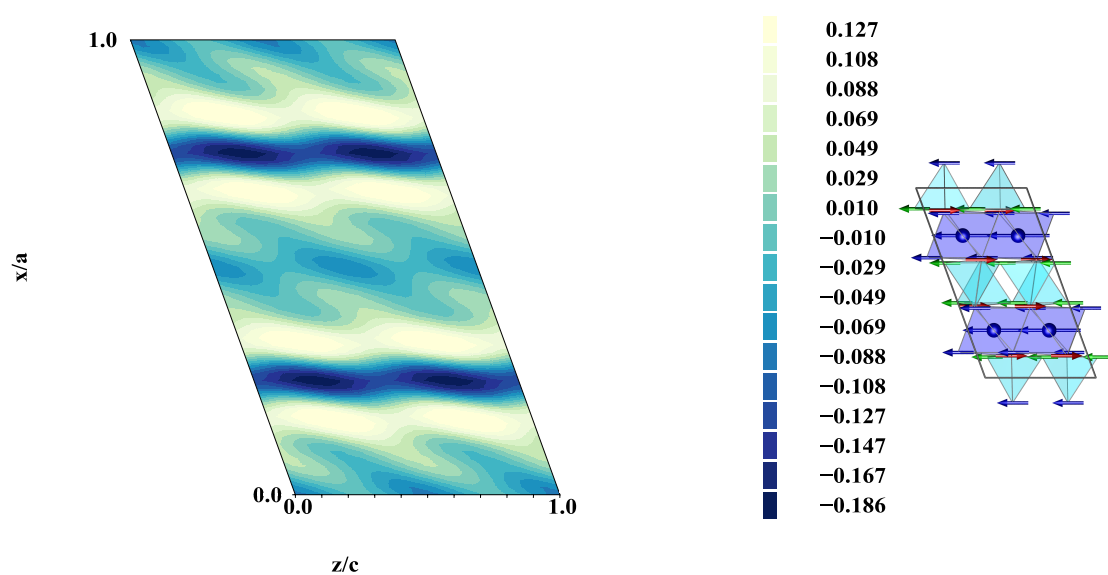
Figure 3.15: Spin density of LiFeSi$_2$O$_6$ in the *ac* plane integrated over the whole unit cell.
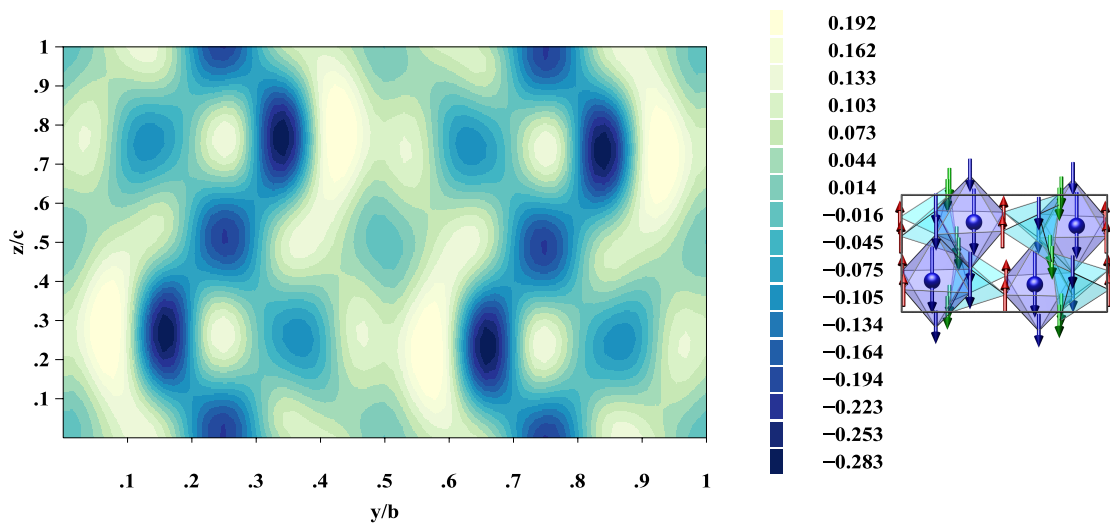
Figure 3.16: Spin density of LiFeSi$_2$O$_6$ in the bc plane integrated over the whole unit cell.

3.6 Conclusion

This chapter presented different neutron investigations of magnetoelectric LiFeSi$_2$O$_6$. The magnetic structure was investigated by single-crystal neutron diffraction. LiFeSi$_2$O$_6$ exhibits a single magnetic phase transition below 18 K. The magnetic structure is a canted antiferromagnet with moments in the *ac* plane plus additional components along *b*. The main moment is along *c*. The magnetic space group is $P2_1/c'$ which is in accordance with the magnetoelectric tensor as it was determined primarily.

The magnetoelectric effect provides evidence that it should be possible to manipulate antiferromagnetic domains in LiFeSi$_2$O$_6$. Spherical neutron-polarisation analysis was employed to investigate whether the combination of an electric and a magnetic field allows to pole antiferromagnetic domains. Indeed, it was possible to pole antiferromagnetic domains by the use of different combinations of perpendicular or parallel electric and magnetic fields employing different components of the magnetoelectric tensor. Even the components α_{i2}, which were stated to be zero, can be used for poling of antiferromagnetic domains effectively. This leads to two possible explanations: either the alignment of the magnetic field was not accurate or the components α_{i2} are not completely zero. The latter is confirmed by new measurements of the magnetoelectric tensor. In the magnetic space group the inversion centre is composed with time inversion. Therefore a toroidal moment is possible in LiFeSi$_2$O$_6$. The toroidal moment is coupled to the antiferromagnetic domains. Thus it is also possible to pole toroidal domains. However, a special contribution of the toroidal moment to the properties of LiFeSi$_2$O$_6$ cannot be asserted.

In addition, the magnon dispersion and the spin density were determined. The magnon dispersion is described very satisfactorily by a model employing three exchange integrals and one anisotropy term.

4 NaFeSi$_2$O$_6$

Aegirine (NaFeSi$_2$O$_6$) belongs to the pyroxenes with the general composition $A M$Si$_2$O$_6$ (A = mono- or divalent metal, M = di- or trivalent metal). It crystallises in the monoclinic space group $C2/c$ [108] with lattice constants $a = 9.6618(5)$ Å, $b = 8.7933(4)$ Å, $c = 5.2946(2)$ Å, $\beta = 107.334(3)°$ at 1.9 K, data from Table 4.8. The crystal structure is similar to the structure of LiFeSi$_2$O$_6$. Natural aegirine was discovered to be multiferroic by S. Jodlauk et al. at Universität zu Köln a few years ago, published 2007 [94]. Antiferromagnetic order sets in at 8 K and an anomaly at 6 K can be observed in the susceptibility data as well as in the magnetic intensity (Figure 4.2). This anomaly is accompanied by the development of spontaneous electric polarisation along the monoclinic b direction, $P_b \approx 13\,\mu$C/m^2. The electric polarisation can be suppressed by a magnetic field of about 4 T in the ac plane and a smaller polarisation along the c direction appears instead, $P_c \approx 1\,\mu$C/m^2 [94].

Understanding the mechanism of multiferroic coupling in aegirine requires knowing the magnetic structure. Several investigations of the magnetic structure in aegirine based on neutron scattering have been published so far [109–111]. However, these three publications are contradictory and neither of them allows on a basis of a clear picture of the magnetic structure to explain the origin of the spontaneous electric polarisation. The reason for that is, that the quantitative measurements in these three works are based on neutron *powder* measurements
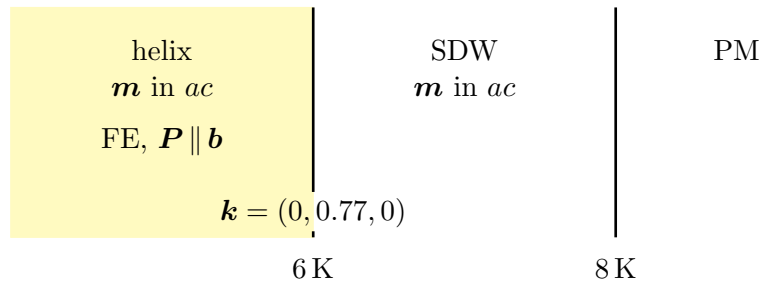

Figure 4.1: Magnetic phase diagram of NaFeSi$_2$O$_6$. At 8 K the magnetic structure sets in as a transverse spin-density wave with moments in the ac plane and at 6 K evolves into an elliptical helix with moments remaining in the ac plane. The transition in the spiral phase is accompanied by the onset of spontaneous electric polarisation.

on *synthetic* samples. Mere on basis of a powder measurement it is often not possible to unambiguously distinguish between *different* models of complex magnetic structures which nevertheless have a *similar* magnetic structure factor.

The advantage of the results in this thesis is, that they can rely on a series of single crystal and powder neutron measurements, and, that the natural samples were cut from the same large crystal which was found to be multiferroic by Jodlauk et al. [94]. The measurements include measurements with polarised neutrons on a single crystal at *IN14*, collecting several hundreds of integrated intensities on a single crystal at *D10*, a powder measurement with natural and synthetic powder at *G4.1*, and a single crystal measurement at high pressure at *4F2*.

Unlike in the three publications [109–111] the measurements at natural samples show no commensurate magnetic order but only incommensurate order with propagation vector $\boldsymbol{k} = (0, 0.77, 0)$. Combining all measurements the following picture of the magnetic structure in natural NaFeSi$_2$O$_6$ can be derived: the magnetic structure forms a transverse spin-density wave with moments in the *ac* plane in the temperature range between 8 K and 6 K and evolves towards an elliptical helix with moments in the *ac* plane below 6 K.

In a powder measurement with synthetic powder additional commensurate magnetic order with propagation vector $\boldsymbol{k} = (0, 1, 0)$, as observed before in the three publications, can be confirmed. By applying relatively low pressure up to 5 kbar on a natural sample surprisingly it was possible to suppress the incommensurate magnetic structure and regain the commensurate order.

4.1 Samples

All samples of natural NaFeSi$_2$O$_6$ were cut from the same high quality natural single crystal found on Mount Malosa, Malawi, which was also used by S. Jodlauk et al. [94]. The chemical composition was reported to be Na$_{1.04}$Fe$_{0.83}$Ca$_{0.04}$Mn$_{0.02}$Al$_{0.01}$Ti$_{0.08}$Si$_2$O$_6$. The samples were provided by the group of L. Bohatý of the Insitut für Kristallographie at Universität zu Köln.

The magnetic propagation vector of different samples of natural NaFeSi$_2$O$_6$ varies between $(0, 0.77, 0)$ to $(0, 0.79, 0)$. The magnetic structure is highly frustrated and reacts sensitively on external parameters as the exact composition of the sample. As the samples were cut from one large single crystal it is very likely that the exact composition varies slightly throughout this crystal of several cm length. The strong influence of external parameters on the propagation vector can also be observed when pressure is applied to the sample: the propagation vector shifts to higher values for increasing pressure, compare Figure 4.5. A temperature dependence of the propagation vector is however marginal, compare Table 4.8 and 4.11.

The synthetic sample shows, in addition, magnetic reflections which can be in-

dexed with a commensurate propagation vector $(0, 1, 0)$. Powder of $NaFeSi_2O_6$ was synthesised by crystallisation of a glass of stoichiometric composition ($NaFeSi_2O_6$) at $800\,°C$ by P. Becker of the Insitut für Kristallographie at Universität zu Köln.

4.2 Symmetry Analysis

In order to solve a complex magnetic structure a detailed symmetry analysis is indispensable. This section deals with the symmetry analysis.

All symmetry elements of a space group G can be written in the Koster-Seitz notation $g = \{\boldsymbol{\alpha}|\boldsymbol{\tau_\alpha} + \boldsymbol{R_n}\}$, where $\boldsymbol{\alpha}$ is an orthogonal 3×3 matrix symbolising the rotational part [proper: $\det \boldsymbol{\alpha} = 1$ (real rotation), improper: $\det \boldsymbol{\alpha} = -1$ (inversion, refection)] of the symmetry and $\boldsymbol{\tau_\alpha} + \boldsymbol{R_n}$ its translational part. $\boldsymbol{\tau_\alpha}$ is either null or a translation vector with fractional components, $\boldsymbol{R_n}$ is a lattice translation vector with integer components.

The action of g on the space variable $\boldsymbol{r}$ is given by $g(\boldsymbol{r}) = \boldsymbol{\alpha} \cdot \boldsymbol{r} + \boldsymbol{\tau_\alpha} + \boldsymbol{R_n}$. The action of g on a vectorial quantity is solely determined by its rotational part. A translation transports a vectorial magnitude from one position to another leaving the orientation invariant. When the vector is polar (e.g. the electric dipole moment) it transforms as $g(\boldsymbol{p}) = \boldsymbol{\alpha} \cdot \boldsymbol{p}$. When the vector is axial (e.g. the magnetic dipole moment) it transforms as $g(\boldsymbol{a}) = \det(\boldsymbol{\alpha})\, \boldsymbol{\alpha} \cdot \boldsymbol{a}$.

If the magnetic structure has a non zero propagation vector $\boldsymbol{k}$ it may be that not all symmetry elements of the space group G are compatible with this modulation. In this case the little group $G_{\boldsymbol{k}}$ (all elements of G which are compatible with $\boldsymbol{k}$) may be a proper subgroup of G. The condition for compatibility of a symmetry element g with the propagation vector $\boldsymbol{k}$ is, that it leaves the propagation vector invariant modulo a reciprocal lattice vector $\boldsymbol{G}$

$$\boldsymbol{\alpha} \cdot \boldsymbol{k} = \boldsymbol{k} + \boldsymbol{G}$$

[112, 113].

The crystallographic space group of $NaFeSi_2O_6$ is $C2/c$. The symmetry elements of this space group are listed in Table 4.1. The magnetic moments are located at the Fe sites which have the special Wyckoff position $(0, y, 1/4)$; the site symmetry is a twofold rotation axis. So the eight symmetry elements generate only four Fe sites; two of them being generated by the C centring and thus their magnetic moment is determined by the magnetic moment of the site to which they are related by the centring operation multiplied by the phase factor of $e^{-i\boldsymbol{k} \cdot \boldsymbol{t}}$.

The magnetic propagation vector found in the used natural crystal is $\boldsymbol{k} = (0, 0.77, 0)$. The little group is $G_{\boldsymbol{k}} = \{1, 2, t, 2_1\}$, which is $C2$. In the space group describing the nuclear structure the four Fe sites belong to one orbit (i.e. they are connected by the symmetry operations). The little group contains less symmetry elements, that is why the orbit splits in two orbits. So, with respect to the little

element	symm. op.
1	x, y, z
2 $0, y, \frac{1}{4}$	$\bar{x}, y, \bar{z} + \frac{1}{2}$
$\bar{1}$ $0, 0, 0$	$\bar{x}, \bar{y}, \bar{z}$
c $x, 0, z$	$x, \bar{y}, z + \frac{1}{2}$
t $(\frac{1}{2}, \frac{1}{2}, 0)$	$x + \frac{1}{2}, y + \frac{1}{2}, z$
2_1 $(0, \frac{1}{2}, 0)$ $\frac{1}{4}, y, \frac{1}{4}$	$\bar{x} + \frac{1}{2}, y + \frac{1}{2}, \bar{z} + \frac{1}{2}$
$\bar{1}$ $\frac{1}{4}, \frac{1}{4}, 0$	$\bar{x} + \frac{1}{2}, \bar{y} + \frac{1}{2}, \bar{z}$
n $(\frac{1}{2}, 0, \frac{1}{2})$ $x, \frac{1}{4}, z$	$x + \frac{1}{2}, \bar{y} + \frac{1}{2}, z + \frac{1}{2}$

Table 4.1: Symmetry elements of the space group $C2/c$.

group the two Fe sites which are not related by the C centring (symmetry element t), now are independent. The independent Fe ions are located at (x, y, z) and at $(\bar{x}, \bar{y}, \bar{z})$. The character table is listed in Table 4.2. There are two irreducible representations Γ_1 and Γ_2. The symmetry restrictions for the magnetic moments are given in Table 4.3.

The reflection $(0, 0.77, 0)$ exists, therefore the valid irreducible representation cannot be Γ_1. In Γ_1 the magnetic moment is parallel $\boldsymbol{b}$ and for the reflection $(0, 0.77, 0)$ the scattering vector $\boldsymbol{Q}$ is parallel to the magnetic moment and according to Equation 2.3 the intensity is null. A combination of both irreducible representations is possible allowing magnetic symmetries of the form (u, v, w).

The synthetic sample shows additional magnetic reflections which can be indexed with a propagation vector $\boldsymbol{k} = (0, 1, 0)$ which is equivalent to $\boldsymbol{k} = (1, 0, 0)$.[1] For this propagation vector the little group is identical to the space group, i.e. all symmetry operations are compatible with the propagation vector and the orbit of all atom sites is *not* split into two orbits as it was the case for the incommensurate propagation vector. The character table is given in Table 4.4 and the corresponding symmetry conditions for the magnetic moments are given in Table 4.5. With a propagation vector $\boldsymbol{k} = (0, 1, 0)$ only simple antiferromagnetic spin arrangements (up-down-up-down) are possible (the phase between nearest moments connected by the propagation vector is $\phi_{\boldsymbol{k}} = \boldsymbol{k} \cdot \boldsymbol{t} = \pi$). The symmetry analysis was done with *BasIreps* [102].

---

[1] Two propagation vectors $\boldsymbol{k}_1$ and $\boldsymbol{k}_2$ are equivalent if $\boldsymbol{k}_1 - \boldsymbol{k}_2$ is a vector of the reciprocal lattice.

		1	2
Γ_1	$C2$	1	1
Γ_2	$C2'$	1	-1

Table 4.2: Character table of the little group $G_{\boldsymbol{k}} = C2$. $\boldsymbol{k} = (0, 0.77, 0)$.

	x, y, z
Γ_1	$0, v, 0$
Γ_2	$u, 0, w$

Table 4.3: Symmetry conditions of the two irreducible representations of $C2$. $\boldsymbol{k} = (0, 0.77, 0)$.

		1	2	$\bar{1}$	c
Γ_1	$C2/c$	1	1	1	1
Γ_2	$C2/c'$	1	1	-1	-1
Γ_3	$C2'/c'$	1	-1	1	-1
Γ_4	$C2'/c$	1	-1	-1	1

Table 4.4: Character table of $C2/c$. $\boldsymbol{k} = (0, 1, 0)$.

	x, y, z	$\bar{x}, \bar{y}, \bar{z}$
Γ_1	$0, v, 0$	$0, v, 0$
Γ_2	$0, v, 0$	$0, \bar{v}, 0$
Γ_3	$u, 0, w$	$u, 0, w$
Γ_4	$u, 0, w$	$\bar{u}, 0, \bar{w}$

Table 4.5: Symmetry conditions of the four irreducible representations of $C2/c$. $\boldsymbol{k} = (0, 1, 0)$.

4.3 Spherical Polarisation Analysis at IN14

The triple-axis spectrometer *IN14* at the *Institut Laue-Langevin* (*ILL*) was used to investigate the magnetic structure of natural $NaFeSi_2O_6$ with *CRYOPAD* for spherical polarisation analysis. The flipping ratio at $(3\,3\,0)$ $(1000\,\text{cnts/s})$ was 18. A single crystal sample of natural aegirine was mounted in the $(1\,0\,0)/(0\,1\,0)$ scattering plane. The propagation vector of this sample is $(0, 0.79, 0)$. An electric field of $0.7\,\text{kV/mm}$ was applied parallel to the b direction during the cooling process in order to produce a monodomain state.

Figure 4.2 shows two temperature dependent scans at the magnetic reflections $(0, -1.21, 0)$ and $(3, 0.21, 0)$. With the formulas given in Table 2.1 we can gain some qualitative information on the magnetic structure in $NaFeSi_2O_6$. The data were treated to directly display the different magnetic contributions: $|\boldsymbol{M}_\perp|^2 = |M_y|^2 + |M_z|^2$ and $M_\chi^2 = -i(\boldsymbol{M}_\perp \times \boldsymbol{M}_\perp^*)_x = 2\Im(M_y M_z^*)$. The crystal is mounted with its crystallographic c axis being vertical, i.e. $c \parallel z$. For the scan at $\boldsymbol{Q} = (0, -1.21, 0)$ we get $x \parallel b$ and $y \parallel a^*$ (approximately $y \parallel a$) and thus $M_z = M_c$ and $M_y = M_a$. So, the intensity must arise from a magnetic moment distribution which has components in the ac plane. Further the emergence of M_χ^2 at $6\,\text{K}$ indicates the development of a chiral magnetic structure below that temperature. The maximum chiral ratio is $r_\chi = 0.3$.

Repeating the same analysis for the reflection $\boldsymbol{Q} = (3, 0.21, 0)$ we get $x \parallel a^*$ (approximately) and $y \parallel b$ (approximately) and thus $M_z = M_c$ and $M_y = M_b$. In

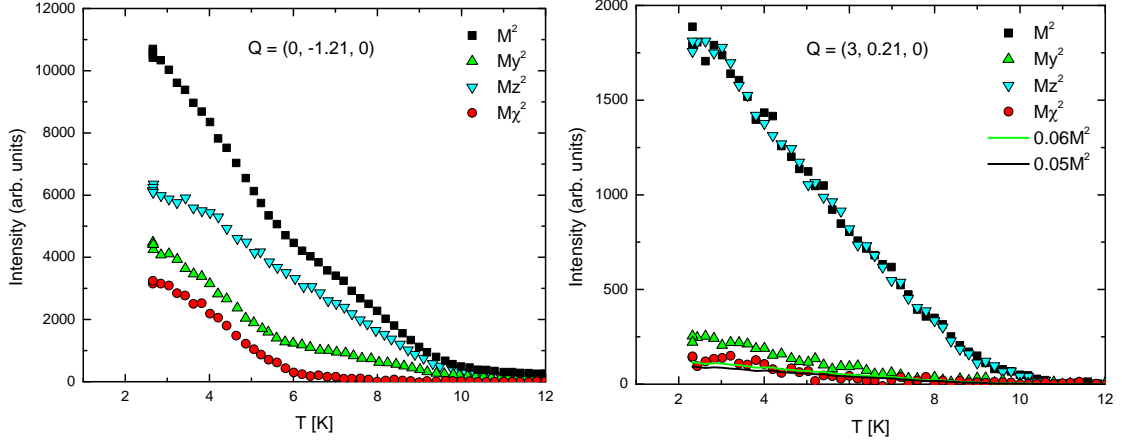**Figure 4.2:** Spherical polarisation analysis of magnetic intensities in NaFeSi$_2$O$_6$ recorded at *IN14*. The data is treated to directly display the different magnetic contributions. For $\boldsymbol{Q} = (0, -1.21, 0)$ we get $M_z = M_c$ and $M_y = M_{a^*}$. For $\boldsymbol{Q} = (3, 0.21, 0)$ we get $M_z = M_c$ and $M_y \approx M_b$. These scans suggest the following model for the magnetic structure: The b component is null and the moments lie within the ac plane to form a transverse spin-density wave in the temperature range between $10\,\mathrm{K}$ and $6\,\mathrm{K}$ and a helical spiral in the range below $6\,\mathrm{K}$. The misalignment of the scattering vector $\boldsymbol{Q}$ and the a^* axis can account for the small chiral contribution (black line). The flipping ratio can account for half of the $|M_y|^2$ component (green line).

particular the fact that there is almost no intensity for M_y might indicate that there is little or no moment parallel b.

In the following it will be analysed whether a helix in the ac plane can account for the small intensities $|M_y|^2$ and M_χ^2 at $\boldsymbol{Q} = (3, 0.21, 0)$. The effect of the flipping ratio and the small misalignment between the scattering vector $\boldsymbol{Q}$ and the a^* axis will be analysed.

The contribution of $|M_y|^2$ can be measured in the non-spin-flip channels (NSF) of I_y and in the spin-flip channels (SF) of I_z: $|M_y|^2 = I_y^{\mathrm{NSF}} = I_z^{\mathrm{SF}}$. Likewise: $|M_z|^2 = I_z^{\mathrm{SF}} = I_z^{\mathrm{NSF}}$. Even if we expect zero intensity for $|M_y|^2 = 0$ a flipping ratio of FR = 18 generates an intensity of $|M_y|^2 = \frac{1}{\mathrm{FR}}|M_z|^2 = \frac{1}{\mathrm{FR}}|\boldsymbol{M}_\perp|^2 = 0.056|\boldsymbol{M}_\perp|^2$.

If the scattering vector lies within the rotation plane of the helix, the chiral term is zero $M_\chi^2 = 0$, compare footnote on page 23. If we assume a circular helix in the ac plane, there is a small angle α between the scattering vector $\boldsymbol{Q}$ and the rotation plane of the helix. The component M_y is then no longer zero but $M_y = qM$ where $q = \sin(\alpha)$ and the helix is described by $M_{a^*} = M$ and $M_c = \mathrm{i}M$. The c axis is vertical and thus $M_z = \mathrm{i}M$ is not affected by the misalignment. The effect of the misalignment on $|\boldsymbol{M}_\perp|^2$ and $|M_y|^2$ is almost negligible because it contributes quadratically. For M_χ^2 it is not negligible because it contributes linearly.

$$\begin{aligned}
|\boldsymbol{M}_\perp|^2 &= |M_y|^2 + |M_z|^2 = (1 + q^2)|M|^2 \\
|M_\chi|^2 &= |2\Im(M_y M_z^*)| = 2q|M|^2 \\
&\Rightarrow |r_\chi| = \frac{2q}{1 + q^2}
\end{aligned}$$

With $\alpha = 4.4°$ it follows $|M_y|^2 = 0.0059|M|^2$ and $|M_\chi|^2 = 0.15|M|^2$. Considering the correction for the flipping ratio, too, we get for the y component: $|M_y|^2 = 0.0059|M|^2 + 0.056|M|^2 = 0.06|M|^2$. For the chiral contribution we must consider that the experimental chiral ratio was $r_\chi = 0.3$. Therefore the expected chiral term due to the misalignment amounts to $|M_\chi|^2 = 0.05|M|^2$. Both corrections terms are depicted in the right panel of Figure 4.2. The chiral term can be explained by the misalignment completely. The contribution of $|M_y|^2$ can only be explained to a factor 1/2. Another disagreement is that $|M_y|^2 + |M_z|^2$ do not add up to $|\boldsymbol{M}_\perp|^2$. Therefore it might be argued that the b component of the magnetic structure is actually zero and the flipping ratio was less than assumed or some other effect has to be considered.

Based on these qualitative results and the symmetry analysis the following model for the magnetic structure is proposed: The magnetic moments lie within the ac plane. The emergence of the chiral term M_χ^2 further suggests a helical spin-spiral structure below $6\,\mathrm{K}$ and a transverse spin-density wave above. The existence of a small b component cannot be excluded. However, its contribution is not chiral.

Attempts in reversing the sign of the chiral magnetic term M_χ^2 by means of an electric field along the crystallographic b direction did not succeed. Furthermore it can be assumed that the crystal is not in a mono-domain state. For a mono-domain state of a circular helix one would compute the chiral term to be of as high intensity as the total magnetic intensity $|\boldsymbol{M}_\perp|^2$. The chiral term being so much smaller indicates that the crystal consists of two domains – unequal in size – which generate chiral terms with opposite signs which cancel out most of the chiral contribution.

4.4 Single-Crystal Measurement at D10

The magnetic structure of a second single crystal sample of natural NaFeSi$_2$O$_6$ was investigated at *D10* (*ILL*) single-crystal diffractometer using a wavelength of $\lambda = 2.36$ Å and an $80{\times}80$ mm^2 two-dimensional microstrip detector for three-dimensional resolution in reciprocal space [114]. Structural and magnetic peaks were recorded at two temperatures (1.8 K and 6.9 K). The lower temperature lies in the multiferroic phase below 6 K, the higher temperature lies in the antiferromagnetic but paraelectric phase. The propagation vector of this sample is $\boldsymbol{k} = (0, 0.78, 0)$.

The refinement was done in the space group $C2/c$ with the lattice constants at 1.9 K from a powder sample, see Table 4.8: $a = 9.6618(5)$ Å, $b = 8.7933(4)$ Å, $c = 5.2946(2)$ Å, $\beta = 107.334(3)°$. The refinement was done with *FullProf* [102].

4.4.1 Crystal Structure

At 1.8 K 1027 reflections were collected out of which 340 arouse from the crystal structure while the remaining 687 were reflections from the magnetic structure. 240 of the structural reflections were equivalent reflections. 113 valid independent reflections were used for the refinement of the crystal structure. The (weighted) internal R-value was 2.8 % (3.3 %).

At 6.9 K 852 reflections were collected of which 366 were structural ones. 255 of those were equivalent reflections. 113 valid independent reflections were used for the refinement. The (weighted) internal R-value was 2.5 % (3.6 %).

atom	x	y	z	U_{iso} [Å^2]			
Na	0	0.3002(11)	1/4	0.010(3)	T	$=$	1.8 K
Fe	0	0.8994(4)	1/4	0.0159(17)			
Si	0.2905(6)	0.0903(6)	0.2379(9)	0.0047(18)	R_{F^2}	$=$	5.9 %
O1	0.1137(5)	0.0796(4)	0.1384(7)	0.0078(16)	R_{wF^2}	$=$	5.9 %
O2	0.3595(4)	0.2551(5)	0.3041(7)	0.0101(16)	R_F	$=$	3.8 %
O3	0.3526(4)	0.0089(5)	0.0105(6)	0.0115(14)	$\chi^2(I)$	$=$	13.5
Na	0	0.3000(10)	1/4	0.008(3)	T	$=$	6.9 K
Fe	0	0.8994(4)	1/4	0.0146(16)			
Si	0.2902(5)	0.0901(5)	0.2379(9)	0.0041(18)	R_{F^2}	$=$	5.8 %
O1	0.1132(4)	0.0795(4)	0.1387(7)	0.0060(16)	R_{wF^2}	$=$	5.8 %
O2	0.3597(4)	0.2554(5)	0.3039(7)	0.0096(16)	R_F	$=$	3.7 %
O3	0.3526(4)	0.0088(4)	0.0108(6)	0.0114(14)	$\chi^2(I)$	$=$	13.8

Table 4.6: Structural parameters of natural NaFeSi$_2$O$_6$ as determined at *D10*.

The refinement was done with isotropic temperature factors and anisotropic extinction correction (model 4 in *FullProf*). The results are listed in Table 4.6. There is no significant difference between the crystal structures at $1.8\,\mathrm{K}$ and $6.9\,\mathrm{K}$.

4.4.2 Magnetic Structure

At $1.8\,\mathrm{K}$ 687 magnetic reflections were recorded. After averaging 423 independent reflections were used for the refinement.

Different models were implemented and fitted to the data with *FullProf*. In all models the two Fe sites which belong to the two different orbits were described by identical Fourier coefficients, only the phase $\phi_{\boldsymbol{k}}$ between those two moments was chosen variable. This condition is necessary, otherwise the absolute moment can be split arbitrarily among both sites and convergence of the refinement cannot be reached. This constraint, however, is not too strong as both sites still have the same site symmetry and thus should have similar magnetic moments. The phase between the moments which are related by the C centring is given by $\phi_{\boldsymbol{k}} = \boldsymbol{k} \cdot \boldsymbol{t} = 2\pi \cdot 0.39$.

A helical magnetic structure with moments in the ac plane is compatible with the irreducible representation Γ_2. An elliptical helix with moments in the ac plane was fitted to the data and, for comparison, elliptical cycloidal spirals with moments in the ab and the bc plane, respectively, were fitted to the data. Of these three models only the ac helix is an eligible candidate as can be learned from the R values of the three models listed in Table 4.7. It was also tested whether an additional b component to an ac helix would lead to better results; the improvement is however almost negligible and the value of the b component is small. Again, for comparison sinusoidal spin-density waves (SDW) in different planes were refined.

	cycl. ab	cycl. bc	hel. ac	hel. $ac + b$
R_{F^2}	38.2%	35.3%	17.7%	17.4%
R_{wF^2}	41.7%	41.5%	19.9%	19.8%
R_F	22.3%	20.9%	12.1%	12.1%
$\chi^2(I)$	95.3	94.0	21.7	21.5
	SDW ab	SDW bc	SDW ac	SDW abc
R_{F^2}	39.1%	37.1%	30.8%	30.7%
R_{wF^2}	43.2%	45.4%	35.4%	35.3%
R_F	24.6%	23.8%	20.9%	20.2%
$\chi^2(I)$	101.6	112.2	68.2	68.1

Table 4.7: R values of different magnetic models of natural $\mathrm{NaFeSi_2O_6}$ fitted to the data determined at *D10* at $1.8\,\mathrm{K}$.
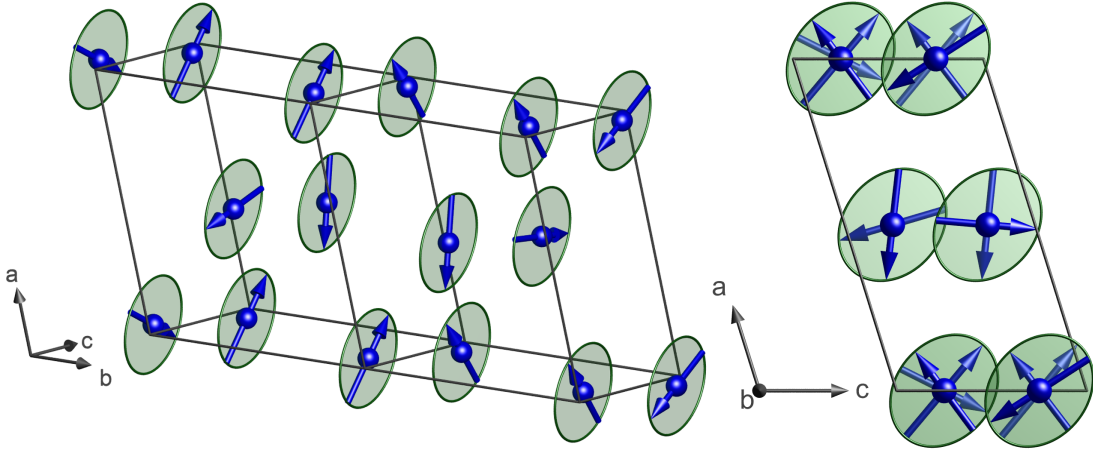
Figure 4.3: Low temperature magnetic structure of natural NaFeSi$_2$O$_6$ at 1.8 K as determined at *D10*. Here the elliptical helix with moments in the *ac* plane is pictured.

SDW's do not yield good results and thus can be excluded.

Based on these refinements the following model for the magnetic structure can be proposed: The low temperature magnetic structure ($T = 1.8$ K) of the natural crystal of aegirine forms an elliptical helix with moments in the *ac* plane, the existence of a small component along *b* cannot be excluded although it is not necessary to successfully describe the data. The lengths of the major and the minor principle axis of the basal ellipse of the helix are $M_{\mathrm{max}} = 3.06(3)\,\mu_{\mathrm{B}}$ and $M_{\mathrm{min}} = 2.45(4)\,\mu_{\mathrm{B}}$, $M_{\mathrm{min}}/M_{\mathrm{max}} = 0.80$. The angle between the major principle axis and the *c* axis is 50°. The phase between the moments at the Fe sites which are related by the inversion centre ($\bar{1}$) is $\phi_{\boldsymbol{k}} = 0.218(2) \cdot 2\pi$. A picture of the magnetic structure can be seen in Figure 4.3.

For the magnetic structure at 6.9 K no model could be fitted to the data successfully. 6.9 K is close to the paramagnetic transition at 8 K. As a consequence the magnetic reflections are weak and broad. Therefore it may be possible that the integration of the intensities was done incorrectly.

4.5 Natural Powder Sample at G4.1

A powder sample of the same natural crystal as used in [94] was measured in 1 K steps from 2 K to 11 K at *G4.1* spectrometer at the *Laboratoire Léon Brillouin* (*LLB*) with a wavelength of $\lambda = 2.423$ Å. The onset of magnetic ordering can be observed around 8 K, stable refinement of the magnetic structure can be attained up to 7 K. *FullProf* was used for refinement of the following magnetic models: spiral magnetic structures with moments in the *ac*, *ab*, *bc* pane and an additional model with the rotation plane tilted arbitrarily, *abc*. Sinusoidal spin-density waves

with moments in the *ac*, *ab*, *bc* plane and along the *a*, *b*, *c* axis and in arbitrary direction *abc*. As background a linear interpolation between a set of background points was chosen. The R values of all models are listed in Table 4.10.

In many cases it is not possible to distinguish among all different magnetic models solely on basis of a powder measurement. Measurements on a single crystal – either by collecting a large number of integrated intensities or by the use of polarised neutrons – are needed to unambiguously distinguish between the different magnetic models. The R values in Table 4.10 suggest the following magnetic structure: At 1.9 K, 3.4 K and 4.2 K a helical spiral with moments in the *ac* plane is most likely. Although for 1.9 K and 3.4 K slightly better results are achieved when a small *b* component is added to the rotation plane of the spiral. This component however is small and the improvement of the magnetic R value is too marginal to justify the need of the *b* component. At 4.2 K the model with the *b* component does not converge. At 5.1 K the transition from the spiral phase to the SDW can be observed; the moments remain in the *ac* plane during this transition. At 6.1 K and 7.1 K a SDW with moments in the *bc* plane yields slightly better results than a SDW with moments in the *ac* plane. However, at that temperature the magnetic peaks are weak and broad already. Therefore – also bearing in mind the results of the measurement with polarised neutrons and the symmetry analysis – the magnetic structure in the paraelectric phase most likely forms a SDW with moments in the *ac* plane.

Table 4.8 shows the lattice parameters and the propagation vector for the best fit (helix or SDW with moments in *ac* plane). The lattice parameters show no significant dependence of the temperature which was not to be expected anyway for the small temperature range. One might detect a slight increase of the propagation vector for the two highest temperatures on the other hand at that temperature the magnetic peaks are quite weak already and the results are not very reliable any more. Concluding, the propagation vector of the natural sample is $\boldsymbol{k} = (0, 0.77, 0)$. Table 4.9 shows the parameters of the magnetic structure at different temperatures for the favoured model. The transition from the helix to the SDW at about 5 K can be observed well. The data at 1.9 K and the Rietveld fit of a helical spiral with moments in the *ac* plane is shown in the upper panel of Figure 4.4.

T [K]	a [Å]	b [Å]	c [Å]	β [°]	k
1.9	9.6618(5)	8.7933(4)	5.2946(2)	107.334(3)	0.7704(6)
3.4	9.6623(5)	8.7927(4)	5.2948(2)	107.332(3)	0.7694(7)
4.2	9.6616(5)	8.7930(4)	5.2947(2)	107.329(3)	0.7686(9)
5.1	9.6627(5)	8.7938(4)	5.2952(2)	107.331(3)	0.770(1)
6.1	9.6627(5)	8.7943(4)	5.2953(2)	107.329(3)	0.774(3)
7.1	9.6625(5)	8.7943(4)	5.2951(3)	107.333(3)	0.776(6)

Table 4.8: Lattice parameters and magnetic propagation vector of natural powder of NaFeSi₂O₆ as determined at *G4.1*. The data displayed here belong to the best fit which is either a helix or a SDW with moments in the *ac* plane.

T [K]	M_{max} [μ_B]	M_{min} [μ_B]	$M_{\text{min}}/M_{\text{max}}$	$\measuredangle$	$\phi_{\boldsymbol{k}}/2\pi$
1.9	4.2	2.5	0.59	13°	0.21
3.4	4.1	2.0	0.50	16°	0.22
4.2	3.8	1.7	0.45	13°	0.22
5.1	3.5	0.1	0.03	12°	0.22
6.1	3.0	0	0	8°	0.22
7.1	2.8	0	0	5°	0.22

Table 4.9: Magnetic structure of natural powder of NaFeSi₂O₆ as determined at *G4.1*. The moments lie in the *ac* plane. At low temperatures they rotate in an elliptical helix. The lengths of the major and the minor principle axis of the ellipse are denoted with M_{max} and M_{min}. The angle between the major principle axis and the *c* axis is shown. $\phi_{\boldsymbol{k}}$ is the phase between the moments at the Fe sites which are related by the inversion centre ($\bar{1}$). Between 5 K and 6 K the magnetic structure evolves towards a transverse spin-density wave. All values are given to the last significant digit.

		spiral				SDW						
		ac	ab	bc	abc	ac	ab	bc	a	b	c	abc
1.9 K	Bragg R	3.31	3.63	3.41*	3.31	3.32	3.63	3.46*		4.35	3.45	3.32
	R_F	2.31	2.44	2.39*	2.31	2.38	2.44	2.40*		2.78	2.40	2.38
	Magnetic R	4.12	10.68	11.07*	4.07	5.51	10.72	10.01*		20.46	9.90	5.56
3.4 K	Bragg R	2.91	3.00	3.02	2.90	3.02	3.00	3.02	2.92	3.73	3.02	3.01
	R_F	2.23	2.19	2.35	2.21	2.27	2.19	2.35	2.37	2.62	2.35	2.26
	Magnetic R	5.55	10.99	9.70	5.44	6.17	11.01	9.70	37.03	20.42	9.63	6.22
4.2 K	Bragg R	3.10	3.06	3.17*		3.17	3.06	3.18*	3.01	3.67	3.17	3.16
	R_F	2.33	2.25	2.41*		2.39	2.25	2.46*	2.35	2.55	2.39	2.37
	Magnetic R	5.24	9.93	8.92*		6.22	9.91	8.67*	37.91	19.27	7.95	6.32
5.1 K	Bragg R	3.20	3.21	3.20	3.20	3.20	3.21	3.20	3.12	3.55	3.19	3.20
	R_F	2.46	2.42	2.45	2.46	2.47	2.42	2.45	2.51	2.62	2.45	2.46
	Magnetic R	6.19	11.88	6.61	6.72	6.18	11.88	6.59	50.73	18.46	6.86	6.39
6.1 K	Bragg R		3.58	3.38		3.38	3.58	3.38	3.42	3.70	3.38	3.38
	R_F		2.67	2.56		2.57	2.67	2.56	2.80	2.80	2.58	2.55
	Magnetic R		11.45	8.12		8.86	11.46	8.09	59.94	14.79	9.12	8.07
7.1 K	Bragg R	3.39*		3.25		3.22*	3.33	3.25	3.28	3.42	3.22	3.26*
	R_F	2.88*		2.76		2.74*	2.80	2.76	2.90	2.88	2.75	2.78*
	Magnetic R	26.33*		8.35		9.31*	10.14	8.37	80.47	11.77	9.90	10.61*

Table 4.10: R values of different magnetic models fitted to a powder sample of natural NaFeSi$_2$O$_6$ measured at *G4.1*. Models which run unstable are marked with an asterisk. Empty positions indicate the corresponding model does not converge.
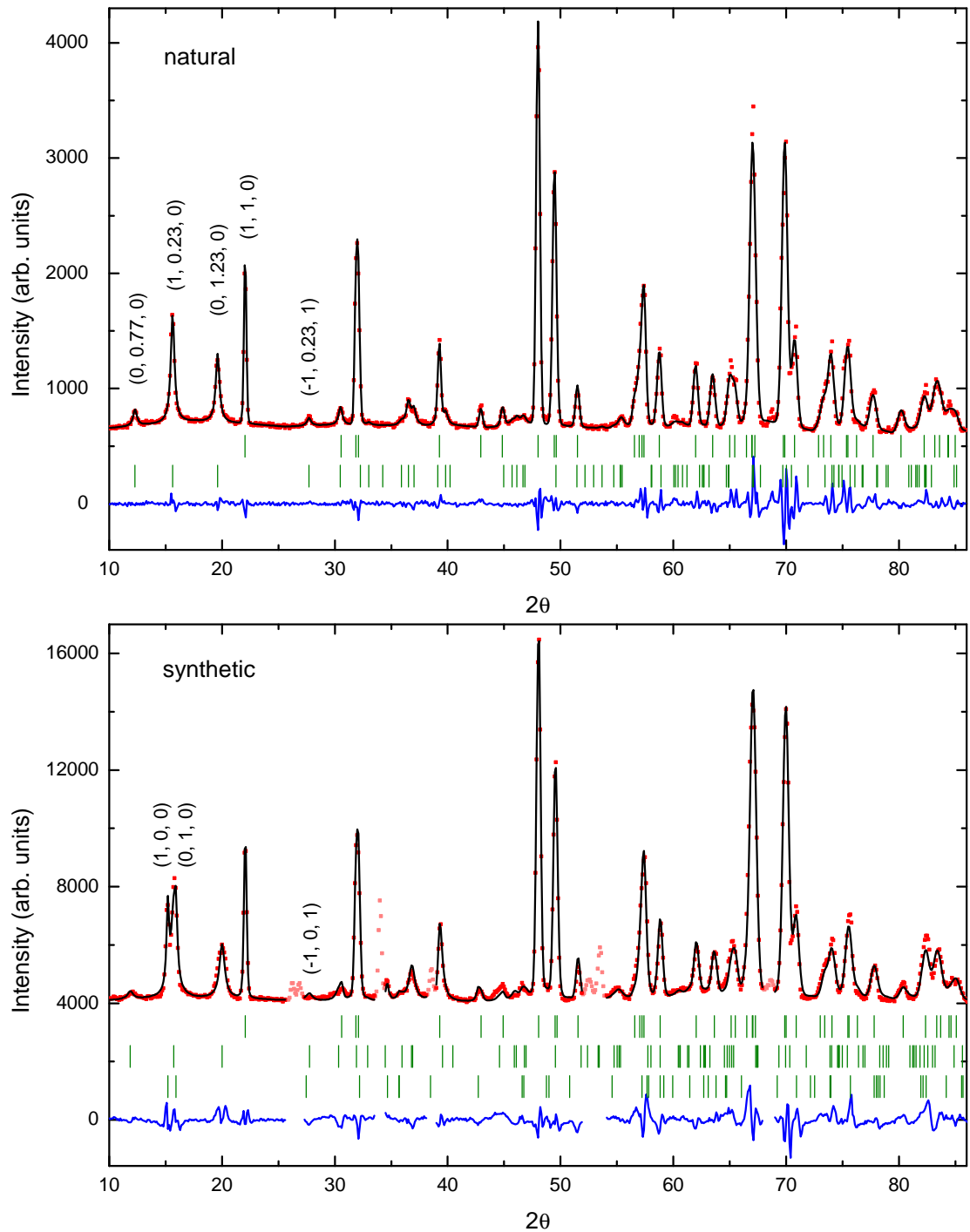
Figure 4.4: Rietveld fit of natural (1.9 K) and synthetic (1.5 K) NaFeSi$_2$O$_6$ powder measured at *G4.1* and refined with *FullProf*. The incommensurate magnetic structure is a helical spiral and the commensurate magnetic structure a SDW both with moments in the *ac* plane. The upper most green ticks indicate the structural Bragg-peak positions whereas the lower indicate the incommensurate magnetic (and commensurate for synthetic sample) Bragg-peak positions. Light red data are excluded from refinement.

4.6 Synthetic Powder Sample at G4.1

A powder sample of synthetic $NaFeSi_2O_6$ was measured at different temperatures at *G4.1 (LLB)* spectrometer with a wavelength of $\lambda = 2.423\,\text{Å}$. The results were already published in the PhD thesis of A.C. Komarek [110]. The data were revisited in the context of this thesis.

Overall, the sample quality is not as good as the quality of the natural sample. There are reflections which cannot be explained by the crystal structure. These reflections are clearly not of magnetic origin as they do not disappear in the paramagnetic regime. The following regions are excluded from the refinement: $25.7° - 27.2°$, $33.6° - 34.4°$, $38.2° - 38.9°$, $52.0° - 54.0°$, $68.0° - 68.9°$.

In addition to the magnetic reflections which can be indexed with the same incommensurate magnetic propagation vector as that of the natural sample, the synthetic sample shows reflections which can be described by a commensurate propagation vector $\boldsymbol{k} = (0, 1, 0)$. Thus the magnetic structure in the synthetic sample is a superposition of two magnetic structures. Two independent magnetic phases were fitted to the data. The following magnetic models were fitted to the incommensurate phase: spiral magnetic structures with moments in the *ac*, *ab*, *bc* pane and an additional model with the rotation plane tilted arbitrarily, *abc*. Sinusoidal spin-density waves with moments in the *ac*, *ab*, *bc* plane and in arbitrary direction *abc*. The moments of the commensurate phase were restricted to the same planes each time which seems to be a reasonable assumption. Due to the integer propagation vector the moments of the second phase are restricted to be of type up-down-up-down.[2] As background a polynomial with six coefficients was chosen. The R values of all models are listed in Table 4.13. The comparison of the different models confirms the previous results: at low temperature the incommensurate magnetic structure forms a helix with moments in the *ac* plane and between $5.5\,\text{K}$ and $6.5\,\text{K}$ it transforms into a SDW with moments while the moments remain in the *ac* plane; the commensurate phase forms an up-down-up-down structure with moments in the *ac* plane.

Table 4.11 shows the lattice parameters and the propagation vector for the best fit (helix or SDW with moments in *ac* plane plus superposition of up-down-up-down structure). The lattice parameters slightly increase with the temperature. One might detect a slight increase of the propagation vector for the two highest temperatures on the other hand at that temperature the magnetic peaks are quite weak already and the results are not very reliable any more. Concluding, the propagation vector of the synthetic sample is $\boldsymbol{k} = (0, 0.75, 0)$. Table 4.12 shows the parameters of the magnetic structure at different temperatures for the favoured model. The transition of the incommensurate part from the helix to the SDW takes place between $5.5\,\text{K}$ and $6.5\,\text{K}$. The data at $1.5\,\text{K}$ and the Rietveld fit of

---

[2]See the symmetry analysis in section 4.2 for a detailed discussion.

a helical spiral plus a superposition of an up-down-up-down structure both with moments in the *ac* plane is shown in the lower panel of Figure 4.4.

T [K]	a [Å]	b [Å]	c [Å]	β [°]	k
1.5	9.6357(6)	8.7767(5)	5.2895(3)	107.355(4)	0.746(1)
2.6	9.6359(6)	8.7768(5)	5.2897(3)	107.356(4)	0.746(1)
3.6	9.6358(6)	8.7764(5)	5.2894(3)	107.358(4)	0.747(1)
4.5	9.6358(6)	8.7775(5)	5.2899(3)	107.356(4)	0.749(1)
5.5	9.6367(6)	8.7775(5)	5.2899(3)	107.357(4)	0.750(2)
6.5	9.6371(5)	8.7783(5)	5.2902(3)	107.360(4)	0.752(4)

Table 4.11: Lattice parameters and magnetic propagation vector of synthetic powder of NaFeSi$_2$O$_6$ as determined at *G4.1*. The data displayed here belong to the best fit which is either a helix or a SDW with moments in the *ac* plane.

T [K]	$M_{\max}$ [μ_B]	$M_{\min}$	$M_{\min}/M_{\max}$	$\measuredangle$	$\phi_{\boldsymbol{k}}/2\pi$	M	$\measuredangle$	$\phi_{\boldsymbol{k}}/2\pi$
		$\boldsymbol{k} = (0, k, 0)$				$\boldsymbol{k} = (0, 1, 0)$		
1.5	4.7	2.0	0.42	10°	0.22	2.0	34°	−0.08
2.6	4.6	2.0	0.44	8°	0.22	1.9	30°	−0.07
3.6	4.7	1.6	0.34	11°	0.22	1.8	32°	−0.07
4.5	4.4	1.7	0.38	9°	0.21	1.7	35°	−0.09
5.5	4.2	1.4	0.32	12°	0.21	1.6	37°	−0.10
6.5	3.9	0	0	16°	0.20	1.4	39°	−0.12

Table 4.12: Magnetic structure of synthetic powder of NaFeSi$_2$O$_6$ as determined at *G4.1*. At low temperatures the magnetic structure is a superposition of an incommensurate helix and a commensurate up-down-up-down structure both with moments in the *ac* plane. The lengths of the major and the minor principle axis of the ellipse are denoted with $M_{\max}$ and $M_{\min}$. The angle between the major principle axis and the *c* axis is shown. $\phi_{\boldsymbol{k}}$ is the phase between the moments which are related by the inversion centre ($\bar{1}$). Between $5.5\,\mathrm{K}$ and $6.5\,\mathrm{K}$ the incommensurate part of the magnetic structure evolves towards a transverse spin-density wave. All values are given to the last significant digit.

		spiral				SDW			
		ac	ab	bc	abc	ac	ab	bc	abc
1.5 K	Bragg R	6.49	7.45	6.73	6.51*	6.49	7.08	6.72	
	R_F	4.54	5.21	4.66	4.48*	4.53	5.04	4.66	
	inc. R	11.25	23.77	13.22	12.57*	13.36	20.43	13.22	
	com. R	8.96	11.41	10.32	12.90*	9.57	9.46	10.33	
2.6 K	Bragg R	6.76	7.74	7.07*	7.36*	6.82	7.29	7.14	7.36
	R_F	4.87	5.48	5.02*	5.00*	4.87	5.34	5.01	5.00
	inc. R	11.08	24.57	14.48*	17.09*	13.07	20.35	14.56	17.09
	com. R	7.70	11.19	10.65*	31.46*	8.26	8.89	14.96	31.46
3.6 K	Bragg R	6.66	7.57	7.13*	6.69*	6.72	7.22	6.93*	6.89*
	R_F	4.65	5.18	4.77*	4.65*	4.66	5.12	4.75*	4.66*
	inc. R	11.55	22.50	13.54*	11.70*	13.02	21.60	12.60*	14.09*
	com. R	9.57	11.38	19.50*	10.75*	9.97	9.92	10.95*	17.07*
4.5 K	Bragg R	6.63	7.48	6.88*	6.90*	6.68	7.11	6.97*	6.69*
	R_F	4.72	5.15	4.85*	4.82*	4.73	5.14	4.84*	4.72*
	inc. R	11.50	20.45	13.06*	15.51*	13.63	21.65	13.69*	13.84*
	com. R	9.97	10.61	12.12*	26.06*	10.24	10.65	16.31*	12.55*
5.5 K	Bragg R	6.69	11.41*	7.00*	7.24*	6.69	7.33*	8.24*	6.85*
	R_F	4.64	12.45*	4.76*	4.91*	4.64	5.06*	5.45*	4.73*
	inc. R	9.83	32.55*	10.65*	9.36*	10.93	22.58*	60.59*	12.01*
	com. R	10.95	30.38*	15.63*	13.42*	11.31	11.43*	49.17*	16.63*
6.5 K	Bragg Rr	7.26*		7.10*		6.88	7.25		7.08*
	R_F	4.96*		5.01*		4.89	5.24		4.93*
	inc. R	13.88*		14.64*		11.28	26.86		13.37*
	com. R	13.21*		15.00*		13.69	12.70		21.67*

Table 4.13: R values of different magnetic models fitted to a powder sample of synthetic NaFeSi$_2$O$_6$ measured at *G4.1*. The magnetic structure is a superposition of an incommensurate and a commensurate structure. Models which run unstable are marked with an asterisk. Empty positions indicate that the corresponding model does not converge.

4.7 Pressure at 4F2

As we learned from the previous chapters the magnetic structure of $NaFeSi_2O_6$ is rather complex: commensurate and incommensurate magnetic structures coexist in a competitive situation. Natural single crystals all cut from the same large crystal show an incommensurate propagation vector and no evidence of commensurate magnetic order. Furthermore a slight deviation in the exact value of the incommensurability for different samples can be observed. The synthetic powder sample shows a superposition of a commensurate and an incommensurate structure. The deviation in the incommensurability for different samples and the absence or presence of the commensurate magnetic structure indicate that the magnetic structure in $NaFeSi_2O_6$ is highly frustrated and complex so that impurities have a high influence on it. The assumption that external parameters as hydrostatic pressure have a great influence on the magnetic structure, too, is obvious.

At the triple-axis spectrometer *4F2 (LLB)* the effect of hydrostatic pressure on the magnetic structure was investigated. Hydrostatic pressure up to $5\,\mathrm{kbar}$ was applied with a helium pressure cell. When increasing the pressure the cell must be heated above the melting point of the He. The sample was mounted
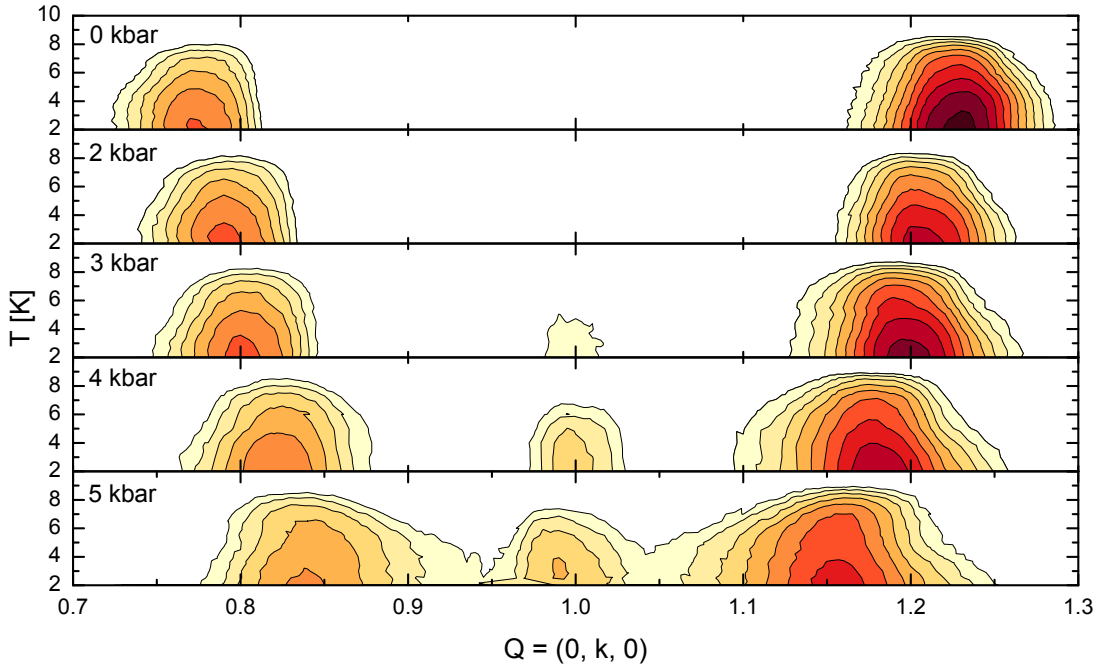
Figure 4.5: Natural $NaFeSi_2O_6$ under pressure at *4F2*. The propagation vector $\boldsymbol{k} = (0, k, 0)$ shifts to higher values with pressure and the intensity of the incommensurate order decreases. Most remarkably is the onset of the commensurate order already at relatively low pressure.

in the *ab* plane. Longitudinal scans across the magnetic peaks $(0, \sim 0.77, 0)$ and $(0, \sim 1.23, 0)$ and the commensurate position at $(0, 1, 0)$ at pressures up to $5\,\text{kbar}$ and varying temperature can be seen in Figure 4.5. At zero pressure no evidence of commensurate magnetic order can be seen here[3]. The propagation vector $\boldsymbol{k} = (0, k, 0)$ shifts to higher values with pressure and additionally the emergence of the commensurate order at $(0, 1, 0)$ can be observed. The intensity of the incommensurate order decreases whereas the intensity of the commensurate order increases. It can be assumed that at higher pressure the sample orders completely commensurate. This effect is reversible when going back and forth with pressure. The shift of the incommensurability with pressure is an expected feature, the emergence of the commensurate order at this rather low pressure is remarkable however.

---

[3]A very small component could be seen at *IN14*.

4.8 Conclusion

This chapter presents a comprehensive investigation of the magnetic structure of natural and synthetic NaFeSi$_2$O$_6$. Different neutron techniques were combined in a powerful way. The magnetic structure is incommensurate with propagation vector $\boldsymbol{k} = (0, 0.77, 0)$. The most likely model of the magnetic structure is a transverse spin-density wave with moments in the *ac* plane which sets in below 8 K and evolves into an elliptical helix with moments remaining in the *ac* plane below 6 K. The existence of a small *b* component cannot be excluded. However, its contribution is not chiral.

The measurement with spherical polarisation analysis at *IN14* gives most valuable advice on the magnetic structure. The results are more of qualitative value than of quantitative. In contrast to the powder measurements, which do not always favour a single model, the results of the measurement with spherical polarisation analysis are more reliable. The measurement with spherical polarisation analysis furthermore indicates that it is not a simple task to influence the magnetic structure by means of an electric field as for other multiferroica.

The measurement at the *D10* single-crystal diffractometer clearly confirms the low-temperature magnetic structure and gives a quantitative result. The size of the magnetic moment is 3.06 μ_B. The theoretical magnetic moment of Fe^{3+} is 5.92 μ_B. This deviation indicates that the magnetic moments are not completely ordered at that temperature, yet. The reason for that might be the high frustration of the magnetic structure. Another cause might be the replacement of some Fe^{3+} ions by other ions (see chemical analysis in Section 4.1).

The measurements of the natural and the synthetic powder at *G4.1* show on the one hand different results in the sense that the synthetic sample has an additional commensurate propagation vector, on the other hand the results for the incommensurate phases seem to be rarely influenced by that fact, as the agreement for the incommensurate magnetic structure is surprisingly good. Especially the natural sample exhibits the transition from the spiral to the SDW nicely. Overall, the powder samples reveal a larger magnetic moment and a flatter ellipse than the single-crystal measurement. Also the angle between the major axis and the *c* axis is found to be smaller in the powder measurements.

The pressure experiment at *4F2* reconciles the different behaviours of the synthetic and the natural sample. The magnetic structure in NaFeSi$_2$O$_6$ is highly frustrated, with the result that external parameters such as doping and pressure have great influence on the propagation vector.

With this data on the magnetic structure it is possible to exclude the inverse Dzyaloshinskii-Moriya interaction as the driving force in NaFeSi$_2$O$_6$ to be multiferroic. The inverse Dzyaloshinskii-Moriya interaction requires a cycloidal magnetic structure where the axis of spin rotation is perpendicular to the modulation vector $\boldsymbol{k}$ of the spin arrangement. In a helical magnetic structure the axis of spin

rotation is parallel to the modulation vector and the double cross product of the Dzyaloshinskii-Moriya term thus vanishes. The small b component, which cannot be excluded, has no chiral contribution and thus generates no Dzyaloshinskii-Moriya term.

The magnetic order in $NaFeSi_2O_6$ lowers the symmetry from $C2/c$ to $C2'$ which is a polar space group. The polar axis is *b* which is indeed the axis of spontaneous electric polarisation in $NaFeSi_2O_6$. Only on basis of symmetry considerations the following explanation of the spontaneous electric polarisation can be given: once the symmetries which keep the crystal from getting polar (here inversion and glide plane) are broken by the magnetic structure, nothing prevents the ions or electrons to shift towards a polar position and ferroelectricity sets in. The argument that a helical spin structure can induce ferroelectricity was also given by T. Arima [23]. A similar argumentation is given by R. Johnson et. al. [33].

There is a peculiarity about the mechanism generating ferroelectricity in $NaFeSi_2O_6$. Most multiferroics ($TbMnO_3$ [19], $MnWO_4$ [20], $Ni_3V_2O_8$ [21], $CuFeO_2$ [22, 23]) undergo a sequence of two second-order magnetic phase transitions. While the first requires a single irreducible representation and is non-polar the second requires two irreducible representations and is polar. Only the second transition breaks the remaining symmetries and generates the ferroelectric phase [24]. The proposed magnetic transitions in $NaFeSi_2O_6$ are restricted to a single irreducible representation. Why then does the first magnetic transition not give rise to ferroelectricity while the second does? Phenomenologically, a spin-density wave does not break inversion symmetry whereas a helix does. In the case of $NaFeSi_2O_6$ the incommensurate spin-density wave is not in accordance with the crystal lattice and the inversion symmetry is not a member of the little group, nevertheless the spin-density is not a chiral structure. The helix on the contrary is a chiral structure and does therefore break the crystal symmetry 'more'. B. Mettout et al. [24] discuss the appearance of just a single irreducible representation under the term *symmetry-replication mechanism*.

5 MnWO$_4$

In this chapter the investigations on the kinetics of electric field induced switching of chiral magnetic structures in multiferroic MnWO$_4$ are presented. On the one hand this topic is of fundamental research interest. On the other hand multiferroics are often regarded in the context of data storage devices such as non-volatile magnetic random access memory (RAM). For this application the writing speed is a crucial issue. Time-resolved neutron scattering was applied in order to investigate how fast the magnetic chirality adapts to an instantaneously switched electric field. Technical details of time-resolved neutron scattering are described in Section 2.4.

The time dependence of the multiferroic switching in MnWO$_4$ was investigated with two different samples at the triple-axis spectrometers *IN12* and *IN14* at the *Institut Laue-Langevin* (*ILL*). The results of both measurements are in good agreement. The main result is that the switching process in MnWO$_4$ takes place in the time scale of 2 ms to 30 ms which is much slower than anticipated.

Hübnerite (MnWO$_4$) is a naturally occurring mineral. It crystallises in the monoclinic space group $P2/c$ ($a = 4.823$ Å, $b = 5.753$ Å, $c = 4.992$ Å, $\beta = 91.08°$). MnWO$_4$ undergoes a sequence of magnetic phase transitions. Below 13.5 K (AFM3) an incommensurate sinusoidal spin-density wave with collinear moments in the ac plane forming an angle of 35° with the a axis and propagation vector $\boldsymbol{k} = (-0.241, \frac{1}{2}, 0.457)$ sets in. Below 12.3 K (AFM2) an additional b component

AFM1	AFM2	AFM3	PM
↑↑↓↓	spiral	SDW	
$\boldsymbol{m}$ in ac plane	$\boldsymbol{m}$ in ac plane $+ b$	$\boldsymbol{m}$ in ac plane	
	FE, $\boldsymbol{P} \parallel \boldsymbol{b}$		
$\boldsymbol{k} = (-\frac{1}{4}, \frac{1}{2}, \frac{1}{2})$	$\boldsymbol{k} = (-0.214, \frac{1}{2}, 0.457)$		
	8 K	12.3 K	13.5 K
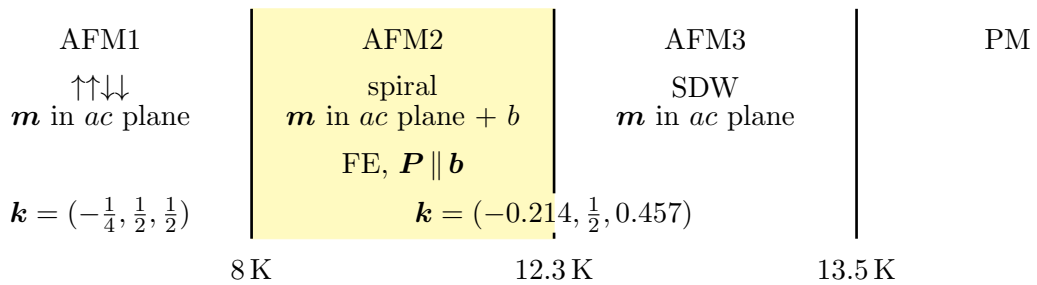
Figure 5.1: Magnetic phase diagram of MnWO$_4$. MnWO$_4$ undergoes a sequence of magnetic phase transitions. The transition in the spiral phase is accompanied by the onset of spontaneous electric polarisation. The transition at 8 K is of first order while the other transitions are of second order. Data are taken from Reference [20].

evolves and the moments order in an elliptical spiral which intercepts the ac plane in the direction of the magnetic moments of AFM3. Below $8.0\,\mathrm{K}$ (AFM1) the system orders collinear again with moments in the ac plane forming an angle of $37°$ with the a axis but with commensurate propagation vector $\boldsymbol{k} = (-\frac{1}{4}, \frac{1}{2}, \frac{1}{2})$. The moments order in an up-up-down-down ($\uparrow\uparrow\downarrow\downarrow$) structure which is a special case of a sinusoidal structure with propagation vector $k = \frac{1}{4}$. [20]

At the transition to the non-collinear state (AFM3 $\rightarrow$ AFM2) spontaneous electric polarisation parallel b develops continuously. At the transition back into the collinear state (AFM2 $\rightarrow$ AFM1) the electric polarisation disappears discontinuously. Just before this transition the polarisation reaches its maximum of $P_b \approx 60\,\mathrm{\mu C/m^2}$. [29–31]

MnWO$_4$ being multiferroic can be explained by the inverse Dzyaloshinskii-Moriya interaction. The direction of the electric polarisation $\boldsymbol{P}$ is given by $\boldsymbol{P} \propto \sum_{ij} \boldsymbol{e}_{ij} \times (\boldsymbol{S}_i \times \boldsymbol{S}_j)$ where $\boldsymbol{S}_i$ and $\boldsymbol{S}_j$ are the magnetic moments of neighbouring manganese ions and $\boldsymbol{e}_{ij}$ points along the connection line of the corresponding ions. As the moments rotate in an ellipse, whose basal plane intercepts the ac plane at an angle of $35°$ and furthermore is not inclined with respect to the b axis, the cross product $\boldsymbol{S}_i \times \boldsymbol{S}_j$ lies in the ac plane forming an angle of $125°$ with the a axis. The manganese ions form zigzag chains along the c direction; in average the connection line is along the c axis, $\langle \boldsymbol{e}_{ij} \rangle \parallel \boldsymbol{c}$. Finally, $\langle \boldsymbol{e}_{ij} \rangle \times (\boldsymbol{S}_i \times \boldsymbol{S}_j) \parallel \boldsymbol{b}$ predicts the polarisation P along the b axis. [29]

The ferroelectric polarisation in MnWO$_4$ can be turned from the b direction to the a direction when a magnetic field above $10\,\mathrm{T}$ is applied along the b axis [29]. The observation of the effect of an electric field on the magnetic structure is more difficult to study, as a complex antiferromagnetic order requires a microscopic technique for observation. By the use of polarised neutrons the direct observation of the electric-field induced switching of the chiral magnetism has been observed in MnWO$_4$ where full hysteresis loops (chiral ratio vs. electric field) were recorded [115–117].

5.1 Time-Dependent Measurements at IN12

For spherical polarisation analysis *CRYOPAD III* was installed on the *IN12* (*ILL*) triple-axis spectrometer. The sample was mounted in the $(0\,1\,0)/(-0.214, 0, 0.457)$ plane. The magnetic peak $(-0.214, 0.5, 0.457)$ had an intensity of $400\,\mathrm{cnts/s}$. The flipping ratio at $(0\,2\,0)$ was 26 ($90\,\mathrm{cnts/s}$) and at $(1\,0\,\bar{2})$[1] it was 41 ($260\,\mathrm{cnts/s}$). The electric field was applied along the b direction by two aluminium plates which were fixed with four nylon screws to the sample, see Figure 5.2. The sample was $1.98\,\mathrm{mm}$ thick. It was grown from melt by P. Becker.

For all measurements of the chiral ratio the spectrometer was placed right at the centre of a peak and for each neutron-polarisation channel just one point was recorded rather than scanning the whole peak. This proceeding is justified if the amplitude is directly proportional to the area which is the case when the full width at half maximum is constant. This requirement was checked carefully for different electric fields with the result that the proposed measuring technique is justified.

Prior to the time-resolved measurements some static investigations were undertaken. A sequence

Figure 5.2: Sample holder of $MnWO_4$. The electric field is applied by two aluminium plates which are fixed by four nylon screws. The sample is $1.98\,\mathrm{mm}$ thick.

of five cooling cycles in different electric fields was recorded, Figure 5.3. The first measurement (the sample had not seen any electric field yet) in zero electric field was a temperature scan from $20\,\mathrm{K}$, which is well in the paramagnetic regime, to $6\,\mathrm{K}$ of both spin-flip channels in the x direction, which are directly linked to the chiral ratio via Equation (2.13). Thereafter, the procedure was repeated with electric fields of $1\,\mathrm{kV/mm}$, $0\,\mathrm{kV/mm}$, $-1\,\mathrm{kV/mm}$, and $0\,\mathrm{kV/mm}$. The obtained maximal chiral ratios were -0.11, 0.48, 0.10, -0.48, 0.05, respectively. The following transition temperatures can be observed: onset of magnetic order at $13.0\,\mathrm{K}$, development of chiral component at $12.6\,\mathrm{K}$ (splitting of both spin-flip channels) and transition to commensurate phase at $7.5\,\mathrm{K}$. These transition temperatures are in good agreement with the values found in literature. The chiral ratio can be influenced effectively by the electric field. The virgin sample (no electric field seen yet) already shows a small chiral ratio of -0.11. The chiral ratio can be reversed and increased by an electric field to 0.48. After heating into the paramagnetic regime and cooling again without electric field the sample remembers its former

---

[1]In order to reach this reflection the sample has to be tilted slightly out of the scattering plane.
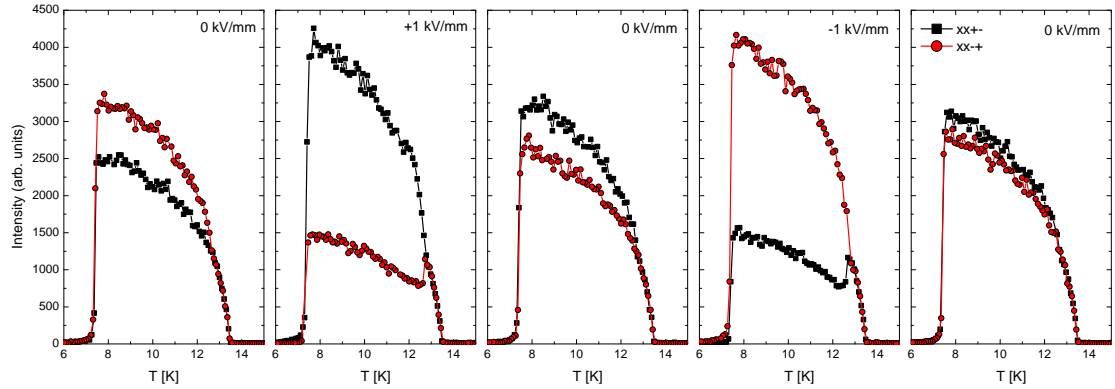
Figure 5.3: Temperature scans of the two spin-flip channels in x direction at different electric fields measured at the incommensurate magnetic reflection $(-0.214, 0.5, 0.457)$. The succession of the measurements is from left to right.

state and develops a chiral ratio of 0.10. The absolute value is comparable to the former zero-field state but the sample remembers the positive sign of the last electric field it saw. The chiral ratio can be fully switched to -0.48 by a reversed electric field. After reheating and removing the electric field the sample develops a chiral ratio of 0.05. This time the crystal seems not to remember the last field seen but remembers the first field it ever saw after cooling from room temperature. This complicated behaviour depending on the history of the sample was also reported by Th. Finger et al. [116]. The authors of this reference observed a maximal chiral ratio in of ±0.8. To a high degree the properties of a sample are thus intrinsic.

The influence of the cooling field on the development of a preferred chirality can also be observed when driving hysteresis loops (chiral ratio vs. electric field). The hysteresis loops were recorded after cooling from 20 K to 10 K in an applied electric field of ±1 kV/mm. The saturation value of the chiral ratio is ±0.48 and can be fully reversed. The crystal develops a preferred chirality depending on the field which is applied during cooling from the paramagnetic phase and can be arbitrarily chosen. A higher field is needed to force the sample in the non-preferred state and a lower field to return in the preferred state. As a consequence the hysteresis loop gets shifted with respect to the electric field, as can be seen in Figure 5.4. This is in accordance with former results, compare [116, 117].

After these preliminary investigations the time dependence was investigated. The time of flight of the neutrons has to be regarded. All data have been shifted so that the onset of the switching process coincides with the reversal of the electric field. During the experiment a strong dependence on the succession of the individual switching processes was observed. For this reason the results are presented in the same succession as they were performed.

In the first experiment an electric field of ±1.2 V/mm was switched at a fre-
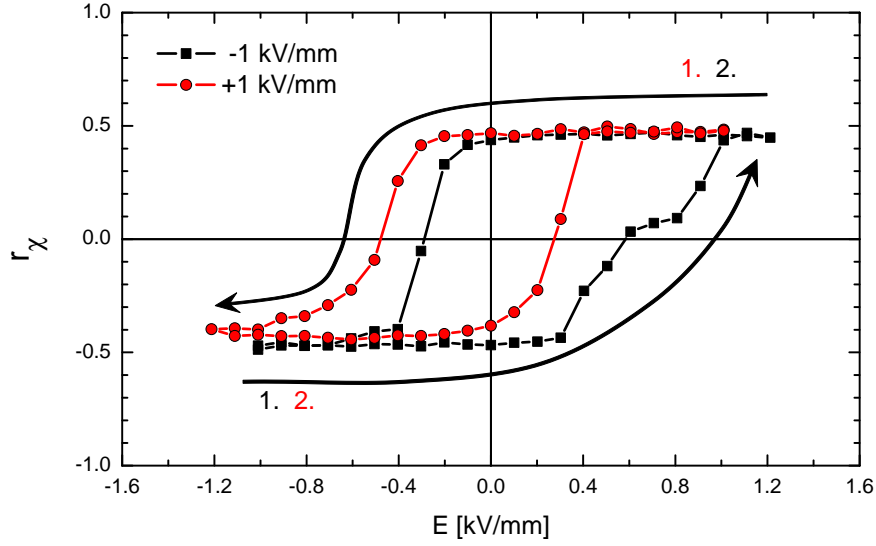
Figure 5.4: Static hysteresis loop obtained by measuring the chiral ratio as a function of external electric field at constant temperature. The loops were recorded after field cooling from $20\,\mathrm{K}$ to $10\,\mathrm{K}$ in $E = \pm 1\,\mathrm{kV/mm}$. Note the coercive field depends on the field direction applied during cooling.

quency of $8\,\mathrm{Hz}$. The response of the sample was observed in a temperature range from $12.5\,\mathrm{K}$ to $7.5\,\mathrm{K}$. Prior to this the sample was cooled from $20\,\mathrm{K}$ to $12.5\,\mathrm{K}$ in a field of $+1.2\,\mathrm{kV/mm}$. Three curves at different temperatures are shown in Figure 5.5. It is possible to switch the magnetic chirality between the two saturation values and the same amplitude as for the static hysteresis loop can be reached. Furthermore the relaxation time is shorter when the system goes into its preferred state and longer when it is forced to respond to the electric field in the other direction. At the temperature closer to the phase transitions the system is softer (i.e. it responds faster to the reversed field).

The following function was fitted to the data [118]

$$
\begin{aligned}
y(t) = \quad & \frac{1}{2}\left[1 - \tanh\left(\frac{t - t_0}{0.001\,\mathrm{ms}}\right)\right]\left[A_2 + (A_1 - A_2)\mathrm{e}^{-\left(\frac{t}{t_1}\right)^{b_1}}\right] \\
& + \frac{1}{2}\left[1 + \tanh\left(\frac{t - t_0}{0.001\,\mathrm{ms}}\right)\right]\left[A_2 + (A_1 - A_2)\left(1 - \mathrm{e}^{-\left|\frac{t - t_0}{t_2}\right|^{b_2}}\right)\right]
\end{aligned}
$$

The hyperbolic tangent yields a continuous approximation of the Heaviside step function which describes the instantaneous reversal of the electric field. t_0 is half of the switching period when the direction of the electric field is reversed. $t_{1,2}$ are the characteristic relaxation times. A_1 and A_2 describe the minimal and maximal chiral ratio, respectively.
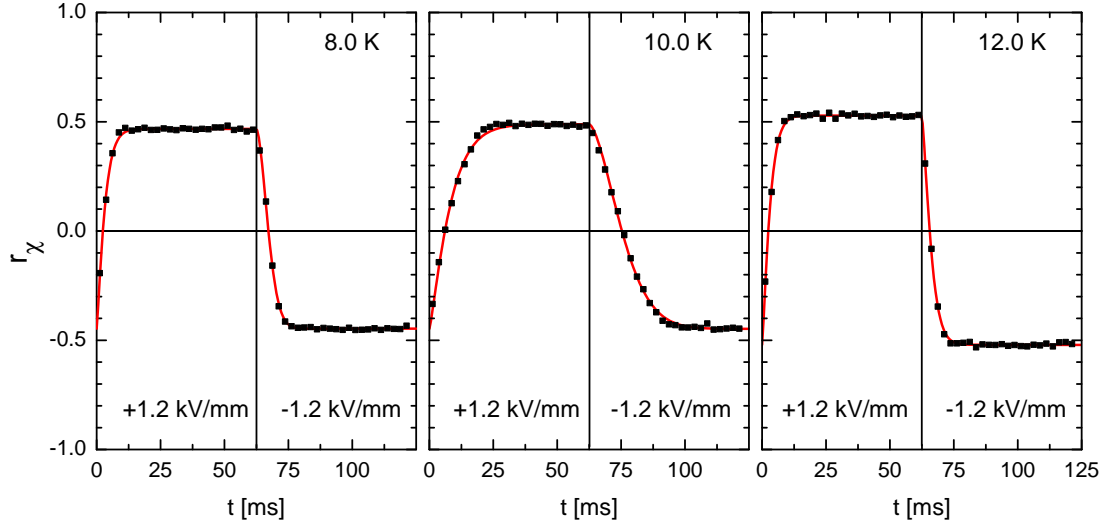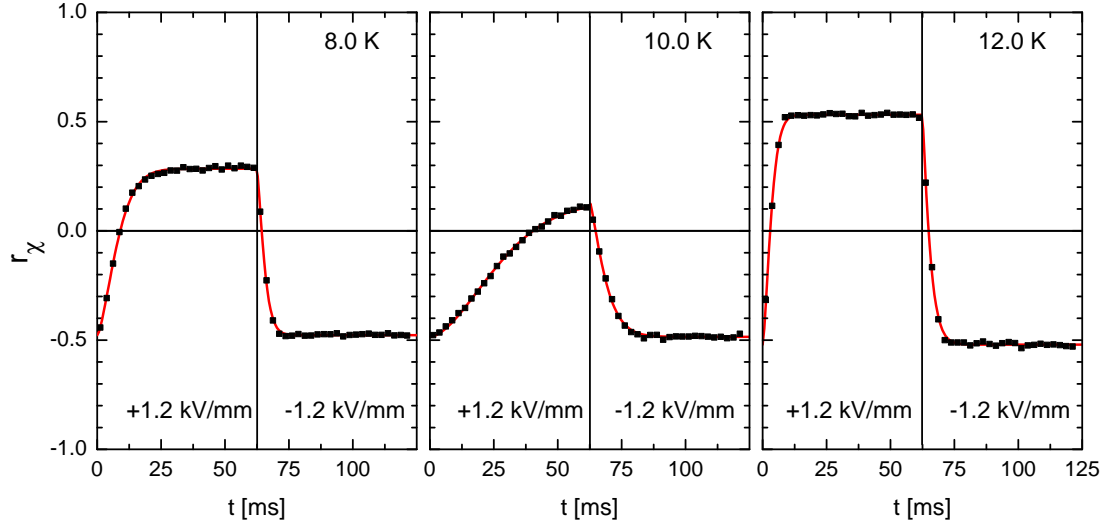
Figure 5.5: Time-dependent measurement of the magnetoelectric switching at different temperatures. The sample was cooled from 20 K in an electric field of +1.2 kV/mm. The electric field is switched with a frequency of 8 Hz and an amplitude of ±1.2 kV/mm with a rise time of 0.2 ms. The chiral ratio can approximately be switched in the same range as in the static hysteresis loop. The relaxation time differs strongly for the two states.
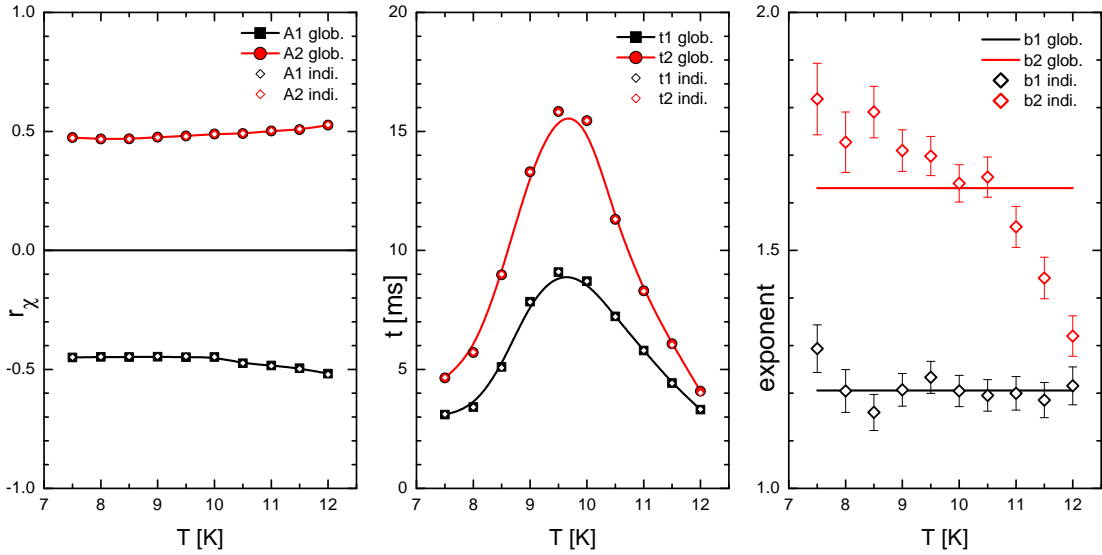
Figure 5.6: Characteristics of the switching behaviour for field cooling +1.2 kV/mm. The electric field is switched with a frequency of 8 Hz and an amplitude of ±1.2 kV/mm. The influence of fitting the exponent individually for each temperature or globally for all temperatures on the saturation value of the chiral ratio and the characteristic relaxation time is negligible. The temperature was decreased during the measurement.

Figure 5.7: Time-dependent measurement of the magnetoelectric switching at different temperatures. The sample was cooled from 20 K in an electric field of $-1.2 \, \text{kV/mm}$. Frequency: 8 Hz, amplitude: $\pm 1.2 \, \text{kV/mm}$. The switching behaviour is asymmetric.
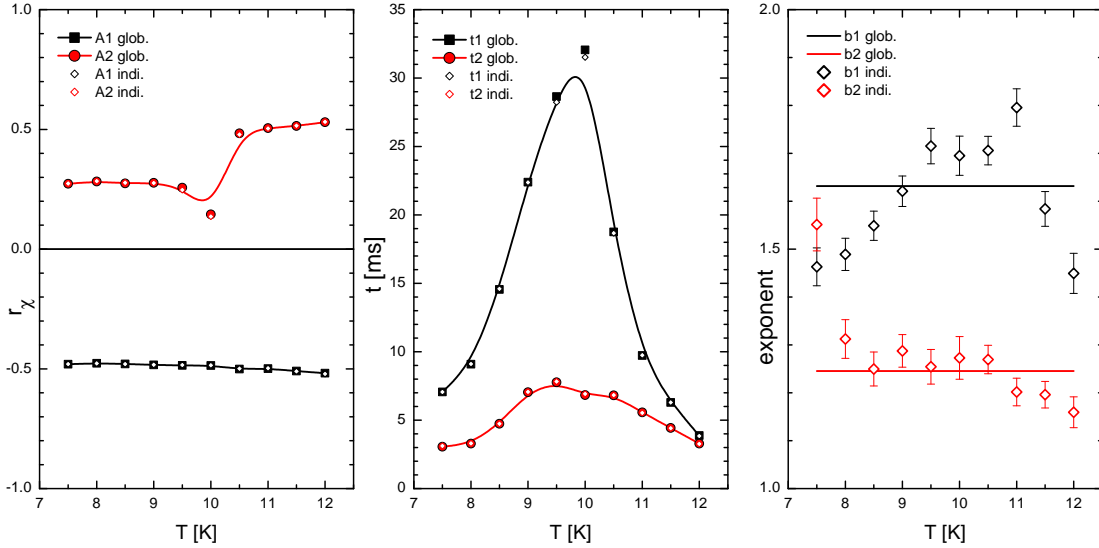
Figure 5.8: Characteristics of the switching behaviour for field cooling $-1.2 \, \text{kV/mm}$. Frequency: 8 Hz, amplitude: $\pm 1.2 \, \text{kV/mm}$. The influence of the exponents on the saturation value of the chiral ratio and the characteristic relaxation time is negligible. The temperature was decreased during the measurement.

The relaxation is discussed on the basis of the Avrami model [119–122]. The exponent b should be between 1 and 2. For one dimensional domain growth the Avrami model predicts an exponent of 2, when assuming constant nucleation, and 1, when assuming nucleation only in the beginning. The exponent cannot be fitted reliably to the data. It varies strongly for different temperatures, see Figure 5.6. The data analysis was done once with global refinement and once with individual refinement of the exponents b_1 and b_2. All parameters are displayed in Figure 5.6. Fortunately, the exponent has only small influence on the saturation value of the chiral ratio and the characteristic relaxation time. The properties which were already discussed at the three example scans (Figure 5.5) are confirmed by the whole temperature run. An interesting observation is that the saturation of the chiral ratio decreases slightly with temperature. This behaviour might be a function of temperature or more likely due to fatigue of the sample as the temperature was reduced during the measurement.

In addition the effect of the frequency on the switching behaviour was investigated. At 10 K the following frequencies were used: 10 Hz, 12 Hz, 5 Hz, 8 Hz, 20 Hz, and 40 Hz. The overlay of the curves at 5 Hz, 10 Hz, 20 Hz, and 40 Hz in Figure 5.9 exhibits the preferred state clearly. When the electric field is switch faster than the system can respond, it will not follow the whole way but it will follow at the same rate and thus will not reach the opposite chiral ratio. It is noteworthy, that the crystal always reaches the saturation value for the preferred state. If the sample was symmetric with respect to the electric field one would expect a more symmetric curve, i.e. the saturation values of the maximal and minimal chiral ratio would be equal in size and both decrease for increasing frequency.

During the experiment it appeared that the sample showed irreversible changes. Especially switching at high frequencies caused fatigue. Runs which were done at 10 K and 8 Hz with different history of the sample prove this assumption. The run which was done in the beginning of the measurement during the temperature scan was used as reference. At this time the chiral ratio could be flipped almost completely (+0.49, −0.45), compare Figure 5.5. Later, after the sample had been switched with 12 Hz, the preferred chirality stayed almost the same (+0.48) but the non-preferred chirality decreased to −0.28, compare Figure 5.9. It is not possible to distinguish whether this is due to the former switching at 12 Hz or to a general process of fatigue. After switching at 40 Hz all parameters stay more or less the same. This speaks for general fatigue rather than destroying the sample by applying too high of a frequency. After this the sample was heated to 20 K and cooled again. The sample did not restore to its reference values. So the sample was heated to 120 K in the hope that would restore the sample. This was not accomplished. Possibly structural defects or mechanical tension influencing the magnetic and polar order, which do not heal when going far beyond the magnetic phase transition, were induced into the sample by the repeated switching.

The influence of the amplitude of the switching field on the switching be-
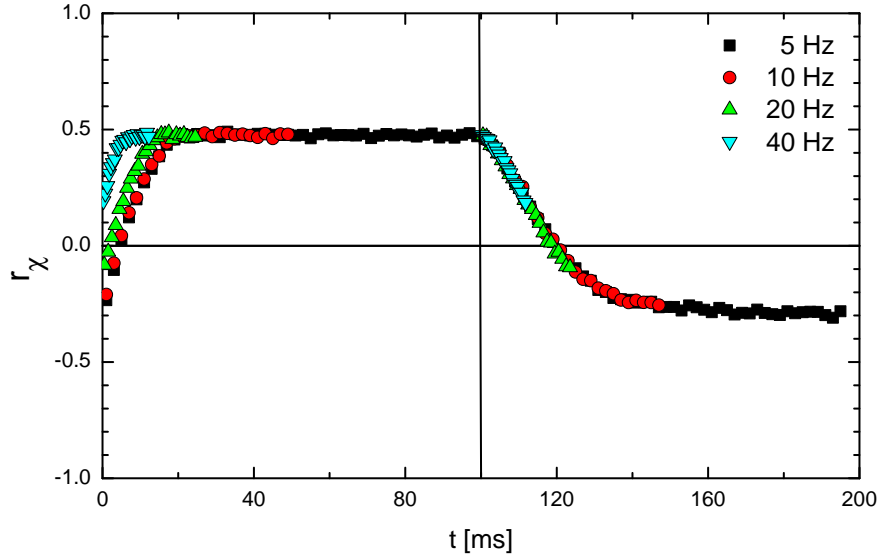
Figure 5.9: Switching at different frequencies. At 10 K the electric field is switched with different frequencies and an amplitude of $\pm 1.2\,\mathrm{kV/mm}$. The system clearly develops a preferred state. At high frequencies the time is too short to completely adapt to the non-preferred state. The data are shifted in the time axis such that the time of the switch coincides for the different frequencies.

haviour was investigated by three measurements with $1.2\,\mathrm{kV/mm}$, $1.4\,\mathrm{kV/mm}$, and $1.5\,\mathrm{kV/mm}$, respectively, Figure 5.10. The difference in the three applied amplitudes is straightforward: when switching from the non-preferred state into the preferred state the field of $1.2\,\mathrm{kV/mm}$ already exceeds the minimal required field (i.e. the field at which the system is willing to adapt to its preferred state). The time constant and the saturation value stay almost the same for all three fields. When switching into the non-preferred state, the system is unwilling to follow. By applying a higher field the chirality is switched faster and the saturation value is increased. This can be understood easily by considering the higher driving force of the higher field.

Nevertheless the sample had suffered non-reversible changes in its properties, in the last series of scans it was investigated whether the preferred chirality can be changed by reversing the field during cooling. The sample was heated to 20 K and recooled in a field of $-1.2\,\mathrm{kV/mm}$. The switching behaviour in a temperature range from 12.5 K to 7.5 K was recorded. Three curves at different temperatures are shown in Figure 5.7. As expected the sample now has a preference to a negative chiral ratio which is in accordance with the field applied during cooling. At 10 K the relaxation time exceeds half of the period of the applied electric field, as a consequence the positive saturation value of the chiral ratio is not reached. Comparing the fit parameters of the two temperature runs (Figure 5.6
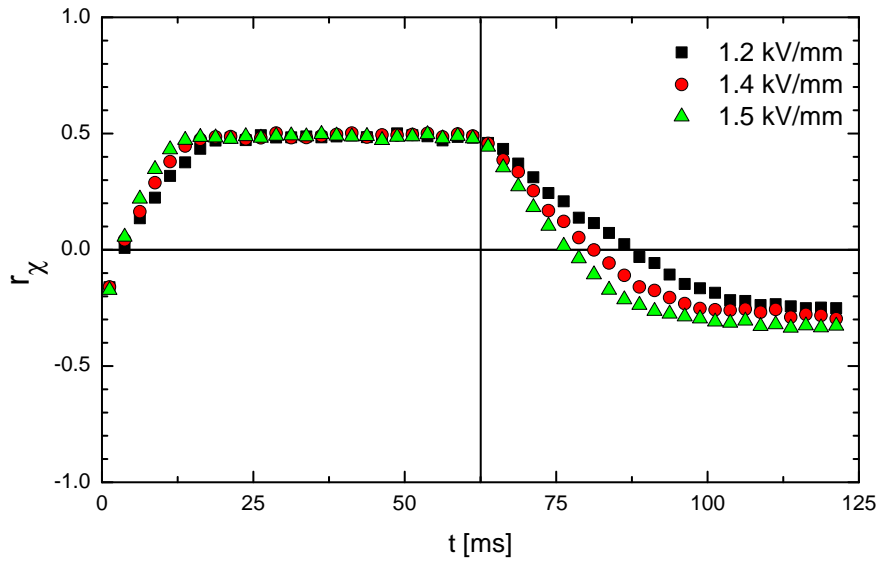
Figure 5.10: Switching with different electric field strength at 10 K and 8 Hz. Higher fields yield a higher driving force and thus a faster respond.

with Figure 5.8) reveals reversed behaviour. Now the saturation of the negative chiral ratio exceeds the saturation of the positive chiral ratio. However the positive (non-preferred) saturation value shows a less smooth curve than before. The kink at 10 K is a consequence of the long relaxation time at that temperature where the saturation value of the chiral ratio is not reached for positive electric field. The behaviour of the time constants is also reversed. Now the time needed to switch to the positive chiral ratio exceeds the time needed to switch to the negative chiral ratio. The time to switch to the non-preferred chirality now is much longer than it was in the series done before.

5.2 Time-Dependent Measurements at IN14

The measurement was repeated at *IN14* with a different sample in order to investigate which properties were specific to the sample and which ones of general nature. The sample [E/H3] was 0.89 mm thick. It was grown from melt solution by P. Becker. A standard Helmholtz setup was used for polarisation analysis. With a Helmholtz setup only the diagonal terms of the polarisation matrix are available. Because the chiral ratio can be obtained with the strongest intensity by measuring both spin flip channels in the x direction this is sufficient. In fact the Helmholtz setup is preferable when one is interested in the diagonal terms of the polarisation matrix only because it is experimentally easier to handle and provides higher intensity than *CRYOPAD*. Another advantage is that the goniometers can tilt in a wider range, so the sample alignment is much easier. The intensity of the magnetic reflection $(-0.214, 0.5, 0.457)$ was 1400 cnts/s.

The hysteresis loop of a zero-field cooled sample is shown in Figure 5.11. The sample was cooled to 10 K in zero electric field and then a negative field of -1.25 kV/mm was applied. The saturation value of the chiral ratio is ± 0.85 which is significantly higher than for the other sample investigated before but it is consistent with values observed by Th. Finger et al. [116]. The hysteresis loop is not perfectly symmetric but shows a clear preference for negative electric fields which was the first field it saw after cooling. Especially a high positive electric field is needed to reach saturation. For that reason the amplitude of the switching
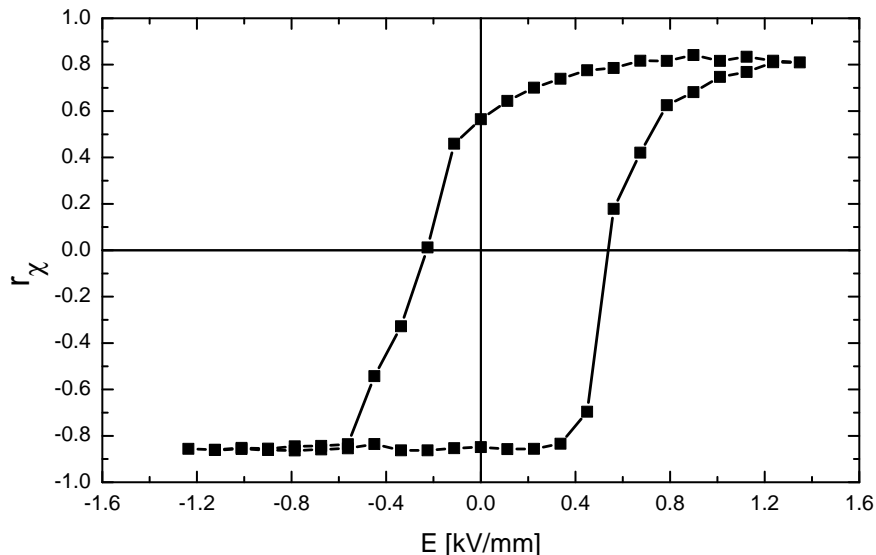

Figure 5.11: Static hysteresis loop obtained by measuring the chiral ratio as a function of external electric field at constant temperature. The loops were recorded after zero-field cooling to 10 K and then a negative field was applied.
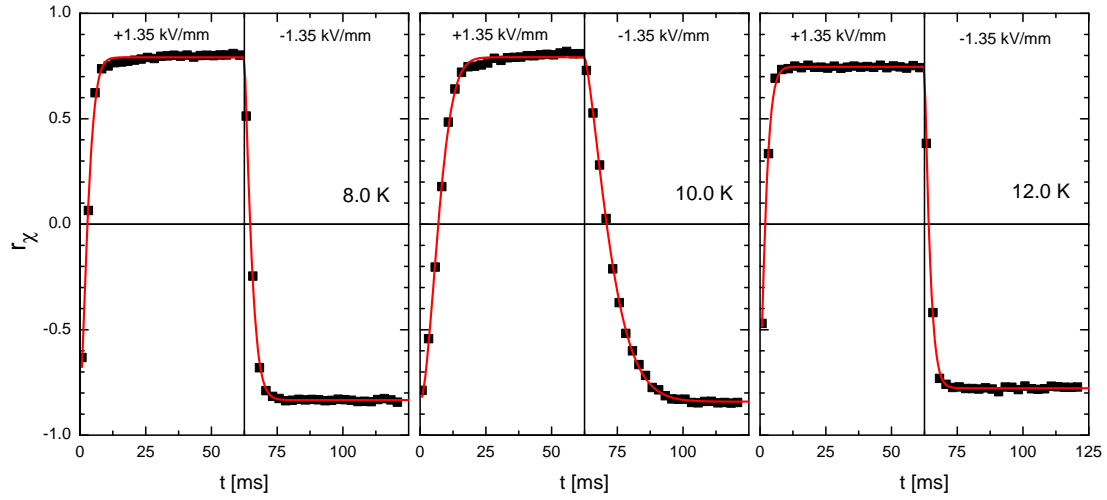
Figure 5.12: Time-dependent measurement of the magnetoelectric switching at different temperatures. The sample was cooled from 20 K in an electric field of +1.35 kV/mm. The electric field is switched with a frequency of 8 Hz and an amplitude of ±1.35 kV/mm. The relaxation times and the saturation values are quite symmetric for both field directions.
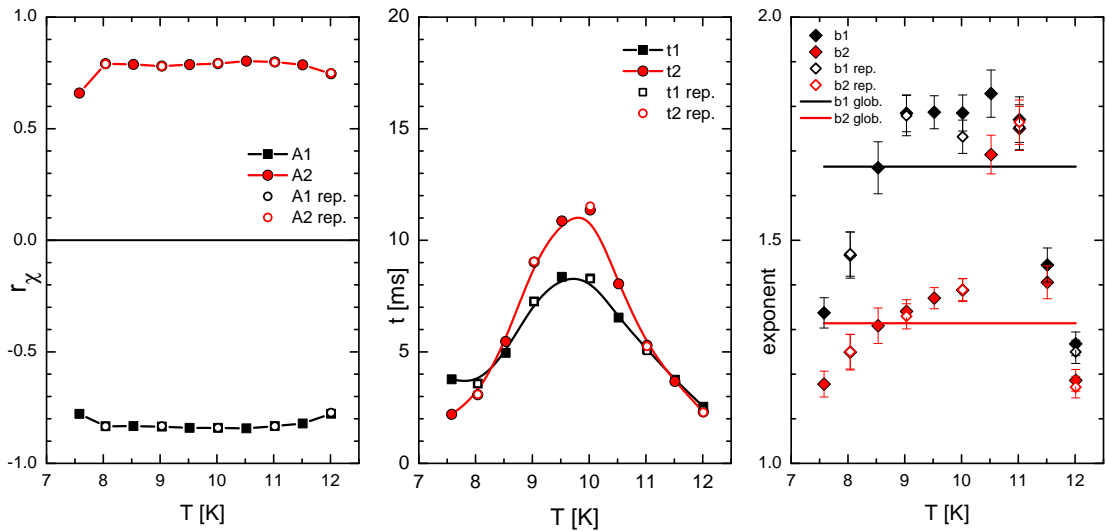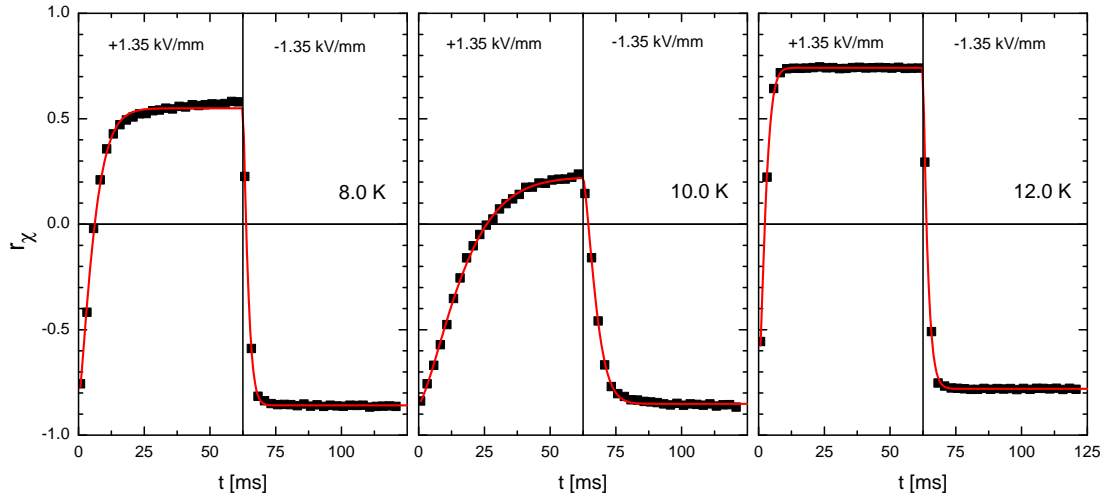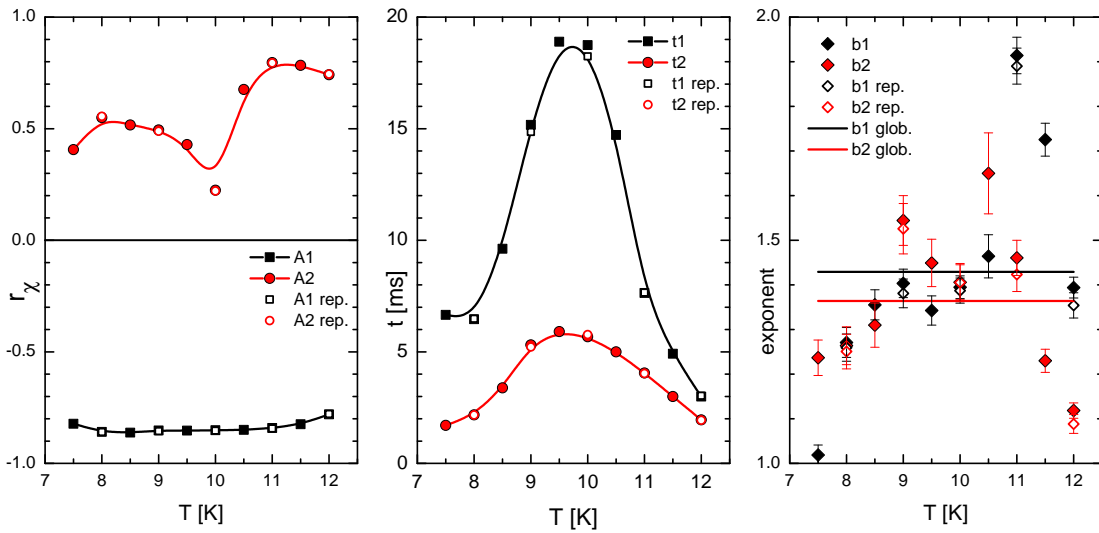

Figure 5.13: Characteristics of the switching behaviour for field cooling +1.35 kV/mm from 20 K. The electric field is switched with a frequency of 8 Hz and an amplitude of ±1.35 kV/mm. The first run was done with 0.5 K steps from 12 K to 7.5 K. Afterwards the sample was reheated to 20 K and the run was repeated with 1 K steps. All data are perfectly reproducible.

Figure 5.14: Time-dependent measurement of the magnetoelectric switching at different temperatures. The sample was cooled from $20\,\mathrm{K}$ in an electric field of $-1.35\,\mathrm{kV/mm}$. The electric field is switched with a frequency of $8\,\mathrm{Hz}$ and an amplitude of $\pm1.35\,\mathrm{kV/mm}$. The relaxation times and the saturation values behave extremely asymmetric for both field directions.

Figure 5.15: Characteristics of the switching behaviour for field cooling $-1.35\,\mathrm{kV/mm}$ from $20\,\mathrm{K}$. The electric field is switched with a frequency of $8\,\mathrm{Hz}$ and an amplitude of $\pm1.35\,\mathrm{kV/mm}$. The first run was done with $0.5\,\mathrm{K}$ steps from $12\,\mathrm{K}$ to $7.5\,\mathrm{K}$. Afterwards the sample was reheated to $20\,\mathrm{K}$ and the run was repeated with $1\,\mathrm{K}$ steps. All data are perfectly reproducible.

field was chosen to be $\pm 1.35\,\text{kV/mm}$ which is slightly higher than for the other sample. Due to lack of time it was abstained from recording further hysteresis loops and checking whether field cooling would produce two different preferred states; instead time-resolved measurements were recorded right away.

For the time-resolved measurements the sample was field cooled from $20\,\text{K}$ in an electric field of $+1.35\,\text{kV/mm}$. Then the field was switched with a frequency of $8\,\text{Hz}$ and an amplitude of $\pm 1.35\,\text{kV/mm}$. The temperature was reduced in $0.5\,\text{K}$ steps from $12.0\,\text{K}$ to $7.5\,\text{K}$. Thereafter the temperature was raised to $20\,\text{K}$ again and the procedure was repeated with $1\,\text{K}$ steps. By doing so the reproducibility of the results was checked. The obtained data are perfectly reproducible. For all data the exponent was again fitted individually and globally. Again, the influence on the characteristic relaxation time and the saturation value is negligible. Figure 5.12 shows three example scans. All fitted parameters are displayed in Figure 5.13. The characteristic relaxation time is shorter than for the sample measured at *IN12* and both times t_1 and t_2 are almost equal. Overall this sample exhibits a more symmetric performance. Additionally, this sample displays a long-term relaxation process which can be observed at $8\,\text{K}$ and $10\,\text{K}$ in Figure 5.12 and at $8\,\text{K}$ in Figure 5.14. The main part of the chiral ration adapts to the new field in less than $10\,\text{ms}$. Hereafter the chiral ratio still increases but on a much lower time scale. This behaviour was not observed at the other sample studied at *IN12*.

The same procedure was repeated for a negative cooling field of $-1.35\,\text{kV/mm}$. The results are displayed in Figures 5.14 and 5.15. This time the sample develops a clear preference for negative field and shows asymmetric behaviour. The time constants differ strongly and the saturation of the chiral ratio is only reached for negative field. Again, the obtained data are perfectly reproducible; even the kink in the positive saturation values. Most remarkably is that the kink in the positive saturation values resembles the kink measured in the other specimen at *IN12* which is also located at $10\,\text{K}$. A possible explanation for that might be that the static hysteresis loop recorded in the beginning was recorded at $10\,\text{K}$. Possibly this might have imprinted a preferred state. However this explanation seems somewhat speculatively.

5.3 Conclusion

The time-dependence of the magnetoelectric switching in $MnWO_4$ was observed with stroboscopic neutron scattering. In summery it can be stated that the switching process in $MnWO_4$ takes place in the time scale of 2 ms to 30 ms. External parameters like the temperature of the sample, the frequency and the amplitude of the applied electric field, and the history of the sample have a big influence on the switching behaviour. Other properties are intrinsic to the sample. The maximal chiral ratios observed at different samples vary between 0.5 and 0.8.

A higher electric field yields a higher driving force, which switches the chiral ratio faster and increases the saturation value slightly. The relaxation time is independent of the applied switching frequency.

Measurements on two different samples confirm that the time scale of the switching process depends strongly on the temperature. In the vicinity of the high-temperature and the low-temperature phase transitions of the ferroelectric regime the sample can be switched faster (2 ms to 7 ms) than for intermediate temperatures (7 ms to 32 ms). For the high-temperature phase transition (second order) this is in accordance with the fact that the coercive field decreases in the vicinity of the phase transition. In the vicinity of the low-temperature phase transition (first order) the coercive field does not reduce[2]. This disagrees with the observation of a reduced relaxation time at this transition. In this context it must be pointed out that the coercive field and the time-dependent measurements were recorded on different samples.

Another feature that could be confirmed by measurements on two different samples is that the history of the sample plays a crucial role for the switching characteristics. The samples clearly develop a preferred state which depends on the field which was applied during cooling. Here it must be distinguished between a long-term and a short term-effect. The short-term effect is related to cooling in an applied electric field from the paramagnetic phase (20 K was used here) into the ferroelectric phase. The sample develops a preference to the field which was applied during cooling. This means that the relaxation time into the corresponding state is shorter than the relaxation time into the other state. By reheating the sample form the ferroelectric into the paramagnetic phase at 20 K and recooling with a reversed electric field, the direction of the preferred state can be alternated. However, the relaxation time into the non-preferred state now is much longer than it was before. The sample seems to remember the first field which was applied after cooling from room temperature. This is the long-term effect. For one sample it was tried to reset this long-term effect by heating to 120 K. However, this temperature was not sufficient to completely reset the sample.

The process of fatigue of the sample is not completely understood, yet. To

---

[2]See hysteresis loops in Reference [116].

some extent the data are perfectly reproducible, however, not all changes are reversible. During the experiment the maximal chiral ratio of the non-preferred state decreased. Heating up to 120 K did not restore the sample completely. Because of the fatigue of the sample during the two temperature series (cooling in positive/negative field) it cannot be distinguished whether the different but not completely opposite behaviour of the sample is due to the different history or due to the fatigue of the sample.

The characteristic relaxation time was determined by second harmonic generation in the group of M. Fiebig [123], too. Their results are consistent with the results presented in this thesis.

6 TbMnO₃

TbMnO$_3$ belongs to a series of rare-earth manganites with orthorhombically distorted perovskite structure, RMnO$_3$ (R = Gd, Tb, Dy) [124]. Its space group is *Pbnm* [125] with lattice constants $a = 5.3003(1)$ Å, $5.8532(1)$ Å, $c = 7.3987(1)$ Å at room temperature. Below 28 K a remarkable large spontaneous electric polarisation along the c direction develops, with $P_c \approx 600\,\mu$C/m^2 at 10 K. By applying a magnetic field of about 5 T the polarisation can be flipped in the a direction [18, 124].

There exist several older publications on the magnetic structure which however overlook the development of a cycloidal magnetic structure at lower temperatures [125–127]. The two older publications [125, 126] on the magnetic structure were published before TbMnO$_3$ was known to develop spontaneous electric polarisation. The discovery of TbMnO$_3$ being multiferroic motivated to search for more complex magnetic order which, via inversion symmetry breaking, can account for spontaneous electric polarisation. In 2005 M. Kenzelmann et al. [19] reported a transition into a spiral magnetic phase. Below 42 K the Mn moments order in a longitudinal spin-density wave (SDW) with incommensurate propagation vector $\boldsymbol{k} \approx (0, 0.28, 0)$ and moments parallel b. The propagation vector reduces slightly with temperature until a quasi-lock-in at 28 K where an elliptical cycloid with moments in the bc plane develops. The transition in the spiral phase is accompanied
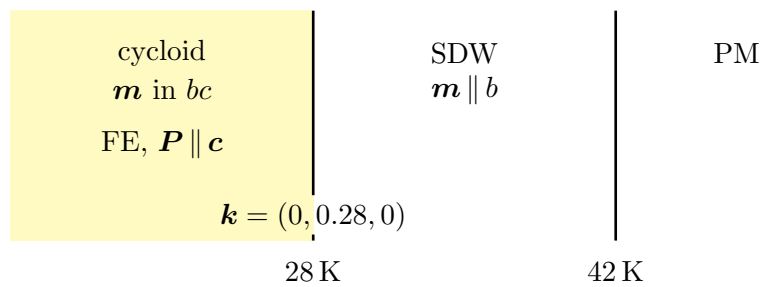

Figure 6.1: Magnetic phase diagram of TbMnO$_3$. The propagation vector reduces slightly with temperature until a quasi-lock-in at 28 K. The transition in the spiral phase is accompanied by the onset of spontaneous electric polarisation. Below 7 K the Tb moments begin to order which however has no big influence on the order of the Mn moments nor the electric polarisation. Data are taken from Reference [19].

by the onset of spontaneous electric polarisation. The inverse Dzyaloshinskii-Moriya interaction as origin of ferroelectricity in spiral magnets was unknown to Kenzelmann at that time. It was presented almost simultaneously by H. Katsura et al. [25]. The inverse Dzyaloshinskii-Moriya interaction predicts electric polarisation parallel c for a cycloidal magnetic structure in the bc plane with propagation vector along b. Below 7 K the magnetic moments of Tb begin to order which however has no big influence on the Mn order nor the electric polarisation.

Due to its high electric polarisation and the rather high transition temperatures TbMnO₃ is well suited for measurements of electric properties as well as neutron investigations in the ferroelectric phase. Furthermore, large high-quality single crystals can be grown easily with the floating-zone method. Therefore, it is not surprising that TbMnO₃ is involved in several great advances concerning the research on multiferroics. It was the first material for which the possibility of switching the electric polarisation by means of a magnetic field was reported in 2003 by T. Kimura et al. [18]. The polarisation is switched from the c direction to the a direction by a magnetic field above 5 T along the b direction. The origin of the polarisation flip was proposed to be due to a flip of the magnetic structure [128]. The experimental proof was provided 2009 by N. Aliouane et al. [129]. The rotation plane of the moments flips from bc to ab while the propagation vector remains parallel b. The opposite direction – manipulating the magnetic structure by means of electric field – is more difficult to study, as a complex antiferromagnetic order requires a microscopic technique for probing. For that reason progress in manipulating the spin helicity through an electric field during cooling below the magnetic phase transition was reported not before 2007 by Y. Yamasaki et al. [39]. One would expect that from here to direct switching at constant temperature, i.e. driving hysteresis loops, should be a small step. However, the first hysteresis loops were reported in 2009 on MnWO₄ [115, 116] and on Ni₃V₂O₈ [130]. The first hysteresis loops for TbMnO₃ are presented in this thesis. Another great advance which can be attributed to TbMnO₃ is the detection of the electromagnon [131, 132].

Within this thesis further attention was dedicated to the lock-in of the magnetic propagation vector and the behaviour of the propagation vector under the influence of isotropic pressure. The crystal structure was determined with single crystal X-ray diffraction in order to gain information on the origin of the ferroelectric polarisation.

6.1 Quasi-lock-in of the Propagation Vector

As mentioned in the introduction the magnetic propagation vector reduces slightly with temperature until a quasi-lock-in[1] where the cycloidal component of the magnetic structure develops and ferroelectricity sets in simultaneously. A precise observation of the phase transition at the *IN20* triple-axis spectrometer at the *Institut Laue-Langevin* (*ILL*) with polarised neutrons reveals that the quasi-lock-in of the incommensurability takes place at $31\,\mathrm{K}$ slightly above the development of the cycloidal phase at $28\,\mathrm{K}$ which coincides with the ferroelectric transition, Figure 6.2. The value of the propagation vector was determined by Q scans at the magnetic reflection $\boldsymbol{Q} = (2, k, 1)$ at *IN20* (*ILL*) for both spin-flip channels in the x direction at the relevant temperatures. Up to $28\,\mathrm{K}$ the intensity in both spin-flip channels is exactly the same and diverges below $28\,\mathrm{K}$.

The *absolute* value of the temperature and the reciprocal lattice position are less reliable for the following reasons: in order to apply a high electric field the pressure of the exchange gas (helium) at the sample has to be reduced. Consequently the thermal contact of the sample to the temperature sensor might be reduced. The absolute value of the temperature is therefore questionable for all measurements with electric field. For polarisation analysis *CRYOPAD* was installed on the triple-

---

[1]The term *quasi-lock-in* means the propagation vector becomes (almost) constant but stays incommensurate, in contrast to a *lock-in* where it becomes commensurate and therefore fixed to a precise value.
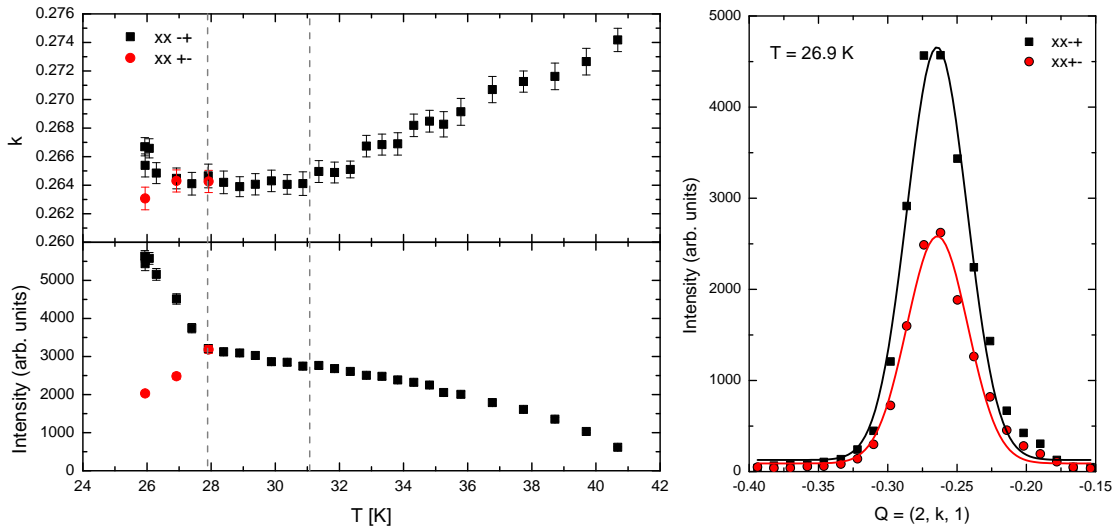

Figure 6.2: Left: The magnetic propagation vector was determined by Q scans at $\boldsymbol{Q} = (2, k, 1)$ at *IN20* (*ILL*). The quasi-lock-in takes place before the chiral component of the magnetic structure develops. Right: A Q scan at $T = 26.9\,\mathrm{K}$ with both spin-flip channels.

axis spectrometer. Unfortunately, due to the experimental setup the goniometers cannot be used for sample alignment resulting in an uncertainty of the reciprocal lattice units. A more exact determination of the absolute value of the propagation vector can be determined by a powder sample or at a four-circle diffractometer. Nevertheless relative changes in temperature and reciprocal lattice units are not affected by the mentioned limitations.

It is an unexpected and not obvious result that the propagation vector becomes constant slightly above the transition into the chiral phase. Actually, this behaviour can be seen in the results of Kenzelmann et al. [19]. However, there it remains unclear if it might be due to uncertainty in the temperature scale and it is not emphasised by the authors. A similar observation, albeit at 34 K, is reported in Reference [127]. D. Meier et al. [133] report an additional kink-like anomaly in the thermal expansion at 34 K which is suspected to be related to the slope change in the temperature dependence of the incommensurability, too.

6.2 Hysteresis

Figure 6.3: Sample holder of TbMnO₃. The electric field is applied by two aluminium plates which are fixed by four nylon screws. The sample is 0.9 mm thick.

Hysteresis loops (chiral ratio vs. electric field) were recorded at the two-axis instrument *POLI-HEIDI* at the *Forschungsreaktor München II*. The neutron polarisation and analysis is accomplished by ^{3}He-spin filters and *CRYOPAD*. The use of spin filters is accompanied by reduced neutron flux. A flipping ratio of 6 was accomplished (that corresponds to a polarisation of 70%).

Two TbMnO₃ samples which were cut from the same single crystal perpendicular to the c axis with thickness of 3.1 mm and 0.9 mm were investigated. The single crystal [ACK103] was grown by A.C. Komarek by the floating-zone method. The electric field was applied with a capacitor build from aluminium plates and nylon screws, Figure 6.3. The sample was mounted in the $(2\,0\,1)/(0\,1\,0)$ scattering plane. The strongest magnetic reflections used for determining the chiral ratio were $\boldsymbol{Q} = (2, \pm 0.28, 1)$. The intensity of the thinner sample at this reflection was rather low: 50 cts/s. The great difficulty of all measurement with electric field is to reduce the helium exchange gas to a pressure low enough to be able to apply voltage of up to 4.5 kV and still control the temperature. Much effort was made by the

POLI-HEIDI team which checked out the breakdown pressure vs. voltage curve before the experiment. The chiral ratio was determined by measuring the two spin-flip channels in the x direction, Equation (2.13).

In a preliminarily test the sample was cooled from $50\,\text{K}$ in positive and negative electric field, Figure 6.4. The sample develops a clear preference for one chiral domain depending on the sign of the electric field. This can be detected by the splitting of the spin-flip channels upon entering the chiral phase. The intensity of the two spin-flip channels is interchanged by reversing the electric field. The chiral ratio was calculated from the data for cooling in positive field. Figure 6.5 depicts the chiral ratio compared to the electric polarisation as taken from [124]. Apart from the temperature mismatch, which is due to the mentioned difficulties with the exchange gas and the resulting poor temperature control, the development of the chiral ratio resembles the development of the electric polarisation.

Reversing of chiral domains is also possible at constant temperature with varying electric field yielding hysteresis loops. The obtained hysteresis loops are shown
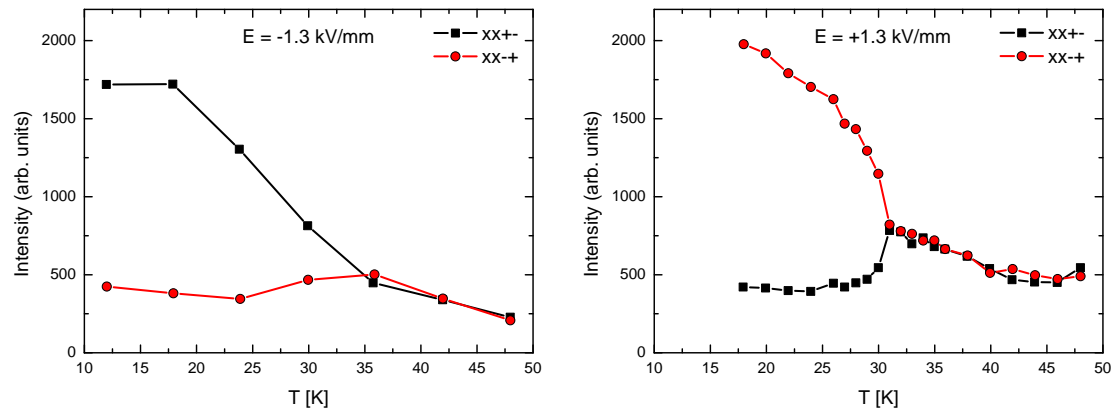

Figure 6.4: Electric field cooling of TbMnO$_3$ in $\pm 1.3\,\text{kV/mm}$. The intensities of the spin-flip channels interchange upon reversing the field which indicates the development of opposite chiral domains.
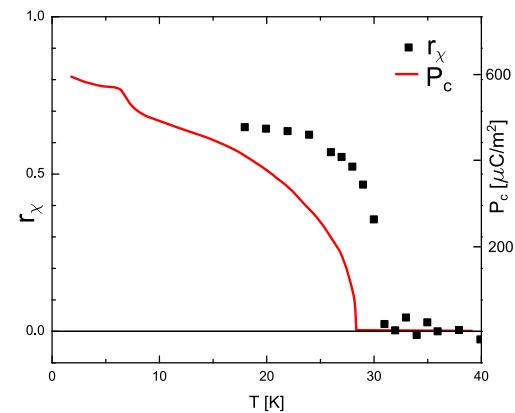

Figure 6.5: The chiral ratio calculated for $E = 1.3\,\text{kV/mm}$ compared to the electric polarisation as taken from [124]. Apart from the temperature mismatch, which is due to the mentioned difficulties with the exchange gas and the resulting poor temperature control, the development of the chiral ratio resembles the development of the electric polarisation.

in Figure 6.6. All hysteresis loops were recorded after zero-field[2] cooling from 50 K to the respective temperature. Therefore it is a remarkable result that the initial curve starts at different positive and negative values. The hysteresis loops

---

[2]To ensure there was not even a minimal electric field applied during cooling the sample was short-circuited during cooling.
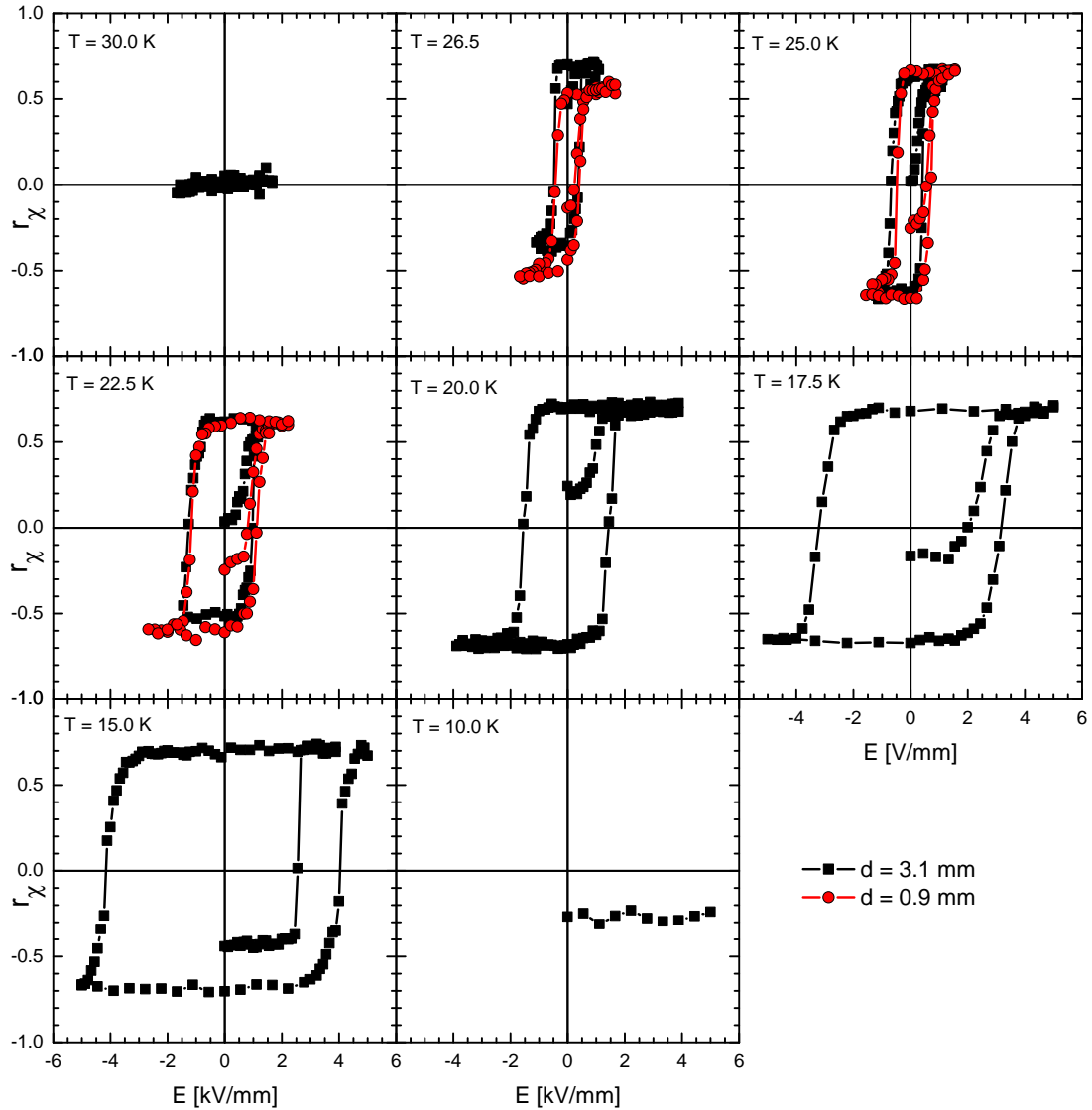

Figure 6.6: Hysteresis loop in TbMnO₃ obtained by measuring the chiral ratio as a function of external electric field at different temperatures for two different samples at *POLI-HEIDI*. The loops were recorded after zero-field cooling from 50 K. The hysteresis loops show a symmetric shape. The coercive field increases with rising temperature while the saturation value stays the same.
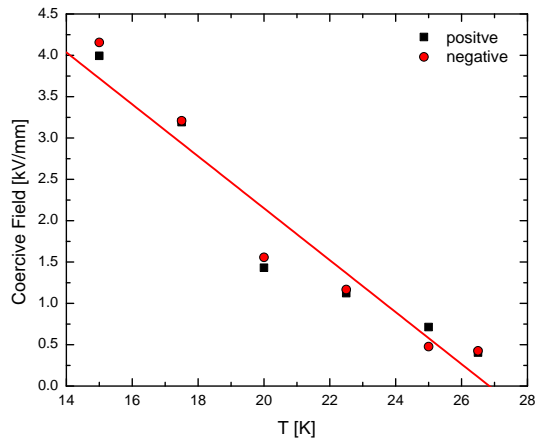
Figure 6.7: The positive and negative coercive fields match perfectly underlining the symmetric character of the sample. The coercive field follows a linear behaviour as a function of the temperature.
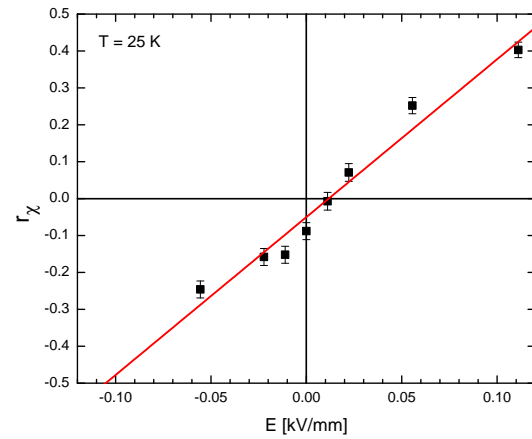
Figure 6.8: Effect of the electric field after cooling from the paramagnetic (50 K) into the chiral magnetic phase (25 K). The sequence was measured with reducing and alternating field strengths. At low fields the chiral ratio shows a linear dependence of the electric field applied during cooling.

shows a symmetric shape. Both the coercive fields and the saturation values are in good accordance. The coercive field increases with rising temperature while still the same saturation value can be reached by applying of a high enough field. The sample becomes stiffer when going deeper into the magnetic phase. This behaviour resembles the results reported on $MnWO_4$, compare [116]. At 10 K the sample is so stiff that the electric field causes an electrical breakdown before the chiral ratio can be affected. The hysteresis loops of the two samples of different thickness match perfectly. In order to apply the same electric field to the thicker sample a larger voltage has to be applied. For that reason it is not possible to reach as high fields for the thicker sample as for the thinner sample. Hence there are only three hysteresis loops at higher temperatures for the sample which was 3.1 mm thick.

The coercive fields for all temperatures are investigated in Figure 6.7. The positive and negative coercive fields match perfectly underlining the symmetric character of the sample. The coercive field shows more or less a linear dependence of the temperature.

The effect of the electric field when cooling from the paramagnetic into the chiral magnetic phase is depicted in Figure 6.8. The sample was cooled from 50 K to 25 K in small electric fields. The sequence was measured with reducing and alternating field strengths. Very small fields are sufficient when applied during cooling to produce a preference for one chiral domain. Saturation is not reached for very small fields. Instead the chiral ratio shows a linear dependence of the electric field at low values.

6.3 Pressure

The highly frustrated, complex magnetic structure of TbMnO$_3$ arises from competing ferromagnetic and antiferromagnetic exchange interactions. Pressure affects the interatomic distances and therefore influences the frustration. The effect of hydrostatic pressure up to 15 kbar on the magnetic structure in TbMnO$_3$ was investigated at *D10* (*ILL*) four-circle diffractometer. The pressure was applied with a high-pressure clamped cell [04PCL150CB5] [134]. For increasing the pressure the cell with the crystal inside had to be dismounted. The pressure was applied at room temperature. After that the pressure cell was reinstalled on the diffractometer and the temperature was set to 10 K. It has to be mentioned that during cooling the cell loses pressure.

The value of the incommensurability was determined at the reflections $(0, \pm k, \pm 1)$, $(0, \pm 1 \pm k, \pm 1)$ and $(0, \pm 2 \pm k, \pm 1)$ (20 reflections) by longitudinal Q-scans. The crystal was mounted in the $(0\,1\,0)/(0\,0\,1)$ plane. The orientation matrix was determined by the automatic routine at *D10*. For any magnetic reflection both satellites $\boldsymbol{k}_1 = \boldsymbol{k}$ and $\boldsymbol{k}_2 = -\boldsymbol{k}$ were collected. The exact value of $\boldsymbol{k}$ was calculated by this formula: $\boldsymbol{k} = (\boldsymbol{k}_1 - \boldsymbol{k}_2)/2$. It turned out that the best signal was obtained from the $(0, \pm k, \pm 1)$ reflections. The mean values of the incommensurability as a function of temperature at different pressures are shown in Figure 6.9. In the low temperature phase the value of the incommensurability is almost constant. These values are shown in Figure 6.10. Omitting the point at 0.36 kbar a linear function can be fitted to the data. The pressure which was applied at room temperature decreases at low temperature. The nominal pressure of 3.16 kbar at room temperature reduced to almost 0 kbar at 10 K. The data were
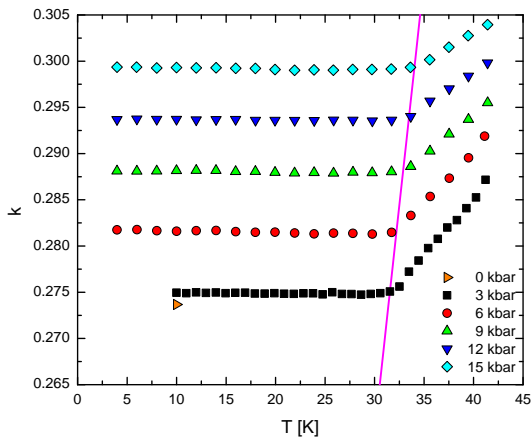

Figure 6.9: Incommensurability as function of temperature at different pressures. The pink line indicates the quasi-lock-in at T_{lock}.
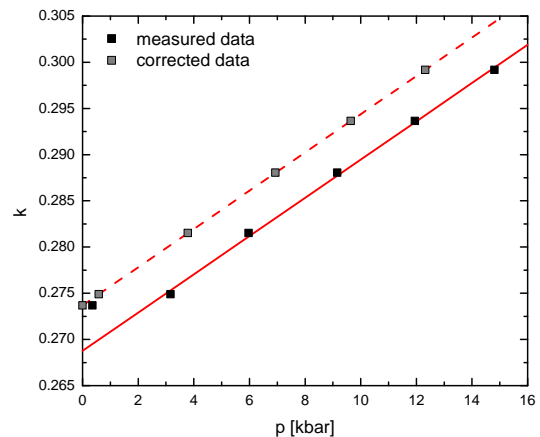
Figure 6.10: Incommensurability in the low temperature phase as function pressure.
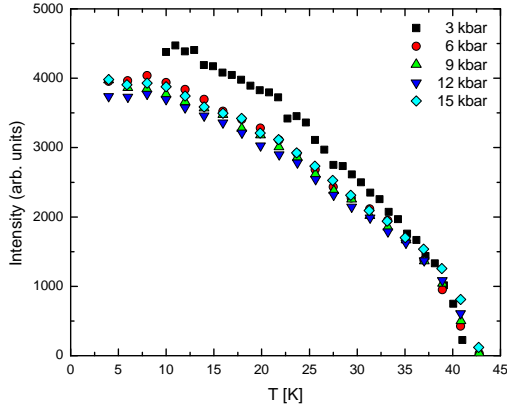
Figure 6.11: Intensity of the magnetic Bragg reflection $(0, 0.28, 1)$ at different pressures. The Néel temperature does not depend on the pressure.

shifted accordingly (dashed line, grey symbols). This rather crude correction is justified by the fact that the zero pressure value of the incommensurability agrees with the values of prior investigations: $k = 0.27$ [19], $k = 0.275$ [125], $k = 0.28$ [127], and $k = 0.275$ from another measurement at *1T1* at the *Laboratoire Léon Brillouin*. The incommensurability k as function of pressure p in kbar (including the shift) is as follows:

$$k(p) = 0.2737(1)\,\text{r.l.u.} + 0.00207(4)\,p\,\frac{\text{r.l.u.}}{\text{kbar}}$$

The values of the corrected pressure are shown in the table:

p at RT [kbar]	0.36	3.16	5.97	9.16	11.95	14.81
p at low T [kbar]	0.00	0.58	3.78	6.94	9.64	12.32

The magnetic phase transition is defined by two characteristic temperatures. At $T_{\text{FE}} = 28\,\text{K}$ ferroelectricity sets in. Above T_{FE} the structure is sinusoidally ordered with the magnetic moment along b. Below T_{FE} the magnetic structure transforms into an elliptical spiral with moments in the bc plane. The quasi-lock-in of the incommensurability sets in at $T_{\text{lock}} = 31.5\,\text{K}$ for zero pressure, see Figure 6.9. This is in perfect agreement with [19]. T_{lock} is indicated as pink line in Figure 6.9 and increases slightly with increasing pressure:

$$T_{\text{lock}} = 31.5(2)\,\text{K} + 0.21(3)\,p\,\frac{\text{K}}{\text{kbar}}$$

The Néel temperature T_{N} shows no temperature dependence as can be seen in Figure 6.11.

The complex magnetic structure in $TbMnO_3$ is a consequence of competing ferromagnetic and antiferromagnetic exchange interactions between the magnetic moments of the manganese ions. In the ab plane the nearest neighbours interact
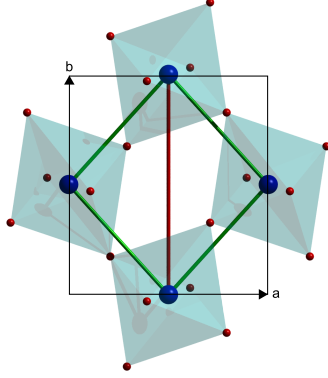
Figure 6.12: View on the ab plane of TbMnO₃. Ferromagnetic interactions J_F between nearest neighbours are highlighted in green. Antiferromagnetic interactions J_AF between next-nearest neighbours along b are highlighted in red.
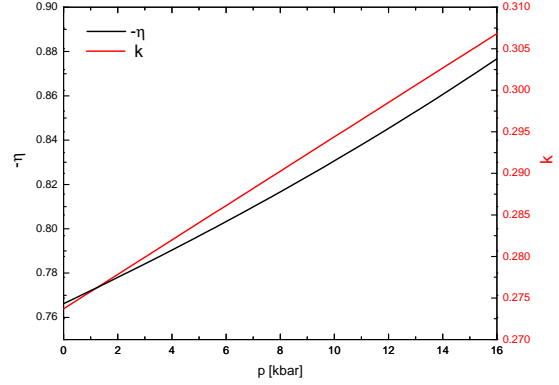
Figure 6.13: $-\eta = -J_\mathrm{AF}/J_\mathrm{F}$ as function of the pressure. Pressure enhances the J_AF compared to J_F.

via a ferromagnetic interaction $J_\mathrm{F} > 0$ and the next-nearest neighbours along b via an antiferromagnetic interaction $J_\mathrm{AF} < 0$. Along c nearest neighbours interact via an antiferromagnetic interaction $J_{\mathrm{AF}c} < 0$ [135]. The situation is illustrated in Figure 6.12. The magnetic structure is a cycloid with moments in the bc plane [19]. Neglecting the elliptical shape of the cycloid the magnetic moments can be described by

$$\boldsymbol{S} = S[0,\ \cos(2\pi\,ky),\ \sin(2\pi\,ky)]$$

where k is the y component of the propagation vector $\boldsymbol{k} = (0, k, 0)$ and y the fractional position of the moment. The magnetic energy of the moment distribution is given by

$$E = -\sum_{i,j} J_{i,j}\boldsymbol{S}_i \cdot \boldsymbol{S}_j$$

Each ion has two neighbours in c direction, two next-nearest neighbours in b direction and four nearest neighbours in the ab plane. The magnetic energy per ion is thus

$$\epsilon = -4J_\mathrm{F}S^2 \cos(\pi\,k) - 2J_\mathrm{AF}S^2 \cos(2\pi\,k) - 2J_{\mathrm{AF}c}S^2$$

In the ground state the system minimises its energy. The competition between the ferromagnetic and antiferromagnetic exchange interactions results in a modi-

fication of the incommensurability k as function of $\eta = J_{\mathrm{AF}}/J_{\mathrm{F}}$.

$$\frac{\mathrm{d}\epsilon}{\mathrm{d}k} = 4\pi\, J_{\mathrm{F}}S^2\sin(\pi\,k) + 4\pi\, J_{\mathrm{AF}}S^2\sin(2\pi\,k)$$
$$\implies \quad 0 = \sin(\pi\,k) + \eta\sin(2\pi\,k)$$
$$\implies \quad \eta = -\frac{1}{2\cos(\pi\,k)}$$

For $k = 0.28$ the relation between J_{AF} and J_{F} is $\eta = J_{\mathrm{AF}}/J_{\mathrm{F}} = -0.78$ and for $k = 0.30$ it is $\eta = -0.85$. The function $-\eta$ is plotted as function of the pressure in Figure 6.13. In conclusion, applying pressure to TbMnO$_3$ enhances the antiferromagnetic next-nearest-neighbour exchange interaction J_{AF} compared to the ferromagnetic nearest-neighbour exchange interaction J_{F}.

6.4 X-Ray Crystal-Structure Analysis

It has been shown that the ferroelectric polarisation in TbMnO$_3$ arises from the inverse Dzyaloshinskii-Moriya interaction. It remains however unclear whether the polarisation is of electronic or of ionic character. By X-ray diffraction, the position of the electron cloud regardless if the electron cloud is shifted with respect to the atomic nucleus (electronic character) or if the ion is shifted as a whole (ionic character), can be studied.

The space group of TbMnO$_3$ is *Pbnm* which is a centrosymmetric space group and therefore electric polarisation is forbidden. In the ferroelectric phase the symmetry must therefore reduce to a non-centrosymmetric space group. There exist four maximal non-isomorphic subgroups: *Pbn*2$_1$, *Pb*2$_1$*m*, *P*2$_1$*nm*, *P*2$_1$2$_1$2$_1$ [136]. Only *Pbn*2$_1$ allows electric polarisation along c. An X-ray measurement is able to detect the deviations of the electrons from their centrosymmetric position. However, these deviations will be small and it is not clear if the resolution will be sufficient.

A room temperature single-crystal X-ray measurement was performed with a *Bruker X8 APEX* using Mo $K\alpha_1$ radiation. A spherical sample with a diameter of 75 µm to 80 µm was produced with a ball mill and glued on a glass capillary with clear nail varnish diluted by acetone. A dataset was collected within 24 h. 12 744 reflections were collected of which 1369 were independent. The internal (weighted) R value was 2.0% (2.2%). The data were corrected for spherical absorption. The structure refinement was done with *Jana2006* [137]. The refinement was performed for F^2 with isotropic extinction correction and anisotropic temperature parameters in the space group *Pbnm*. The lattice parameters are $a = 5.3003(1)$ Å, $5.8532(1)$ Å, and $c = 7.3987(1)$ Å. The structural parameters and the R values are listed in Table 6.1. The parameters are in good agreement with the parameters in Reference [125].

Note, refining the room temperature data in the non-centrosymmetric space group $Pbn2_1$ should not give rise to an electric polarisation due to the deviation of the ions from the centrosymmetric positions. The results of the refinement in $Pbn2_1$ are listed in Table 6.2. The z component of Tb was fixed to account for the floating origin.

The electric dipole moment of a crystal can be calculated by

$$\boldsymbol{p} = \sum_\alpha q_\alpha \Delta \boldsymbol{r}_\alpha$$

where $\Delta \boldsymbol{r}$ is the deviation of an ionic position from its centrosymmetric position and q is its charge. The polarisation $\boldsymbol{P} = \boldsymbol{p}/V$ is defined as dipole moment per volume V.

With the data from Table 6.1 and 6.2 the polarisation of $\text{Tb}^{3+}\text{Mn}^{3+}\text{O}_3^{2-}$ can be computed: $P_c = 4.2(2) \cdot 10^4 \, \text{µC/m}^2$. This value exceeds the actual polarisation by a factor of 70 and was determined in the paraelectric phase. This result demonstrates the precision of this X-ray measurement is not sufficient to detect the transition to a ferroelectric space group. In general X-ray measurements are less precise for lighter elements as oxygen. Unfortunately the light oxygen ions are expected to experience the highest deviation from their centrosymmetric positions. The expected deviation of the oxygen ions can be estimated. In a simple model only the oxygen ions shift while the other ions remain at the centrosymmetric position. There are twelve O^{2-} ions in the unit cell. This gives $\Delta r_c = P_c V / (12 \cdot 2\,e) = 0.000\,36 \, \text{Å}$ which corresponds to a shift in the fractional position parameters of $\Delta z = 0.000\,05$. This resolution is not reached for the oxygen ions.

Because the room temperature measurement did not yield the required resolution it was abstained from making a measurement in the ferroelectric phase at low temperature.

atom	x	y	z	U_{iso} [Å^2]			
Tb	0.98349(2)	0.08138(2)	1/4	0.00342(3)			
Mn	1/2	0	0	0.00317(7)	GOF	=	1.54
O1	0.1072(4)	0.4660(3)	1/4	0.0047(4)	R	=	1.81 %
O2	0.7036(3)	0.3272(2)	0.05145(17)	0.0048(2)	R_w^2	=	4.83 %

atom	$U11$	$U22$	$U33$	$U12$	$U13$	$U23$
Tb	0.00373(5)	0.00320(5)	0.00332(5)	−0.00058(3)	0	0
Mn	0.00279(13)	0.00438(13)	0.00234(13)	0.00095(9)	0.00001(8)	0.00070(10)
O1	0.0054(7)	0.0062(6)	0.0025(6)	−0.0010(5)	0	0
O2	0.0044(4)	0.0050(4)	0.0050(4)	−0.0012(3)	0.0010(3)	−0.0007(3)

Table 6.1: Structural parameters of TbMnO$_3$ at room temperature as measured at *APEX*. The refinement was done with *Jana2006* in space group *Pbnm*. Anisotropic temperature factors were used.

atom	x	y	z	U_{iso} [Å^2]			
Tb	0.983484(17)	0.081438(15)	1/4	0.00343(2)			
Mn	0.4977(3)	−0.00444(16)	−0.00090(14)	0.00282(6)	GOF	=	1.29
O1	0.1069(3)	0.4660(3)	0.2533(8)	0.0045(3)	R	=	1.87 %
O2A	0.7049(10)	0.3283(5)	0.0547(6)	0.0060(8)	R_w^2	=	4.43 %
O2B	0.7028(9)	0.3262(6)	0.4508(5)	0.0036(7)			

atom	$U11$	$U22$	$U33$	$U12$	$U13$	$U23$
Tb	0.00371(4)	0.00324(4)	0.00335(4)	−0.00058(2)	0.0009(2)	−0.00008(9)
Mn	0.00259(10)	0.00372(11)	0.00217(10)	0.00065(8)	0.00004(7)	0.00048(8)
O1	0.0039(13)	0.0021(14)	0.0120(14)	−0.0003(10)	0.0025(11)	0.0004(9)
O2A	0.0048(13)	0.0076(15)	−0.0014(9)	−0.0022(10)	0.0002(9)	0.0019(8)
O2B	0.0048(13)	0.0076(15)	−0.0014(9)	−0.0022(10)	0.0002(9)	0.0019(8)

Table 6.2: Structural parameters of TbMnO$_3$ at room temperature as measured at *APEX*. The refinement was done with *Jana2006* in space group *Pbn2$_1$*. Anisotropic temperature factors were used.

6.5 Conclusion

In this chapter magnetoelectric hysteresis loops in TbMnO$_3$ were presented. They were recorded by determining the chiral ratio with polarised neutrons. By the use of two samples of different thickness it was demonstrated that the hysteresis scales with the strength of the electric field. The coercive field increases linearly with decreasing temperature. When cooling from the paramagnetic regime only a small field is required for choosing a preferred chirality. The value of the chiral ratio depends linearly on the electric field strength for small fields. Further it has been demonstrated that the development of the chiral ratio resembles the development of the electric polarisation.

The quasi-lock-in of the magnetic propagation vector was investigated with polarised neutrons. It has been shown that the lock-in takes place slightly above the transition into the chiral magnetic phase. The propagation vector changes linearly with isotropic pressure. This is due to the highly frustrated and thus complex magnetic structure. The increase of the value of the incommensurability indicates that the antiferromagnetic exchange interaction is enhanced with respect to the ferromagnetic exchange interaction.

A precise X-ray single crystal measurement was performed. The measurement yields good results. Nevertheless it is not accurate enough to analyse the origin of the ferroelectric polarisation. Otherwise, such measurements have not yet been reported in literature.

7 DyMnO₃

The structural, ferroelectric, and magnetic properties of DyMnO$_3$ resemble those of TbMnO$_3$. Its space group is *Pbnm* with lattice constants $a = 5.2841\,\text{Å}$, $b = 5.8496\,\text{Å}$, $c = 7.3941\,\text{Å}$ [138]. DyMnO$_3$ exhibits the largest ferroelectric polarisation among the rare-earth manganites. Spontaneous ferroelectric polarisation develops below $18\,\text{K}$ parallel to the c direction and reaches $P_c \approx 1400\,\mu\text{C/m}^2$ at its maximum at $12\,\text{K}$. Below $12\,\text{K}$ the spontaneous polarisations decreases until $6.5\,\text{K}$ where it becomes constant at $600\,\mu\text{C/m}^2$ similar to the polarisation of TbMnO$_3$. By application of a magnetic field along the b direction the electric polarisation can be flipped into the a direction and values of $P_a \approx 2500\,\mu\text{C/m}^2$ can be reached in relatively low magnetic fields of $2\,\text{T}$. [124].

The magnetic structure of the Mn moments is similar to the structure in TbMnO$_3$. Below $39\,\text{K}$ the Mn moments order in an incommensurate longitudinal spin-density wave with moments along b. The propagation vector $\boldsymbol{k} = (0, 0.37, 0)$ reduces slightly until a quasi lock-in at $18\,\text{K}$ where a second transition into a cycloidal phase with moments in the bc plane occurs. An essential difference compared to TbMnO$_3$ plays the role of the Dy moments. While in TbMnO$_3$ the ordering of the Tb moments has no big influence on the electric polarisation, the order of the Dy moments can account for the significant higher polar-
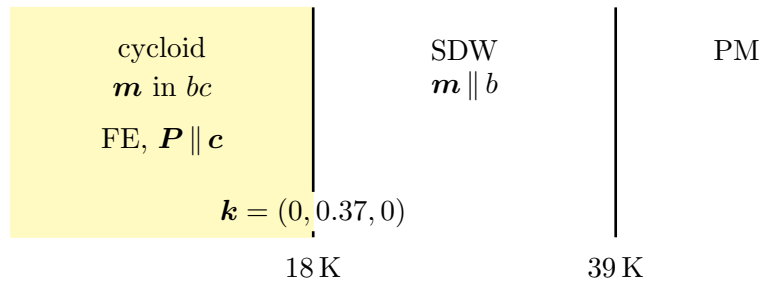

Figure 7.1: Magnetic phase diagram of DyMnO$_3$. The propagation vector reduces slightly with temperature until a quasi-lock-in at $18\,\text{K}$ takes place. The transition in the spiral phase is accompanied by the onset of spontaneous electric polarisation. Below $15\,\text{K}$ the Dy moments order with the same propagation vector as the Mn moments and thereby enhance the electric polarisation. Below $6.5\,\text{K}$ the Dy moments order with propagation vector $\boldsymbol{k}_{\text{Dy}} = (0, \frac{1}{2}, 0)$ accompanied by the steep drop of the electric polarisation. Data are taken from Reference [28].

isation and its steep drop below 12 K. Below 15 K the Dy moments order along the b axis in an incommensurate sinusoidal structure with the same propagation vector as the Mn moments and thereby enhance the electric polarisation. Below 6.5 K the Dy moments order in a commensurate structure with propagation vector $\boldsymbol{k}_{\mathrm{Dy}} = (0, \frac{1}{2}, 0)$ accompanied by the steep drop of the electric polarisation. [28, 139]

Neutron-scattering experiments on Dy compounds suffer from the large neutron absorption cross section of Dy which can be minimised by the use of the isotope ^{162}Dy.

For DyMnO₃ the magnetoelectric hysteresis was investigated in the same manner as reported in the previous chapter for TbMnO₃. The measurements were performed at the two-axis instrument *POLI-HEIDI* at the *Forschungsreaktor München II*.

7.1 Hysteresis

Hysteresis loops (chiral ratio vs. electric field) of DyMnO₃ were recorded during the same beam time in which hysteresis loops of TbMnO₃ were recorded at *POLI-HEIDI*. For further description on the experimental setup, it is referred to Section 6.2.

A DyMnO₃ sample was cut perpendicular to the c axis with a thickness of 2.6 mm. The electric field was applied with a capacitor build from aluminium plates and nylon screws. The sample was mounted in the $(2\,0\,1)/(0\,1\,0)$ scattering plane. The strongest magnetic reflection used for the measurement was $\boldsymbol{Q} = (-2, 0.37, -1)$. The chiral ratio was determined by measuring the two spin-flip channels in the x direction, Equation (2.13).
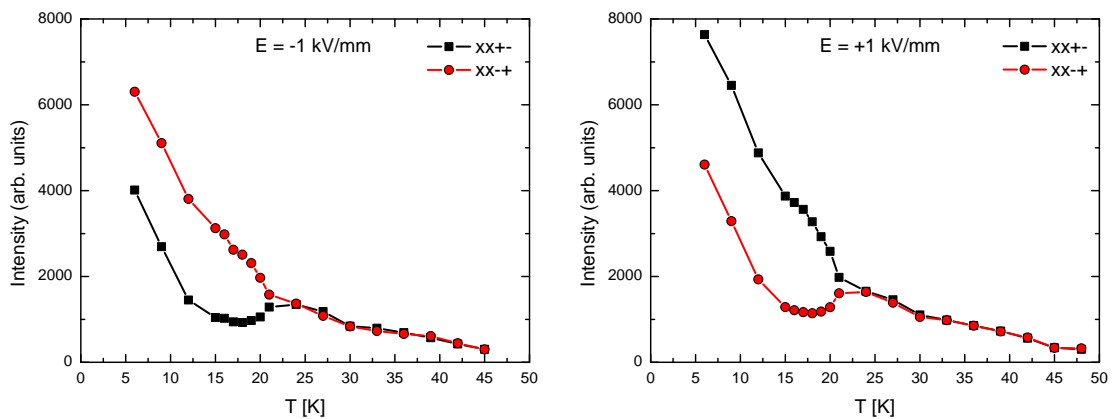

Figure 7.2: Electric field cooling of DyMnO₃ in ± 1 kV/mm. The intensities of the spin-flip channels interchange upon reversing the field which indicates the development of opposite chiral domains.
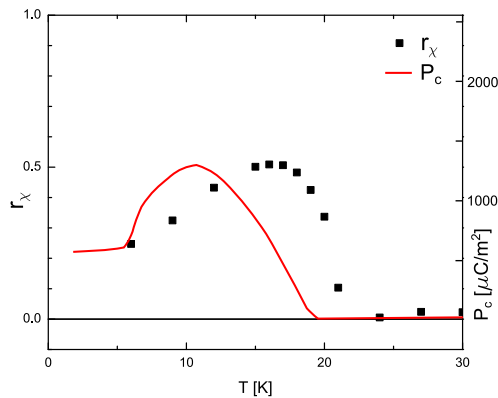
Figure 7.3: The chiral ratio compared to the electric polarisation as taken from [124]. Apart from the temperature mismatch the development of the chiral ratio resembles the development of the electric polarisation.

Again, during electric field cooling from 50 K the two spin-flip channels were recorded, Figure 7.2. The sample develops a clear preference for one chiral domain depending on the sign of the electric field. This can be detected by the splitting of the spin-flip channels upon entering the chiral phase. The intensity of the two
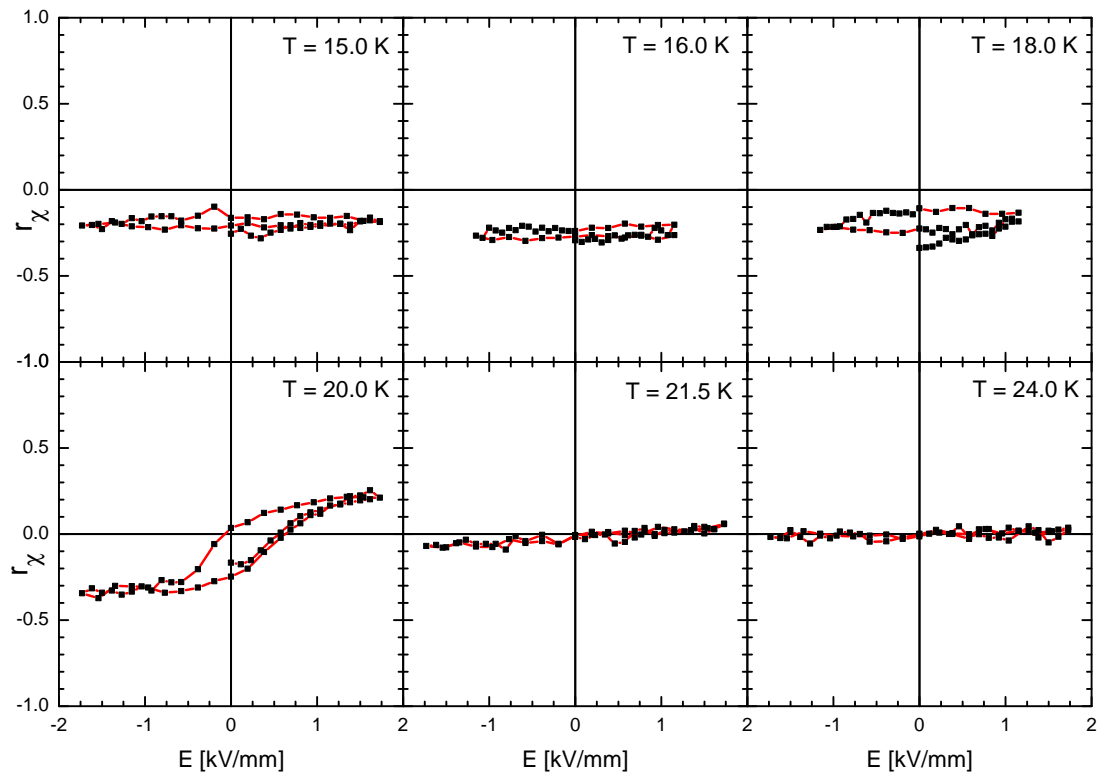

Figure 7.4: Hysteresis loops in DyMnO$_3$ obtained by measuring the chiral ratio as a function of external electric field at different temperatures for two samples at *POLI-HEIDI*. The loops were recorded after zero-field cooling from 50 K. Reversing of chiral domains is only possible near the ferroelectric transition.

119

spin-flip channels is interchanged by reversing the electric field. In contrast to TbMnO$_3$ (Figure 6.4), where the difference in both spin-flip channels increases upon cooling, in DyMnO$_3$ the difference reaches a maximum around 17 K, reduces thereafter, and becomes almost constant at lower temperatures. This behaviour can be understood by considering the chiral ratio calculated from the field-cooling data. In Figure 7.3 the chiral ratio is compared to the electric polarisation as taken from [124]. Apart from the temperature mismatch the development of the chiral ratio resembles the development of the electric polarisation qualitatively.

Reversing of chiral domains at constant temperature by means of an applied electric field in DyMnO$_3$ is only possible close to the phase transition of the chiral magnetic phase. The recorded hysteresis loops are shown in Figure 7.4. All hysteresis loops were recorded after zero-field cooling from 50 K to the respective temperature. To ensure there was not even a minimal electric field applied during cooling the sample was short-circuited during cooling. According to literature the ferroelectric transition should be at 18 K. The observation of a hysteresis loop at 20 K indicates a problem with the temperature control that might be explained by the low pressure of the exchange gas (helium). The low pressure is required in order to apply the electric field yet it results in a poor temperature control.

7.2 Conclusion

The experimental results clearly demonstrated that the development of the chiral ratio resembles the development of the electric polarisation. Furthermore, the difficulty of driving hysteresis loops in DyMnO$_3$ compared to TbMnO$_3$ was observed. In fact just one hysteresis loop close to the ferroelectric transition could be recorded. One explanation might be that the Dy order is the reason for the poor response of the chiral ratio of the Mn moments to the electric field. In DyMnO$_3$ the order of the Dy moments has big influence on the ferroelectric polarisation.

8 YMn$_2$O$_5$

Oxides of the RMn$_2$O$_5$ (R = Y, Bi or rare earth) series exhibit large electric polarisation. Spontaneous electric polarisation along the b axis develops in YMn$_2$O$_5$ below 39 K and values of 1000 µC/m^2 are reached. The sign of the electric polarisation inverts at 19 K and its absolute value drops to a quarter of the former value [140]. Ferroelectricity is induced by the order of the magnetic moments of the Mn$^{3+/4+}$ ions. Below 45 K commensurate magnetic order with propagation vector $\boldsymbol{k} = (1/2, 0, 1/4)$ sets in. Between 23 K and 17 K a transition to an incommensurate order with propagation vector $\boldsymbol{k} = (0.48, 0, 0.29)$ occurs [35].

L. Chapon et al. [35] propose a superposition of two sinusoidal spin-density waves on different crystallographic Mn sites in the commensurate phase on basis of neutron powder diffraction. This resulting magnetic structure breaks inversion symmetry. The electric polarisation is claimed to arise from exchange striction. More recent results obtained by neutron single-crystal diffraction by H. Kimura et al. [34] and C. Vecchini et al. [141] report an additional small cycloidal component in the magnetic structure. It is therefore questionable whether the predominant mechanism inducing ferroelectricity is the inverse Dzyaloshinskii-Moriya interaction or exchange striction.

Although much attention has been devoted to the determination of the magnetic structure of YMn$_2$O$_5$ little effort has been put to measuring the lattice distortions that give rise to the electric polarisation. This information could be a valuable hint on that matter. This displacement will be small, however.

In the context of this thesis detailed crystallographic investigations of the crystal structure were undertaken. A room temperature single-crystal X-ray diffraction measurement was performed with a *Bruker X8 APEX* using Mo $K\alpha_1$ radiation. A spherical sample with a diameter of 115(10) µm was produced with a ball mill and glued on a glass capillary with clear nail varnish diluted by acetone. A dataset was collected within 24 h. 32 396 reflections were collected of which 1979 were independent. The internal (weighted) R value was 5.4% (2.9%). The data was corrected for spherical absorption. The structure refinement was done with *Jana2006* [137]. The refinement was performed for $|F|^2$ with isotropic extinction correction and anisotropic temperature parameters in the space group *Pbam*. The lattice parameters are $a = 5.6639(2)$ Å, $b = 7.2587(2)$ Å, and $c = 8.4726(3)$ Å. The structural parameters and the R values are listed in Table 8.1. The parameters are in excellent agreement with parameters from References [34, 142].

The space group of YMn$_2$O$_5$ is *Pbam* [143] which is a centrosymmetric space

group and therefore electric polarisation is forbidden. In the ferroelectric phase the symmetry must therefore reduce to a non-centrosymmetric space group. There exist four maximal non-isomorphic subgroups: *Pba*2, *Pb*2$_1$*m*, *P*2$_1$*am*, *P*2$_1$2$_1$2 [136]. Only *Pb*2$_1$*m* allows for electric polarisation along *b*.

The electric dipole moment of a crystal can be calculated by

$$\boldsymbol{p} = \sum_\alpha q_\alpha \Delta \boldsymbol{r}_\alpha$$

where $\Delta \boldsymbol{r}$ is the deviation of an ionic position from its centrosymmetric position and q is its charge. The polarisation $\boldsymbol{P} = \boldsymbol{p}/V$ is defined as dipole moment per volume V. A simple model can be used to estimate the expected displacement. In a simple model all oxygen ions shift equally while the other ions remain at the centrosymmetric position. There are 20 O^{2-} ions in the unit cell. The expected displacement of the oxygen ions under this assumption amounts to $\Delta r_b = P_b V/(20 \cdot 2\,e) = 0.000\,54\,\text{Å}$ which corresponds to a shift in the fractional position parameters of $\Delta y = 0.000\,06$.

Note, refining the room temperature data in the non-centrosymmetric space group *Pb*2$_1$*m* should not give rise to an electric polarisation due to the deviation of the ions from the centrosymmetric positions. The results of the refinement in *Pb*2$_1$*m* are listed in Table 8.2. The y component of Mn1 was fixed to account for the floating origin.

With the data from Table 8.1 and 8.2 the polarisation of Y^{3+}Mn$_2^{3+/4+}$O$_5^{2-}$ (Mn1: +4, Mn2: +3) can be computed: $P_b = 8.1(1.5) \cdot 10^3\,\text{µC/m}^2$. This value is a factor 8 higher than the actual polarisation and was computed for the paraelectric phase where there should be no polarisation. This result demonstrates the precision of this X-ray diffraction measurement is not sufficient to detect the transition to a ferroelectric space group. In general X-ray diffraction measurements are less precise for lighter elements as oxygen. Unfortunately the light oxygen ions are expected to experience the highest deviation from their centrosymmetric positions. The necessary resolution for the oxygen ions of $\Delta y = 0.000\,06$ was not reached what can be detected from the values in Table 8.2 directly.

Despite the non-sufficient resolution at room temperature another data set was collected at $T = 28\,\text{K}$. The crystal was cooled to $28\,\text{K}$ by a stream of helium gas which is cooled by passing through a heat exchanger *N-HeliX* by *Oxford Cryosystems*. The cold gas passes over the sample through an X-ray transparent beryllium nozzle.

A dataset was collected within 8 h. 8296 reflections were collected of which 1993 were independent. The internal (weighted) R value was 4.0% (2.3%). The data were corrected for spherical absorption. The structure refinement was done with *Jana2006* [137]. The refinement was performed for $|F|^2$ with isotropic extinction correction and anisotropic temperature parameters in the space groups *Pbam* and *Pb*2$_1$*m*. The lattice parameters are $a = 5.6622(4)\,\text{Å}$, $b = 7.2516(5)\,\text{Å}$,

and $c = 8.4660(5)$ Å. The structural parameters and the R values are listed in Table 8.3 and 8.4. The electric polarisation computed from that data amounts to $P_b = 1.8(2) \cdot 10^4\,\mu\mathrm{C/m^2}$. This is a factor 18 higher than the actual value. Again, the necessary resolution for the oxygen ions could not be accomplished.

Overall, the structure refinements of YMn_2O_5 at room temperature and at 28 K yield good R values for the space group *Pbam*. The values at 28 K are only slightly worse, which is due to the three times shorter measurement time. At low temperatures ice accumulates around the sample holder. The measurement time has to be reduced in order to reduce the risk that the ice covers the sample. The evaluation of the data in space group $Pb2_1m$ does not improve the R values of the refinement which indicates that the data can be described sufficiently well with the high symmetry space group. The experiment did not achieve to analyse the shifts of the ions into a polar position. Measurements of this precision however are at the threshold of the experimental resolution. Reference [140] reports a synchrotron diffraction measurement and a neutron diffraction measurement was reported in the diploma thesis [97]. Both measurements meant to analyse the ferroelectric phase transition by a precise structure analysis. Neither of them yielded sufficient resolution. Concluding, ferroelectric polarisation in YMn_2O_5 is beyond the resolution of structure analysis.

atom	x	y	z	U_{iso} [Å^2]			
Y	0.138697(18)	0.171131(18)	0	0.00493(3)			
Mn1	0	1/2	0.25494(3)	0.00404(4)	GOF	=	1.20
Mn2	0.41180(3)	0.35004(3)	1/2	0.00450(4)	R	=	1.91 %
O1	0	0	0.27114(18)	0.0060(2)	R_w^2	=	4.02 %
O2	0.16317(14)	0.44412(14)	0	0.0056(2)			
O3	0.15109(14)	0.43087(15)	1/2	0.0073(2)			
O4	0.39454(11)	0.20593(10)	0.24333(13)	0.00640(15)			

atom	$U11$	$U22$	$U33$	$U12$	$U13$	$U23$
Y	0.00528(4)	0.00391(6)	0.00559(4)	0.00001(4)	0	0
Mn1	0.00439(6)	0.00355(8)	0.00419(6)	0.00015(5)	0	0
Mn2	0.00514(6)	0.00379(8)	0.00458(6)	−0.00015(5)	0	0
O1	0.0076(3)	0.0049(4)	0.0055(3)	0.0012(3)	0	0
O2	0.0056(3)	0.0054(4)	0.0059(3)	0.0005(3)	0	0
O3	0.0057(3)	0.0106(5)	0.0055(3)	0.0020(3)	0	0
O4	0.0083(2)	0.0043(3)	0.0066(2)	0.0012(2)	−0.00096(18)	−0.00109(19)

Table 8.1: Structural parameters of YMn₂O₅ at RT in space group *Pbam*.

atom	x	y	z	U_{iso} [Å^2]			
YA	0.13846(8)	0.17096(3)	0	0.00445(9)			
YB	0.63893(8)	0.32860(4)	0	0.00534(10)			
Mn1	−0.00015(13)	1/2	0.25495(3)	0.00402(3)			
Mn2A	0.41204(12)	0.35036(8)	1/2	0.00465(15)	GOF	=	1.13
Mn2B	0.91158(12)	0.15029(9)	1/2	0.00430(14)	R	=	2.13 %
O1	−0.0007(5)	0.0007(4)	0.27121(15)	0.00594(18)	R_w^2	=	4.23 %
O2A	0.1637(4)	0.4449(5)	0	0.0059(6)			
O2B	0.6626(4)	0.0565(4)	0	0.0052(6)			
O3A	0.1521(5)	0.4305(5)	1/2	0.0074(7)			
O3B	0.6500(5)	0.0687(5)	1/2	0.0073(7)			
O4A	0.3946(4)	0.2069(3)	0.2436(4)	0.0066(5)			
O4B	0.8944(4)	0.2949(3)	0.7570(4)	0.0060(5)			

atom	$U11$	$U22$	$U33$	$U12$	$U13$	$U23$
YA	0.004901(15)	0.0031(2)	0.00533(13)	0.00027(14)	0	0
YB	0.00553(15)	0.0047(2)	0.00574(14)	0.00033(14)	0	0
Mn1	0.00433(5)	0.00361(7)	0.00412(5)	0.00014(4)	0.00015(14)	0.00025(18)
Mn2A	0.0051(2)	0.0043(3)	0.0046(2)	0.0000(2)	0	0
Mn2B	0.0051(2)	0.0033(3)	0.0044(2)	0.0004(2)	0	0
O1	0.0076(3)	0.0047(4)	0.0055(3)	0.0012(2)	0.0006(7)	0.0007(8)
O2A	0.0034(10)	0.0080(14)	0.0062(9)	−0.0004(8)	0	0
O2B	0.0078(11)	0.0024(12)	0.0055(8)	−0.0018(8)	0	0
O3A	0.0068(11)	0.0095(14)	0.0059(9)	0.0029(10)	0	0
O3B	0.0043(9)	0.0126(15)	0.0050(8)	−0.0010(10)	0	0
O4A	0.0085(8)	0.0044(10)	0.0068(6)	0.0009(6)	−0.0002(5)	−0.0012(6)
O4B	0.0080(8)	0.0037(9)	0.0064(6)	−0.0014(6)	0.0016(5)	−0.0011(6)

Table 8.2: Structural parameters of YMn₂O₅ at RT in space group *Pb2₁m*.

atom	x	y	z	U_{iso} [Å^2]			
Y	0.13807(3)	0.17147(3)	0	0.00297(4)			
Mn1	0	1/2	0.25493(5)	0.00276(6)	GOF	=	1.28
Mn2	0.41135(5)	0.35047(4)	1/2	0.00304(6)	R	=	2.62 %
O1	0	0	0.2712(3)	0.0045(3)	R_w	=	5.41 %
O2	0.1633(2)	0.44439(19)	0	0.0044(3)			
O3	0.1513(2)	0.43115(19)	1/2	0.0044(3)			
O4	0.39466(18)	0.20628(13)	0.2433(2)	0.0047(2)			

atom	$U11$	$U22$	$U33$	$U12$	$U13$	$U23$
Y	0.00323(7)	0.00225(7)	0.00342(7)	−0.00028(6)	0	0
Mn1	0.00293(10)	0.00221(10)	0.00316(10)	0.00009(8)	0	0
Mn2	0.00347(10)	0.00222(10)	0.003415(10)	−0.00004(9)	0	0
O1	0.0057(5)	0.0036(5)	0.0041(5)	0.0013(5)	0	0
O2	0.0041(5)	0.0047(5)	0.0044(5)	0.0004(4)	0	0
O3	0.0033(5)	0.0055(5)	0.0045(5)	0.0004(4)	0	0
O4	0.0055(4)	0.0034(3)	0.0052(4)	0.0007(3)	−0.0004(3)	−0.0003(3)

Table 8.3: Structural parameters of YMn$_2$O$_5$ at $T = 28$ K in space group *Pbam*.

atom	x	y	z	U_{iso} [Å^2]			
YA	0.13892(13)	0.17141(5)	0	0.00317(15)			
YB	0.63726(12)	0.32845(5)	0	0.00273(15)			
Mn1	0.0002(2)	1/2	0.25494(5)	0.00278(5)			
Mn2A	0.4109(2)	0.35057(12)	1/2	0.0027(2)	GOF	=	1.22
Mn2B	0.9119(2)	0.14960(14)	1/2	0.0036(2)	R	=	2.75 %
O1	0.0010(8)	0.0032(6)	0.2711(3)	0.0045(3)	R_w^2	=	5.53 %
O2A	0.1647(7)	0.4473(7)	0	0.0044(11)			
O2B	−0.1620(8)	0.5587(7)	0	0.0048(11)			
O3A	0.1503(8)	0.4310(7)	1/2	0.0054(10)			
O3B	0.6523(8)	0.0693(7)	1/2	0.0037(9)			
O4A	0.3961(6)	0.2063(4)	0.2435(6)	0.0036(7)			
O4B	0.8930(6)	0.2933(5)	0.7570(7)	0.0060(8)			

atom	$U11$	$U22$	$U33$	$U12$	$U13$	$U23$
YA	0.0041(3)	0.0021(3)	0.0033(2)	−0.0003(3)	0	0
YB	0.0023(2)	0.0023(3)	0.0035(2)	0.0003(3)	0	0
Mn1	0.00292(9)	0.00224(9)	0.00319(9)	0.00009(8)	0.0003(3)	−0.0000(4)
Mn2A	0.0039(4)	0.0010(4)	0.0030(4)	0.0003(4)	0	0
Mn2B	0.0029(4)	0.0039(4)	0.0039(4)	0.0004(4)	0	0
O1	0.0055(5)	0.0037(5)	0.0044(5)	0.0011(4)	−0.0017(15)	−0.0033(15)
O2A	0.0019(17)	0.008(2)	0.0034(15)	0.0034(15)	0	0
O2B	0.006(2)	0.0025(19)	0.0054(17)	−0.0024(16)	0	0
O3A	0.0020(17)	0.009(2)	0.0054(15)	−0.0009(17)	0	0
O3B	0.0046(18)	0.0034(16)	0.0033(14)	−0.0016(16)	0	0
O4A	0.0058(13)	0.0020(12)	0.0029(10)	0.0033(10)	−0.0001(9)	0.0006(8)
O4B	0.0053(14)	0.0050(14)	0.0079(12)	0.0019(11)	0.0008(11)	−0.0012(11)

Table 8.4: Structural parameters of YMn$_2$O$_5$ at $T = 28$ K in space group *Pb2$_1$m*.

9 Conclusion

In the context of this thesis several multiferroic materials with antiferromagnetic and/or chiral magnetic structures have been studied thoroughly by different (polarised) neutron-scattering techniques in combination with X-ray diffraction. Special attention has been devoted to the switching of (chiral) antiferromagnetic domains.

Pyroxenes

Despite their similar composition $LiFeSi_2O_6$ and $NaFeSi_2O_6$ exhibit quite different properties. While $NaFeSi_2O_6$ is multiferroic and exhibits a spontaneous electric polarisation below $6\,K$, $LiFeSi_2O_6$ exhibits electric polarisation below $18\,K$ only in an applied magnetic field. Therefore, $LiFeSi_2O_6$ is not multiferroic in the sense of the definition, yet it is magnetoelectric.

In order to determine the magnetic structure, neutron-diffraction experiments have been performed on both compounds revealing different magnetic structures. $LiFeSi_2O_6$ undergoes a single magnetic phase transition below $18\,K$. The magnetic structure was examined by a single-crystal neutron-diffraction experiment. The chemical and the magnetic unit cell are identical and the magnetic space group is $P2_1/c'$. The magnetic structure represents a canted antiferromagnet with moments in the ac plane plus an additional b component. The main moment lies along the c direction.

Refinement of the magnetic structure of $NaFeSi_2O_6$ reveals a more complex magnetic structure. (Polarised) neutron measurements on single crystals and powders (natural and synthetic) allow the following picture: the magnetic structure of natural $NaFeSi_2O_6$ is incommensurate with propagation vector $\boldsymbol{k} = (0, 0.77, 0)$. Below $8\,K$ it sets in as a transverse spin-density wave with moments in the ac plane and below $6\,K$ it evolves into an incommensurate helix with moments remaining in the ac plane. The transition into the spiral phase is accompanied by the onset of ferroelectricity along the monoclinic axis b. In addition, the synthetic powder shows commensurate order with a propagation vector $\boldsymbol{k} = (0, 1, 0)$. By applying isotropic pressure to the natural sample the incommensurate order can be suppressed and commensurate order develops. Furthermore, it was observed that different samples of natural $NaFeSi_2O_6$ have a slightly different propagation vector varying from $\boldsymbol{k} = (0, 0.77, 0)$ to $\boldsymbol{k} = (0, 0.79, 0)$. This is most likely due to small differences in the composition of these natural samples. The strong influence of

the chemical composition and the mechanical pressure on the value of the propagation vector can be explained by the frustration of the magnetic structure of $NaFeSi_2O_6$.

A helical magnetic structure breaks inversion symmetry and can account for electric polarisation along the rotation axis of the helix. This is the case in $NaFeSi_2O_6$ as the rotation axis of the helix coincides with the direction of the spontaneous polarisation. It is noteworthy that the two magnetic transitions in $NaFeSi_2O_6$ require only a single irreducible representation. This is exceptional among the multiferroics.

Spherical polarisation analysis was used to demonstrate that antiferromagnetic domains in $LiFeSi_2O_6$ can be reversed by a combination of perpendicular as well as parallel electric and magnetic fields. The fields were applied in the paramagnetic phase and then the sample was cooled into the antiferromagnetic phase before the fields were removed. From symmetry considerations only a magnetic field or only an electric field should not give rise to a preferred antiferromagnetic domain. In $LiFeSi_2O_6$ a magnetic field induces an electric polarisation. Now, if the direction of this polarisation is defined by the direction of an applied electric field, the magnetic structure is influenced, too. The different directions of the applied electric and the magnetic field that can be used to influence the antiferromagnetic domains exploit different components of the magnetoelectric tensor. Reversion of one field (either magnetic or electric) causes inversion of the antiferromagnetic domain. Reversion of both fields restores the initial configuration.

Due to the fact that in the magnetic structure of $LiFeSi_2O_6$ the inversion symmetry is composed with time inversion ($\bar{1}'$), $LiFeSi_2O_6$ allows for ferrotoroidicity. Switching of antiferromagnetic domains is related to switching of ferrotoroidal domains. The crucial point about the toroidal state is whether it reveals some unique properties which distinguish it from an antiferromagnetic structure with broken inversion symmetry. As far as the experimental results in this thesis are concerned, no evidence for a unique feature of the toroidal domains can be confirmed.

The magnon dispersion of $LiFeSi_2O_6$ was determined by inelastic neutron scattering and sufficiently described by a Heisenberg model. The best-fit parameters result from a model with one ferromagnetic and two antiferromagnetic exchange interactions, while the gap near the zone-boundary has been described by an anisotropy term.

Time Dependence of Multiferroic Switching

Within the scope of this thesis the kinetics of electric-field induced switching of chiral magnetic structures was investigated by stroboscopic techniques for polarised neutron scattering. Two samples of $MnWO_4$ were examined. The experimental observations yield a surprisingly slow switching process within the time scale of about 2 ms to 30 ms.

The time scale of the switching process strongly depends on the temperature. In the vicinity of the high-temperature and the low-temperature phase transitions of the ferroelectric regime the sample can be switched faster than for intermediate temperatures. For the high-temperature phase transition (second order) this is in accordance with the fact that the coercive field decreases in the vicinity of the phase transition. In the vicinity of the low-temperature phase transition (first order) the coercive field does not decrease. This disagrees with the observation of a reduced relaxation time at this transition. In this context it must be pointed out that the coercive field and the time-dependent measurements were recorded on different samples.

A higher electric field causes a faster response. Measurements at two different samples confirm that the history of the sample plays a crucial role for the switching characteristics. The sample clearly develops a preferred state, which depends on the first field applied during cooling. The relaxation time into this preferred state is shorter than the relaxation time into the non-preferred state.

The process of fatigue of the sample is not completely understood, yet. To some extent the data are perfectly reproducible, however, not all changes are reversible.

It appears highly interesting to extend these observations to other chiral multiferroics. The static hysteresis loops on $TbMnO_3$ and $DyMnO_3$ presented in this thesis provide a good basis for these investigations. From the static hysteresis loops it becomes apparent that $TbMnO_3$ is a suitable candidate for this kind of investigation. $DyMnO_3$ on the contrary is less suitable.

Rare Earth Manganites

The investigations on $TbMnO_3$ and $DyMnO_3$ manly focus on the hysteresis loops (chiral ratio vs. electric field).

Even though $TbMnO_3$ was the first multiferroic material with chiral magnetic structure which was discovered, up to now only hysteresis loops for $MnWO_4$ and $Ni_3V_2O_8$ have been reported. The hysteresis loops were recorded by measuring the chiral ratio of the magnetic structure by polarised neutron scattering as a function of the electric field. The electric field was aligned parallel to the electric polarisation. The experiment demonstrates that the chirality of the magnetic spiral can be reversed by an applied electric field. By comparing temperature dependent data of the chiral ratio and the electric polarisation it was proven that the development of the chiral ratio resembles the development of the electric polarisation.

The use of two samples of different thickness confirms that the shape of the hysteresis scales with the strength of the electric field and that no other geometric effect has to be considered. The coercive field increases linearly with decreasing temperature. When cooling from the paramagnetic regime, only a small field is required for choosing a preferred chirality, and the value of the chiral ratio depends

linearly on the electric field strength for small fields.

In contrast to $TbMnO_3$ it has been much more difficult to drive hysteresis loops in $DyMnO_3$. Again, by comparing temperature dependent data of the chiral ratio and the electric polarisation, it was proven that the development of the chiral ratio resembles the development of the electric polarisation. The electric polarisation develops at the transition into the spiral magnetic phase and its magnitude drops to a lower value when the order of the Dy moments sets in. In fact just one hysteresis loop close to the ferroelectric transition could be recorded. One explanation might be that the Dy order is the reason for the poor response of the chiral ratio of the Mn moments to the electric field. In $DyMnO_3$ the order of the Dy moments has a large influence on the ferroelectric polarisation.

The quasi-lock-in of the magnetic propagation vector of $TbMnO_3$ was investigated with polarised neutrons. The results reveal that the lock-in takes place at temperatures slightly above the development of the chiral magnetic structure.

Furthermore, it has been shown that the propagation vector increases linearly with isotropic pressure. The highly frustrated and thus complex magnetic structure responds sensitively to any change in interatomic distances. The increase of the value of the incommensurability indicates that the antiferromagnetic exchange interaction is enhanced with respect to the ferromagnetic exchange interaction.

Precise X-ray single crystal measurements were performed at $TbMnO_3$ and YMn_2O_5. The refinement of the crystal structure yields good results. Nevertheless, the primary objective of analysing the origin of the ferroelectric polarisation has not been achieved. The measurements reveal that the deviations of the ions from their centrosymmetric positions in the ferroelectric phase is beyond the resolution limit of diffraction experiments. Otherwise, such measurements have not yet been reported in literature.

Bibliography

[1] H. Schmid, *Multi-ferroic magnetoelectrics*, Ferroelectrics **162**, 317 (1994).

[2] K. Aizu, *Possible Species of Ferromagnetic, Ferroelectric, and Ferroelastic Crystals*, Phys. Rev. B **2**, 754 (1970).

[3] W. Eerenstein, N. Mathur, and J. Scott, *Multiferroic and magnetoelectric materials*, Nature **442**, 759 (2006).

[4] J.-P. Rivera, *On definitions, units, measurements, tensor forms of the linear magnetoelectric effect and on a new dynamic method applied to Cr-Cl boracite*, Ferroelectrics **161**, 165 (1994).

[5] H. Schmid, *Some symmetry aspects of ferroics and single phase multiferroics*, J. Phys.: Cond. Matter **20**, 434201 (2008).

[6] M. v. Ardenne, G. Musiol, and U. Klemradt, *Effekte der Physik und ihre Anwendungen* (Verlag Harri Deutsch, 2005), 3rd ed.

[7] N. Spaldin and M. Fiebig, *The Renaissance of Magnetoelectric Multiferroics*, Science **309**, 391 (2005).

[8] P. Curie, *Sur la symétrie dans les phénomènes physiques, symétrie d'un champ électrique et d'un champ magnétique*, Journal de Physique **3**, 393 (1894).

[9] I. Dzyaloshinskii, *On the magneto-electric effect in antiferromagnets*, Sov. Phys. JETP **10**, 628 (1959).

[10] D. Astrov, *The magnetoelectric effect in antiferromagnetics*, Sov. Phys. JETP **11**, 708 (1960).

[11] G. Rado and V. Folen, *Observation of the Magnetically Induced Magnetoelectric Effect and Evidence for Antiferromagnetic Domains*, Phys. Rev. Lett. **7**, 310 (1961).

[12] D. Khomskii, *Multiferroics: Different ways to combine magnetism and ferroelectricity*, J. Magn. Magn. Mater. **306**, 1 (2006).

[13] N. Hill, *Why Are There so Few Magnetic Ferroelectrics?*, J. Phys. Chem. B **104**, 6694 (2000).

[14] T. Kimura, *Spiral Magnets as Magnetoelectrics*, Annu. Rev. Mater. Res. **37**, 387 (2007).

[15] M. Fiebig, *Kooperation trotz Frustration*, Physik Journal **1**, 14 (2009).

[16] D. Khomskii, *Classifying multiferroics: Mechanisms and effects*, Physics **2**, 20 (2009).

[17] S.-W. Cheong and M. Mostovoy, *Multiferroics: a magnetic twist for ferroelectricity*, Nat. Mater. **6**, 13 (2007).

[18] T. Kimura, T. Goto, H. Shintani, K. Ishizaka, T. Arima, and Y. Tokura, *Magnetic control of ferroelectric polarization*, Nature **426**, 55 (2003).

[19] M. Kenzelmann, A. Harris, S. Jonas, C. Broholm, J. Schefer, S. Kim, C. Zhang, S.-W. Cheong, O. Vajk, and J. Lynn, *Magnetic Inversion Symmetry Breaking and Ferroelectricity in $TbMnO_3$*, Phys. Rev. Lett. **95**, 087206 (2005).

[20] G. Lautenschläger, H. Weitzel, T. Vogt, R. Hock, A. Böhm, M. Bonnet, and H. Fuess, *Magnetic phase transitions of $MnWO_4$ studied by the use of neutron diffraction*, Phys. Rev. B **48**, 6087 (1993).

[21] G. Lawes, M. Kenzelmann, N. Rogado, K. Kim, G. Jorge, R. Cava, A. Aharony, O. Entin-Wohlman, A. Harris, T. Yildirim, et al., *Competing Magnetic Phases on a Kagomé Staircase*, Phys. Rev. Lett. **93**, 247201 (2004).

[22] A. B. Harris, *Landau analysis of the symmetry of the magnetic structure and magnetoelectric interaction in multiferroics*, Phys. Rev. B **76**, 054447 (2007).

[23] T. Arima, *Ferroelectricity Induced by Proper-Screw Type Magnetic Order*, J. Phys. Soc. Jpn. **76**, 073702 (2007).

[24] B. Mettout, P. Tolédano, and M. Fiebig, *Symmetry replication and toroidic effects in the multiferroic pyroxene $NaFeSi_2O_6$*, Phys. Rev. B **81**, 214417 (2010).

[25] H. Katsura, N. Nagaosa, and A. Balatsky, *Spin Current and Magnetoelectric Effect in Noncollinear Magnets*, Phys. Rev. Lett. **95**, 057205 (2005).

[26] I. Sergienko and E. Dagotto, *Role of the Dzyaloshinskii-Moriya interaction in multiferroic perovskites*, Phys. Rev. B **73**, 094434 (2006).

[27] T. Arima, A. Tokunaga, T. Goto, H. Kimura, Y. Noda, and Y. Tokura, *Collinear to Spiral Spin Transformation without Changing the Modulation Wavelength upon Ferroelectric Transition in $Tb_{1-x}Dy_xMnO_3$*, Phys. Rev. Lett. **96**, 097202 (2006).

[28] O. Prokhnenko, R. Feyerherm, E. Dudzik, S. Landsgesell, N. Aliouane, L. Chapon, and D. Argyriou, *Enhanced Ferroelectric Polarization by Induced Dy Spin Order in Multiferroic $DyMnO_3$*, Phys. Rev. Lett. **98**, 057206 (2007).

[29] K. Taniguchi, N. Abe, T. Takenobu, Y. Iwasa, and T. Arima, *Ferroelectric Polarization Flop in a Frustrated Magnet $MnWO_4$ Induced by a Magnetic Field*, Phys. Rev. Lett. **97**, 097203 (2006).

[30] O. Heyer, N. Hollmann, I. Klassen, S. Jodlauk, L. Bohatý, P. Becker, J. Mydosh, T. Lorenz, and D. Khomskii, *A new multiferroic material: $MnWO_4$*, J. Phys.: Cond. Matter **18**, L471 (2006).

[31] A. Arkenbout, T. Palstra, T. Siegrist, and T. Kimura, *Ferroelectricity in the cycloidal spiral magnetic phase of $MnWO_4$*, Phys. Rev. B **74**, 184431 (2006).

[32] G. Lawes, A. Harris, T. Kimura, N. Rogado, R. Cava, A. Aharony, O. Entin-Wohlman, T. Yildirim, M. Kenzelmann, C. Broholm, et al., *Magnetically Driven Ferroelectric Order in $Ni_3V_2O_8$*, Phys. Rev. Lett. **95**, 087205 (2005).

[33] R. Johnson, S. Nair, L. Chapon, A. Bombardi, C. Vecchini, D. Prabhakaran, A. Boothroyd, and P. Radaelli, *$Cu_3Nb_2O_8$: A Multiferroic with Chiral Coupling to the Crystal Structure*, Phys. Rev. Lett. **107**, 137205 (2011).

[34] H. Kimura, S. Kobayashi, Y. Fukuda, T. Osawa, Y. Kamada, Y. Noda, I. Kagomiya, and K. Kohn, *Spiral Spin Structure in the Commensurate Magnetic Phase of Multiferroic RMn_2O_5*, J. Phys. Soc. Jpn. **76**, 074706 (2007).

[35] L. Chapon, P. Radaelli, G. Blake, S. Park, and S.-W. Cheong, *Ferroelectricity Induced by Acentric Spin-Density Waves in YMn_2O_5*, Phys. Rev. Lett. **96**, 097601 (2006).

[36] C. Ederer and N. Spaldin, *Towards a microscopic theory of toroidal moments in bulk periodic crystals*, Phys. Rev. B **76**, 214404 (2007).

[37] N. Spaldin, M. Fiebig, and M. Mostovoy, *The toroidal moment in condensed-matter physics and its relation to the magnetoelectric effect*, J. Phys.: Cond. Matter **20**, 434203 (2008).

[38] B. Van Aken, J.-P. Rivera, H. Schmid, and M. Fiebig, *Observation of ferrotoroidic domains*, Nature **449**, 702 (2007).

[39] Y. Yamasaki, H. Sagayama, T. Goto, M. Matsuura, K. Hirota, T. Arima, and Y. Tokura, *Electric Control of Spin Helicity in a Magnetic Ferroelectric*, Phys. Rev. Lett. **98**, 147204 (2007).

[40] B. Aken, J. Rivera, H. Schmid, and M. Fiebig, *Anisotropy of Antiferromagnetic $180°$ Domains in $LiCoPO_4$ and $LiNiPO_4$*, Phys. Rev. Lett. **101**, 157202 (2008).

[41] E. Prince, ed., *International Tables for Crystallography Volume C: Mathematical, physical and chemical tables* (Kluwer Academic Publishers, 2004), 3rd ed.

[42] A.-J. Dianoux and G. Lander, eds., *Neuton Data Booklet* (OCP Science, 2003), 2nd ed.

[43] G. Bacon, *Neutron Diffraction* (Oxford at the Clarendon Press, 1962), 2nd ed.

[44] G. Squires, *Introduction to the Theory of Themal Neutron Scattering* (Dover Publications, INC., 1996).

[45] G. Shirane, S. Shapiro, and J. Tranquada, *Neutron Scattering with a Tiple-Axis Spectrometer* (Cambridge University Press, 2002).

[46] J. Rossat-Mignod, *Magnetic Structures* (Academic Press, 1987), vol. 23 C of *Methods of Experimental Physics*, chap. 19.

[47] J. Rodríguez-Carvajal, *FullProf Manual* (2001).

[48] M. Blume, *Polarization Effects in the Magnetic Elastic Scattering of Slow Neutrons*, Phys. Rev. **130**, 1670 (1963).

[49] S. Maleev, V. Bar'yakhtar, and R. Suris, *The scattering of slow neutrons by complex magnetic structures*, Sov. Phys. Solid State **4**, 2533 (1963).

[50] P. J. Brown, *Spherical Neutron Polarimetry* (Elsevier, 2006), chap. 5, Neutron Scattering from Magnetic Materials.

[51] R. Moon, T. Riste, and W. Koehler, *Polarization Analysis of Thermal-Neutron Scattering*, Phys. Rev. **181**, 920 (1969).

[52] P. Steffens, privat communication.

[53] W. Kelvin, *Baltimore Lectures on Molecular Dynamics and the Wave Theory of Light* (London: C. J. Clay and Sons, 1904), p. 619.

[54] L. Barron, *True and False Chirality and Absolute Asymmetric Synthesis*, J. Am. Chem. Soc. **108**, 5539 (1986).

[55] V. Simonet, M. Loire, and R. Ballou, *Magnetic chirality as probed by neutron scattering*, Eur. Phys. J. Special Topics **213**, 5 (2012).

[56] E. Rutherford, *Bakerian Lecture: Nuclear Constitution of Atoms*, Proc. R. Soc. A **97**, 374 (1920).

[57] E. Fermi, *Versuch einer Theorie der β-Strahlen. I*, Z. Phys. **88**, 161 (1934).

[58] J. Chadwick, *Possible Existence of a Neutron*, Nature **129**, 312 (1932).

[59] J. Chadwick, *The Existence of a Neutron*, Proc. R. Soc. A **136**, 692 (1932).

[60] W. Heisenberg, *Über den Bau der Atomkerne. I*, Z. Phys. **77**, 1 (1932).

[61] R. Bacher and E. Condon, *The Spin of the Neutron*, Phys. Rev. **41**, 683 (1932).

[62] R. Sutton, T. Hall, E. Anderson, H. Bridge, J. DeWire, L. Lavatelli, E. Long, T. Snyder, and R. Williams, *Scattering of Slow Neutrons by Ortho- and Parahydrogen*, Phys. Rev. **72**, 1147 (1947).

[63] I. Tamm and S. Altschuler, C. R. Acad. Sc. USSR **1**, 458 (1934).

[64] D. Mitchell and P. Powers, *Bragg Reflection of Slow Neutrons*, Phys. Rev. **50**, 486 (1936).

[65] F. Bloch, *On the Magnetic Scattering of Neutrons*, Phys. Rev. **50**, 259 (1936).

[66] J. Schwinger, *On the Magnetic Scattering of Neutrons*, Phys. Rev. **51**, 544 (1937).

[67] O. Frisch, H. von Halban, and J. Koch, *Some Experiments on the Magnetic Properties of Free Neutrons*, Phys. Rev. **53**, 719 (1938).

[68] P. Powers, *The Magnetic Scattering of Neutrons*, Phys. Rev. **54**, 827 (1938).

[69] O. Halpern and M. Johnson, *On the Theory of Neutron Scattering by Magnetic Substances*, Phys. Rev. **51**, 992 (1937).

[70] O. Halpern and M. Johnson, *Magnetic Scattering of Slow Neutrons*, Phys. Rev. **52**, 52 (1937).

[71] O. Halpern and M. Johnson, *On the Magnetic Scattering of Neutrons*, Phys. Rev. **55**, 898 (1939).

[72] L. Alvarez and F. Bloch, *A Quantitative Determination of the Neutron Moment in Absolute Nuclear Magnetons*, Phys. Rev. **57**, 111 (1940).

[73] C. Shull and J. Smart, *Detection of Antiferromagnetism by Neutron Diffraction*, Phys. Rev. **76**, 1256 (1949).

[74] D. Hughes and M. Burgy, *Reflection of Neutrons from Magnetized Mirrors*, Phys. Rev. **81**, 498 (1951).

[75] C. Shull, E. Wollan, and W. Koehler, *Neutron Scattering and Polarization by Ferromagnetic Materials*, Phys. Rev. **84**, 912 (1951).

[76] R. Nathans and A. Paoletti, *Magnetic Form Factor of Cobalt*, Phys. Rev. Lett. **2**, 254 (1959).

[77] R. Nathans, C. Shull, G. Shirane, and A. Andresen, *The use of polarized neutrons in determining the magnetic scattering by iron and nickel*, J. Phys. Chem. Solids **10**, 138 (1959).

[78] F. Tasset, *Zero field neutron polarimetry*, Physica B: Cond. Matter **156-157**, 627 (1989).

[79] R. Stewart, *Polarized Neutrons Intro and Techniques* (Delft, 2010), Lecture Notes: Polarised Neuton School.

[80] J. Schweizer, *Polarized Neutrons and Polarization Analysis* (Elsevier, 2006), chap. 4, Neutron Scattering from Magnetic Materials.

[81] B. Willis and C. Carlile, *Experimental Neutron Scattering* (Oxford University Press, 2009).

[82] H. Haken and H. Wolf, *Atom- und Quantenphysik* (Springer, 1993), 5th ed.

[83] National Institute of Standards and Technology, `http://physics.nist.gov/cuu/Constants/`.

[84] T. Jones and W. Williams, *Non-adiabatic spin flippers for thermal neutrons*, Nuclear Instruments and Methods **152**, 463 (1978).

[85] F. Mezei, *Neutron Spin Echo: A New Concept in Polarized Thermal Neutron Techniques*, Z. Phys. **225**, 146 (1972).

[86] L. P. Regnault, privat communication.

[87] E. Lelièvre-Berna, E. Bourgeat-Lami, P. Fouilloux, B. Geffray, Y. Gibert, K. Kakurai, N. Kernavanois, B. Longuet, F. Mantegezza, M. Nakamura, et al., *Advances in spherical neutron polarimetry with Cryopad*, Physica B: Cond. Matter **356**, 131 (2005).

[88] L. P. Regnault, B. Geffray, P. Fouilloux, B. Longuet, F. Mantegazza, F. Tasset, E. Lelièvre-Berna, S. Pujol, E. Bourgeat-Lami, N. Kernavanois, et al., *Spherical neutron polarization analysis on the three-axis spectrometer IN22*, Physica B: Cond. Matter **350**, E811 (2004).

[89] G. Eckold, *Time-resolved triple-axis spectroscopy – a new method for real-time neutron scattering*, Nucl. Instrum. Methods A **289**, 221 (1990).

[90] W. Heisenberg, *Zur Theorie des Ferromagnetismus*, Z. Phys. **49**, 619 (1928).

[91] T. Holstein and H. Primakoff, *Field Dependence of the Intrinsic Domain Magnetization of a Ferromagnet*, Phys. Rev. **58**, 1098 (1940).

[92] G. Czycholl, *Theoretische Festkörperphysik* (Vieweg, 2000).

[93] A. Sáenz, *Spin Waves in Exchange-Coupled Complex Magnetic Structures and Neutron Scattering*, Phys. Rev. **125**, 1940 (1962).

[94] S. Jodlauk, P. Becker, J. Mydosh, D. Khomskii, T. Lorenz, S. Streltsov, D. Hezel, and L. Bohatý, *Pyroxenes: a new class of multiferroics*, J. Phys.: Cond. Matter **19**, 432201 (2007).

[95] G. Redhammer, G. Roth, W. Paulus, G. André, W. Lottermoser, G. Amthauer, W. Treutmann, and B. Koppelhuber-Bitschnau, *The crystal and magnetic structure of Li-aegirine LiFe^{3+}Si$_2$O$_6$: a temperature-dependent study*, Phys. Chem. Minerals **28**, 337 (2001).

[96] G. Redhammer and G. Roth, *Structural variations in the aegirin solid-soltion series (Na,Li)FeSi$_2$O$_6$ at 298 K and 80 K*, Z. Kristallogr. **217**, 63 (2002).

[97] M. Baum, *Magnetische Struktur und Anregungen in Multiferroika*, Diplomarbeit, II. Physikalisches Institut, Universität zu Köln (2009).

[98] S. Jodlauk, *Neue Magnetoelektrika und magnetoelektrische Multiferroika*, Dissertation, Institut für Kristallographie, Universität zu Köln (2009).

[99] G. Redhammer, G. Roth, W. Treutmann, M. Hoelzel, W. Paulus, G. André, C. Pietzonka, and G. Amthauer, *The magnetic structure of clinopyroxene-type LiFeGe$_2$O$_6$ and revised data on multiferroic LiFeSi$_2$O$_6$*, J. Solid State Chem. **182**, 2374 (2009).

[100] M. Ackermann, privat communication.

[101] M. Meven, privat communication.

[102] J. Rodríguez-Carvajal, *FullProf*, http://www.ill.eu/sites/fullprof/.

[103] P. Brown, J. Forsyth, and F. Tasset, *A study of magnetoelectric domain formation in Cr$_2$O$_3$*, J. Phys.: Cond. Matter **10**, 663 (1998).

[104] P. Brown, J. Forsyth, and F. Tasset, *Studies of magneto-electric crystals using spherical neutron polarimetry*, Solid State Sciences **7**, 682 (2005).

[105] E. Ressouche, M. Loire, V. Simonet, R. Ballou, A. Stunault, and A. Wildes, *Magnetoelectric MnPS$_3$ as a candidate for ferrotoroidicity*, Phys. Rev. B **82**, 100408 (2010).

[106] M. Fisher, *The theory of equilibrium critical phenomena*, Rep. Prog. Phys. **30**, 615 (1967).

[107] J. Rodríguez-Carvajal and C. Frontera, *Refinement of flipping ratios using FULLPROF*.

[108] E. Baum, W. Treutmann, M. Behruzi, W. Lottermoser, and G. Amthauer, *Structural and magnetic properties of the clinopyroxenes NaFeSi$_2$O$_6$ and LiFeSi$_2$O$_6$*, Z. Kristallogr. **183**, 273 (1988).

[109] O. Ballet, J. Coey, G. Fillion, A. Ghose, A. Hewat, and J. Regnard, *Magnetic Order in Acmite; NaFeSi$_2$O$_6$*, Phys. Chem. Minerals **16**, 672 (1989).

[110] A. C. Komarek, *Complex ordering phenomena in transition metal oxides and oxy-halides*, Dissertation, II. Physikalisches Institut, Universität zu Köln (2009).

[111] G. Redhammer, A. Senyshyn, M. Meven, G. Roth, S. Prinz, A. Pachler, G. Tippelt, C. Pietzonka, W. Treutmann, M. Hoelzel, et al., *Nuclear and incommensurate magnetic structure of NaFeGe$_2$O$_6$ between 5 K and 298 K and new data on multiferroic NaFeSi$_2$O$_6$*, Phys. Chem. Minerals **38**, 139 (2011).

[112] R. Ballou and B. Ouladdiaf, *Representation Analysis of Magnetic Structures* (Elsevier, 2006), chap. 3, Neutron Scattering from Magnetic Materials.

[113] N. Qureshi, *Magnetic properties of the kagome staircase mixed system (Co$_x$Ni$_{1-x}$)$_3$V$_2$O$_8$*, Dissertation, Fachbereich Material- und Geowissenschaften, Technische Universität Darmstadt (2009).

[114] ILL homepage, http://www.ill.eu/instruments-support/instruments-groups/instruments/d10/characteristics/.

[115] A. Poole, P. Brown, and A. Wills, *Spherical neutron polarimetry (SNP) study of magneto-electric coupling in the multiferroic MnWO$_4$*, J. Phys.: Conf. Ser. **145**, 012074 (2009).

[116] T. Finger, D. Senff, K. Schmalzl, W. Schmidt, L. P. Regnault, P. Becker, L. Bohatỳ, and M. Braden, *Electric-field control of the chiral magnetism of multiferroic MnWO$_4$ as seen via polarized neutron diffraction*, Phys. Rev. B **81**, 054430 (2010).

[117] T. Finger, D. Senff, K. Schmalzl, W. Schmidt, L. P. Regnault, P. Becker, L. Bohatỳ, and M. Braden, *Polarized-neutron-scattering studies on the chiral magnetism in multiferroic MnWO$_4$*, J. Phys.: Conf. Ser. **221**, 012001 (2010).

[118] J. Leist, *Echtzeit-Untersuchungen der ferroelektrischen Phasenumwandlung in K$_2$SeO$_4$ und SrTiO$_3$*, Dissertation, Institut für Physikalische Chemie, Georg-August-Universität Göttingen (2009).

[119] M. Avrami, *Kinetics of Phase Change. I General Theory*, J. Chem. Phys. **7**, 1103 (1939).

[120] M. Avrami, *Kinetics of Phase Change. II Transformation-Time Relations for Random Distribution of Nuclei*, J. Chem. Phys. **8**, 212 (1940).

[121] M. Avrami, *Granulation, Phase Change, and Microstructure Kinetics of Phase Change. III*, J. Chem. Phys. **9**, 177 (1941).

[122] Y. Ishibashi and Y. Takagi, *Note on Ferroelectric Domain Switching*, J. Phsy. Soc. Jpn. **31**, 506 (1971).

[123] T. Hoffmann, P. Thielen, P. Becker, L. Bohatý, and M. Fiebig, *Time-resolved imaging of magnetoelectric switching in multiferroic MnWO$_4$*, Phys. Rev. B **84**, 184404 (2011).

[124] T. Kimura, G. Lawes, T. Goto, Y. Tokura, and A. Ramirez, *Magnetoelectric phase diagrams of orthorhombic RMnO₃ (R = Gd, Tb, and Dy)*, Phys. Rev. B **71**, 224425 (2005).

[125] J. Blasco, C. Ritter, J. García, J. de Teresa, J. Pérez-Cacho, and M. Ibarra, *Structural and magnetic study of Tb₁₋ₓCaₓMnO₃ perovskites*, Phys. Rev. B **62**, 5609 (2000).

[126] S. Quezel, F. Tcheou, J. Rossat-Mignod, G. Quezel, and E. Roudaut, *Magnetic structure of the perovskite-like compound TbMnO₃*, Physica B **86**, 916 (1977).

[127] R. Kajimoto, H. Yoshizawa, H. Shintani, T. Kimura, and Y. Tokura, *Magnetic structure of TbMnO₃ by neutron diffraction*, Phys. Rev. B **70**, 012401 (2004).

[128] M. Mostovoy, *Ferroelectricity in Spiral Magnets*, Phys. Rev. Lett. **96**, 067601 (2006).

[129] N. Aliouane, K. Schmalzl, D. Senff, A. Maljuk, K. Prokeš, M. Braden, and D. Argyriou, *Flop of Electric Polarization Driven by the Flop of the Mn Spin Cycloid in Multiferroic TbMnO₃*, Phys. Rev. Lett. **102**, 207205 (2009).

[130] I. Cabrera, M. Kenzelmann, G. Lawes, Y. Chen, W. Chen, R. Erwin, T. Gentile, J. Leão, J. Lynn, N. Rogado, et al., *Coupled Magnetic and Ferroelectric Domains in Multiferroic Ni₃V₂O₈*, Phys. Rev. Lett. **103**, 087201 (2009).

[131] A. Pimenov, A. Mukhin, V. Ivanov, V. Travkin, A. Balbashov, and A. Loidl, *Possible evidence for electromagnons in multiferroic manganites*, Nature Phys. **2**, 97 (2006).

[132] D. Senff, P. Link, K. Hradil, A. Hiess, L. P. Regnault, Y. Sidis, N. Aliouane, D. Argyriou, and M. Braden, *Magnetic Excitations in Multiferroic TbMnO₃: Evidence for a Hybridized Soft Mode*, Phys. Rev. Lett. **98**, 137206 (2007).

[133] D. Meier, N. Aliouane, D. N. Argyriou, J. A. Mydosh, and T. Lorenz, *New features in the phase diagram of TbMnO₃*, New J. Phys. **9**, 100 (2007).

[134] ILL homepage, `http://www.ill.eu/en/html/instruments-support/sample-environment/equipment/high-pressures/clamped-cells/04pcl150cb5/`.

[135] D. Senff, N. Aliouane, D. N. Argyriou, A. Hiess, L. P. Regnault, P. Link, K. Hradil, Y. Sidis, and M. Braden, *Magnetic excitations in a cycloidal magnet: the magnon spectrum of multiferroic TbMnO₃*, J. Phys.: Cond. Matter **20**, 434212 (2008).

[136] T. Hahn, ed., *International Tables for Crystallography Volume A: Space-group symmetry* (Kluwer Academic Publishers, 2002), 5th ed.

[137] V. Petricek, M. Dusekand, and L. Palatinus, *Jana2006*, `http://jana.fzu.cz/`.

[138] Y. Chen, H. Yuan, G. Li, G. Tian, and S. Feng, *Crystal growth and magnetic property of orthorhombic $RMnO_3$ (R = Sm-Ho) perovskites by mild hydrothermal synthesis*, J. Cryst. Growth **305**, 242 (2007).

[139] R. Feyerherm, E. Dudzik, N. Aliouane, and D. Argyriou, *Commensurate Dy magnetic ordering associated with incommensurate lattice distortion in multiferroic $DyMnO_3$*, Phys. Rev. B **73**, 180401 (2006).

[140] I. Kagomiya, S. Matsumoto, K. Kohn, Y. Fukuda, T. Shoubu, H. Kimura, Y. Noda, and N. Ikeda, *Lattice Distortion at Ferroelectric Transition of YMn_2O_5*, Ferroelectrics **286**, 167 (2003).

[141] C. Vecchini, L. Chapon, P. Brown, T. Chatterji, S. Park, S.-W. Cheong, and P. Radaelli, *Commensurate magnetic structures of RMn_2O_5 (R=Y,Ho,Bi) determined by single-crystal neutron diffraction*, Phys. Rev. B **77**, 134434 (2008).

[142] I. Kagomiya, K. ichi Kakimoto, and H. Ohsato, *Precursor phenomenon on ferroelectric transition in multiferroic YMn_2O_5*, J. Eur. Ceram. Soc. **30**, 255 (2010).

[143] I. Kagomiya, K. Kohn, and T. Uchiyama, *Structure and Ferroelectricity of RMn_2O_5*, Ferroelectrics **280**, 131 (2002).

Danksagung

Zunächst möchte ich mich bei Prof. Dr. Markus Braden für die unzähligen Ideen und Vorschläge zu Messungen bedanken, die mir eine vielseitige Grundlage für meine Dissertation verschafft haben. Außerdem danke ich ihm, dass er mir ermöglicht hat, an zwei Sommerschulen sowie der International Conference on Magnetism in Busan teilzunehmen.

Bei Prof. Dr. Ladislav Bohatý und bei Prof. Dr. Petra Becker möchte ich mich dafür bedanken, dass sie mir schon seit meiner Diplomarbeit für Fragen und Anregungen zur Verfügung standen. Die Gespräche mit ihnen waren stets höchst motivierend.

Bei Dr. Jeannis Leist und Prof. Dr. Götz Eckold möchte ich mich für die Kooperation bei den zeitaufgelösten Messungen bedanken. Besonderer Dank gilt hierbei Jeannis, der bei den Messungen einen unermüdlichen Einsatz gezeigt hat, und von dem ich eine Menge lernen konnte.

Bei Dr. Paul Steffens möchte ich mich neben der guten wissenschaftlichen vor allem für die persönliche Betreuung bedanken. Unsere Ausflüge ins Vercors und in die Chartreuse bleiben unvergessen.

Bei Dr. Karin Schmalzl bedanke ich mich für die gute Betreuung bei den schwierigen Messungen, die oftmals auch vom Local Contact überdurchschnittlichen Einsatz abverlangten.

Auch bei Dr. Yvan Sidis, Dr. Maria Theresa Fernández-Díaz, Dr. Astrid Schneidewind und Dr. Louis-Pierre Regnault bedanke ich mich für die gute Betreuung während meiner Messungen.

Bei Dr. Holger Ulbrich bedanke ich mich für die vortreffliche Zusammenarbeit im Röntgen-Kompetenz-Team.

Bei Simon Holbein, Jonas Stein und Christine Tölzer bedanke ich mich für unzählige Hilfestellung bei Messungen und Auswertungen.

Dr. Navid Qureshi, Thomas Finger, Dr. Ralf Müller und Dr. Alexander Komarek danke ich für die gute Zusammenarbeit in der Arbeitsgruppe.

Mit Dr. Joachim Hemberger und Matthias Ackermann konnte ich viele anregende Diskussionen über Multiferroika führen. Vielen Dank.

Bei Johanna Brand und Niels Gierse, die mich schon seit den ersten Tagen meines Studiums begleiten, bedanke ich mich insbesondere für das Zuhören in schwierigeren Zeiten.

Außerdem gilt mein Dank meinen Eltern Horst und Helga Baum, die mich während der letzten dreißig Jahre sehr unterstützt haben.

142

Erklärung

Ich versichere, dass ich die von mir vorgelegte Dissertation selbständig angefertigt, die benutzten Quellen und Hilfsmittel vollständig angegeben und die Stellen der Arbeit – einschließlich Tabellen, Karten und Abbildungen –, die anderen Werken im Wortlaut oder dem Sinn nach entnommen sind, in jedem Einzelfall als Entlehnung kenntlich gemacht habe; dass diese Dissertation noch keiner anderen Fakultät oder Universität zur Prüfung vorgelegen hat; dass sie – abgesehen von unten angegebenen Teilpublikationen – noch nicht veröffentlicht worden ist sowie, dass ich eine solche Veröffentlichung vor Abschluss des Promotionsverfahrens nicht vornehmen werde. Die Bestimmungen der Promotionsordnung sind mir bekannt. Die von mir vorgelegte Dissertation ist von Prof. Dr. M. Braden betreut worden.